Systematic Studies on Novel Polymeric Nanocomposites Embedded with a Well-Defined Fine Network

Yoshihiko Shimizu

2019

Contents

Chapter 1

General Introduction

1-1. Network embedded in matrices

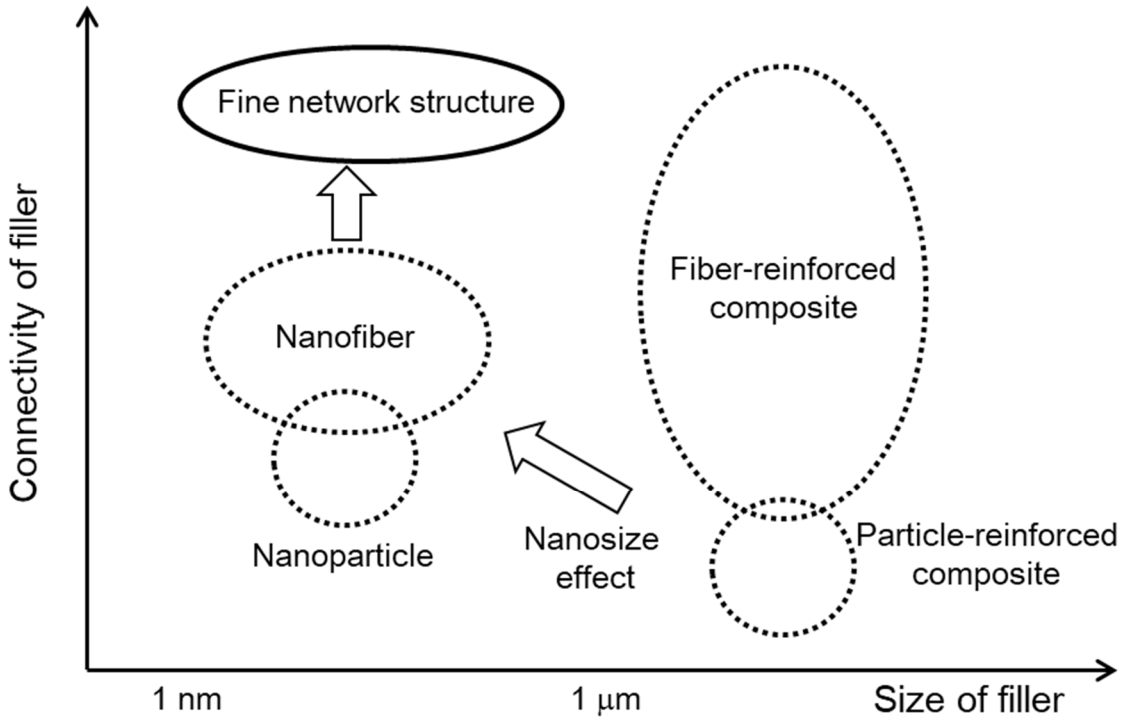

Figure 1-1. Schematic relationship between sizes and connectivity of fillers for polymeric composites.

Polymeric composite materials, in which fillers are embedded in matrices, are widely used as mechanical reinforcement materials in various industries. With fillers, the composites are classified as particle-reinforced composites and fiber-reinforced composites (Figure 1-1). Among them, long-fiber-reinforced composites with micrometer-scale-diameter fibers are widely used as high-reinforcement structural materials. This property is derived from the high connectivity of the

filler network, which is precisely controlled by the arrangement of fibers. For example, carbon fiber-reinforced plastic (CFRP), in which textiles or parallel layers of micrometer-scale-diameter carbon fibers are embedded in epoxy resin-based matrices, is widely utilized in aerospace applications as a reinforcement and lightweight structural material (Figure 1-2).

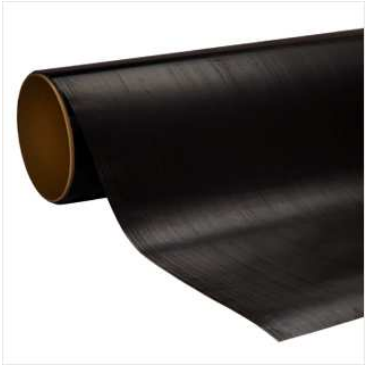

Figure 1-2. Image of a CFRP (TORAYCA®prepreg, TORAY, Japan) in which micrometer-scale-diameter carbon fibers are embedded in parallel in the matrix.[1]

Nanocomposites, in which nanometer- to submicron-scale fillers are embedded in matrices, are expected to be utilized as advanced materials with superior mechanical properties and functionality, such as electrical and optical properties including transparency derived from the "nanosize effect".[2, 3] Nanocomposites exhibit advantages of a small volume threshold for the formation of fine network structures and large surface area, which enable the effective achievement of functionality. However, it is difficult to control the arrangement of nanofillers in matrices due to amplified surface interactions.[4] Therefore, the fabrication, characterization, and functionalization of nanocomposites with a well-defined fine network structure are important to design new advanced materials.

1-2. Fine network structure in nature

Fine network structures are prevalent in biological multicomponent composites such as plants (cell

wall), the human body (bone, articular cartilage, ligament etc.), and other natural materials. The cell wall of plants has a thin and flexible layer structure with cellulose nanofiber networks, pectin, and structural proteins. The cell wall not only strengthens the plant body but also assists plant growth, in terms of cell differentiation, water transport, and defense.[5] Articular cartilage is mainly composed of collagen fiber networks intertwined with proteoglycan. The articular cartilage retains water in its network structure, providing wear resistance, enhanced mechanical, and low frictional properties.[6] Snakes possess some skin surfaces with a nanometer-scale honeycomb or net-like structure, providing high strength, wear resistance, and control of frictional properties at different regions of the body for slithering.[7] Thus, in nature, fine network structures provide not only reinforced mechanical properties but also functionalities such as mass transfer, retention, and friction by combining the advantages of multiple components.

The fine network structure in nature has been adopted in the form of biologically inspired artificial materials, i.e., biomimetic materials. For example, some tissue engineering applications, such as the artificial cartilage, have employed fiber-reinforced nanocomposites and a double network gel, which is composed of a stiff and brittle first polymer network and a soft second polymer network.[8] Polymeric foams with nanofibers, which are inspired cell wall structures, have also been applied as reinforced porous materials with superior thermal and energy-absorbing functionalities.[9, 10]

1-3. Mechanical properties

The mechanical properties of composites are categorized as static properties, such as the elastic modulus for small deformation, strength and toughness for large deformation; and dynamic properties such as viscoelasticity, impact resistance, and friction. Although many theoretical models have been proposed, it is difficult to estimate these mechanical properties systematically because they are affected in complex ways by fillers, matrices, and interfaces with each other depending on

the deformation. Moreover, as composites are generally heterogeneous in the microscopic scale, the relationship between the microscopic phenomenon and macroscopic mechanical properties is complex.

1-3-1. Rule of mixtures

The elastic modulus of a composite (E) can be theoretically and simply estimated as follows based on the rule of mixtures (Voigt model), considering the volume fraction (V_f) of a filler.

$$E = E_f V_f + E_m(1 - V_f) \qquad (1-1)$$

where subscripts f and m represent the filler and matrix, respectively. This model considers that the strain is uniform in the microscopic and macroscopic scales. Hence, in order to predict the elastic modulus by the rule of mixtures, some assumptions are made: i) Fillers penetrate in the direction parallel to the applied load (Figure 1-3). ii) The strain of the fillers accords with that of the matrices. iii) The interface between the fillers and matrices is perfect. These assumptions represent ideal mechanical properties.

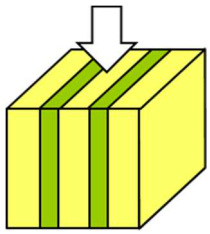

Figure 1-3. Illustration of a composite in which fillers (green) penetrate in the direction of loading.

In many cases, however, the actual elastic modulus is lower because the abovementioned assumptions are not satisfied. Therefore, several improved models have been proposed, which mainly focus on the geometry and topology of fillers, such as the size, shape, uniformity, anisotropy, and connectivity.[11-13]

1-3-2. Percolated filler model

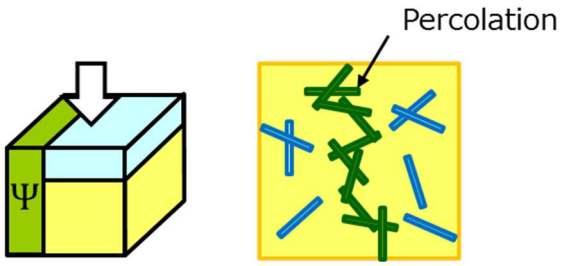

Figure 1-4. Illustration of a composite embedded with percolated fillers (green).

Mechanical models focusing on the connectivity of fillers have also been reported. The percolation model[14, 15] describes the mechanical properties of a composite embedded with the percolating filler network parallel to the loading direction and non-percolating filler phase vertical to the loading direction in the matrix (Figure 1-4). According to the percolation model, the elastic modulus of a composite E is expressed by

$$E = \frac{(1 - 2\Psi + \Psi X_f)E_m E_f + (1 - X_f)\Psi E_f^2}{(1 - X_f)E_f + (X_f - \Psi)E_m} \qquad (1-2)$$

where E_m and E_f are the elastic modulus of the matrix phase and filler phase, respectively, and X_f is the volume fraction of the filler phase. Ψ is the percolation volume fraction of the fillers. It should be noted that this model suggests that the elastic modulus of the composite primarily increases with increasing percolated volume fraction. In a nanocomposite system, in which cellulose whiskers are three-dimensionally and randomly dispersed, Ψ is given by

$$\Psi = X_r \left(\frac{X_r - X_c}{1 - X_c}\right)^{0.4} \qquad (1-3)$$

where X_c is the critical volume fraction of the fillers for percolation, which is given by $X_c = 0.7/A$ for $X_c \leq X_r$. A is the aspect ratio of the fillers.[16] It should be noted that this model suggests that the aspect ratio is the most important factor for the formation of a network structure, i.e., nanoscale fillers with a high aspect ratio are superior for effective enhancement of the mechanical properties of

composites despite the small filler fraction.

1-3-3. Lattice model

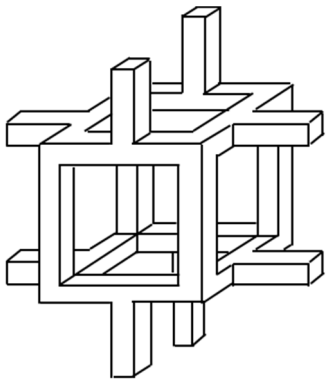

Figure 1-5. Illustration of a lattice structure.

Mechanical models of a network structure have also been reported. Figure 1-5 shows an illustration of a lattice structure.[17] In general, a lattice structure consists of joints, struts, and spaces. The struts are branched three-dimensionally at the joint and connected to other joints. The lattice network structure is characterized as the length, thickness, and shape of the strut, connectivity of the joint, and shape and size of the space. The most important characteristic of the lattice structure is that the fillers (struts) are perfectly connected (percolated) and self-supported.

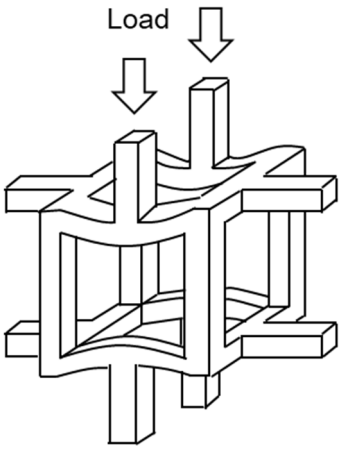

Figure 1-6. Schematic of bending deformation of a lattice structure.

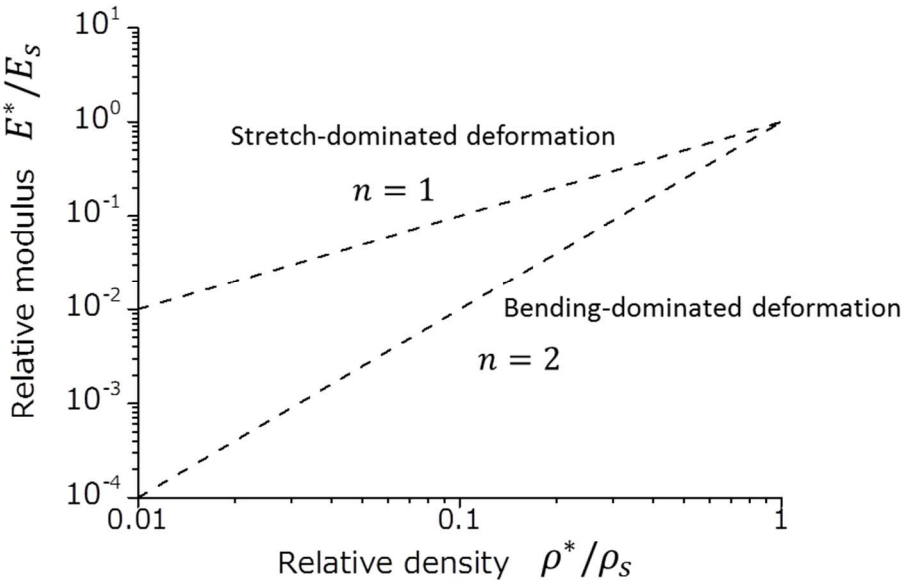

Figure 1-7. Plots of relative modulus E^*/E_s against relative densityρ^*/ρ_s of the lattice structure.

Figure 1-6 shows the representative deformation behavior of a lattice network structure, which can be categorized as the stretching (compressing) and bending of struts. The relative modulus of a lattice with similar geometry or topology is scaled as $E^*/E_s \sim (\rho^*/\rho_s)^n$, where E^* and E_s are the modulus of the network and bulk, respectively; and ρ^* and ρ_s are the density of the lattice and bulk, respectively (Figure 1-7).[18] A scaling exponent n close to 1 indicates stretch-dominated deformation behavior of the struts, whereas an exponent n close to 2 indicates bending-dominated deformation. An exponent n greater than 2 indicates that some parts in the lattice network are inefficient for load transfer due to the inhomogeneity of the lattice network derived from defects such as the relaxation, looping, or dangling of struts. Thus, the uniformity of the network structure affects the enhancement of mechanical properties such as the modulus and strength, due to stress distribution.

Subsequently, for composites embedded with the lattice network in matrices, deformation of the lattice network involves deformation of the matrix. Therefore, the bend-deformation of the network is expected to be suppressed depending on the lateral reinforcement of the matrix. Otherwise, a

segment of the matrix will have to undergo a forced large and heterogeneous deformation.[19] In other words, the deformation behavior of the network is associated with the mechanical properties of the matrices.

1-4. Matrices and functionalities

A fine network structure with continuous pores allows the adsorption, holding, transfer, and separation of fluid mass derived from the large surface area and connectivity of the network. Accordingly, a fine network structure is employed as a porous material with properties such as low weight, mass storage, separation, energy insulation, and transfer. A fine network structure containing a liquid as the pore matrix is expected to effectively improve the mechanical properties by offering resistance to fluid flow in the pores and the frictional property by the formation of fluid films on sliding surfaces. Therefore, such materials are promising as tribomaterials with superior wear resistance and lubrication. For example, a gel, in which a large amount of liquid is immersed in a three-dimensionally cross-linked fine network, exhibits specific frictional behavior derived from not only the interfacial interaction between the gel and an opposite substrate but also the flow of the fluid in and out of the gel. Gong et al. proposed a repulsion-adsorption model considering the interfacial interaction between polymer chains of a gel and substrate.[20] In this model, the friction of a gel is determined by two factors: elastic deformation of the polymer chain derived from the adsorption, and lubrication of the hydrated layer of the polymer network. Therefore, the mechanical properties of a gel containing a network and fluid play an important role in the tribological behavior. Various kinds of matrices with viscoelasticity can also be applied to the network structure, to provide composites such as pseudo solids, elastomers, and resins. The functionalities of the thus-obtained composites are closely related to the fine network structure and matrices. For example, properties such as impact resistance, shape memory, and stimuli response, whereby deformation occurs in

response to a stimulus such as stress and temperature, employ the difference in mechanical properties between the network and matrices. Accordingly, for the extensible design of composites, it is important to understand the functionalities of composites associated with the network and matrices over a wide range of strains or viscoelasticities.

1-5. Strategies for preparing a fine network structure and composites

Various methods for preparing fine network structures have been developed. Self-assembly or phase separation of immiscible components such as polymer blends, block copolymers, and polymer solutions is a simple and typical technique for preparing a periodic bi-continuous structure with a submicron to micrometer-sized network.[21] Drying of gels is another technique to obtain a fine network structure. The gel is prepared by the sol-gel process,[22] regeneration from solution,[23] and dispersion of nanofibers and nanoparticles[24]. Recently, lithography and 3D printing have been employed to fabricate well-defined fine network structures.[25–29] Particularly, the nanoframe network structure is fabricated by the light-induced crosslinking of photoresists using interference lithography.

1-6. Cellulose nanofiber (CNF)

Cellulose nanofiber (CNF), which has a typical diameter of several to 50 nm and a length of several micrometers, is obtained either by the mechanical or chemical treatment of biomass, such as woods and plants. The mechanical disintegration of wood pulp involves grinding,[30] repeated high-pressure homogenization,[31, 32] and aqueous counter collisions,[33] whereas chemical disintegration employs 2,2,6,6-tetramethylpiperidine-1-oxyl radical (TEMPO)-mediated oxidation/disintegration.[34] The most important and remarkable characteristics of CNF are the high Young's modulus (140 GPa[35, 36]) and strength (2–6 GPa[37]) derived from the crystal modulus of cellulose-I along the longitudinal

direction. Furthermore, CNF has a high aspect ratio, and is potentially superior as a reinforcement filler for polyolefin, polystyrene, and poly(meth)acrylate matrices. However, as the surface of CNF is hydrophilic, perfect dispersion in a matrix is quite difficult unless the surface nature is changed to be hydrophobic either by the chemical modification of hydrophobic groups[38] or physical adsorption of surfactants or polymers[39–41] in order to suppress the numerous inter- or intramolecular hydrogen bonds among CNFs. Another important approach to preparing high-performance CNF-reinforced composites utilizes a preformed (templated) "network" of unmodified CNF.[42, 43] This approach is expected to introduce a highly percolated CNF network into the composites and achieve effective reinforcement with only a small amount of CNF. The effect of reinforcement by the CNF network can be evaluated by independently controlling the dispersity and interfacial interaction. However, in the fabrication of a CNF network by sol-gel processes, including solvent exchange to a poor solvent, the issue of aggregation is a significant drawback.

1-6-1. Bacterial cellulose (BC) gel

Bacterial cellulose (BC) gel, which is produced by the bacterium *Acetobacter xylinus*, is composed of a ribbon-shaped CNF network with cross-sections of approximately 4×80 nm and lengths of several micrometers[44] (Figure 1-8). BC has desirable mechanical properties[45–47] such as a high Young's modulus (114 GPa[48]) derived from the high crystallinity of cellulose-I (more than 70%[49]), similar to other cellulosic resources. Therefore, it has been utilized as a reinforcement filler for polymer composite materials.[50–54] Notably, the highly fine and pure CNF network structure of a BC gel is maintained in water despite it containing less than 1% of BC because of the high aspect ratio and entanglement. Therefore, BC gel is expected to be utilized as a precursor material to prepare ideal aerogels,[55–59] as well as gels and composite materials for tissue engineering and other applications.[60, 61] Moreover, as BC can disperse without modification or the adsorption of additives,

we can directly evaluate the contribution of the CNF reinforcement.

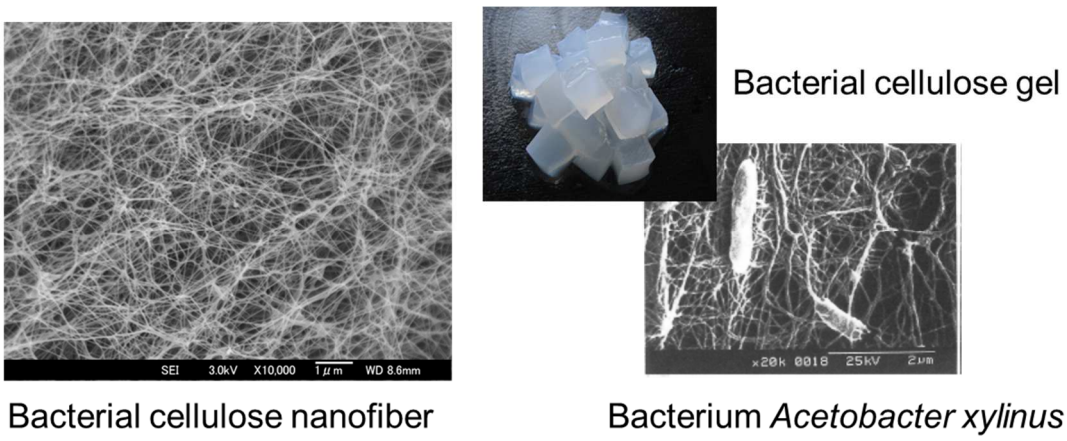

Figure 1-8. Images of bacterial cellulose gels, bacterium *Acetobacter xylinus*, and bacterial cellulose nanofiber in the gel.

1-7. Polymer monolith

Polymer monoliths, which consist of bi-continuous three-dimensional well-defined fine networks of framework and pores, possess unique functionalities such as low density, energy adsorption and mass separation, and holding and transfer, derived from the high porosity and surface area. Therefore, they are promising for advanced applications such as separators and filters for high-performance liquid chromatography (HPLC) [62–69], lithium-ion batteries,[70] catalyst supports, and reaction fields[71]. Polymer monoliths are prepared by the phase separation of a polymer solution[72] or *in situ* polymerization-induced phase separation between polymers and non-reactive porogen. The microscopic morphology of polymer monoliths, such as the pore size and hence porosity, is the most important factor determining their properties, which are mainly controlled by the reaction rate, including reaction temperature, affinity, and ratio of the two phases.

Among polymer monoliths, the epoxy resin-based polymer monolith, which is formed by the

reaction of epoxy and amine monomers in non-reactive porogen, is attractive. This is because the sizes of the framework and pores can be controlled easily by changing conditions including the polymerization temperature, type of porogen, and ratio of epoxy and amine groups[73–79] (Figure 1-9). The most important characteristic of epoxy resin-based polymer monoliths is the high strength derived from the rigid and well-defined fine epoxy resin-based-network. Hence, they can also be applied as a mechanical reinforcement for composites, energy absorption,[80–83] and tribological applications. Some approaches have been reported to prepare various shapes of epoxy-based polymer monoliths. Molding is typically performed to prepare various types of shapes such as blocks, rods, and membranes.[84, 85] Suspension polymerization can also be used to prepare particles.[86–88]

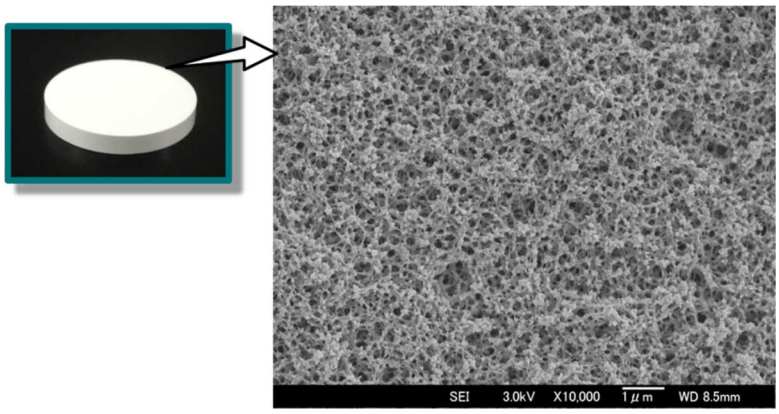

Figure 1-9. FE-SEM image of epoxy resin-based monolith.

1-8. Background and purpose of this thesis

There are considerable experimental, simulation, and theoretical studies on the mechanical properties of nanocomposites containing a fine network structure. The definition of a network structure is important, because mechanical properties largely depend on the morphology of the network structure. However, there are few experimental studies on the mechanical and structural characterization of nanocomposites with a well-defined fine network structure, which systematically

focus on matrices of varying viscoelasticity. Furthermore, there are few frictional studies on a well-defined fine network structure that associate with the mechanical properties, despite their close relationship. In order to elucidate these aspects, some challenges need to be overcome:

i) Preparation of a well-defined fine network structure-introduced composite independent of the properties of matrices, which is impeded by the different interfacial properties.

ii) Preparation of a well-defined fine network structure-introduced composite with a wide range of configuration, which is impeded by the few versatile processes available for preparation.

For the first challenge, self-assembly processes such as phase separation and drying are typically employed to prepared composites. However, their use is restricted in the matrix because of the deformation or aggregation of the network due to interfacial interaction. For the second challenge, in previous work, we reported a preparation method for skinless membranes[70] and particles[75] of epoxy resin-based polymer monoliths for application in mass separators. To apply this method for tribomaterials, it is necessary to establish a versatile process for preparing a film on a sliding substrate. Consequently, our aims are as follows:

i) To establish an expandable system for the preparation of well-defined fine network structures and composite with them.

ii) To propose a strengthening mechanism of composites reinforced with well-defined fine network structures, and enable systematic understanding common to composites with various matrices.

iii) To propose a frictional mechanism for composites with well-defined fine network structures by associating with the mechanical properties.

iv) To demonstrate application toward tribomaterials by utilizing our fabrication system and understanding.

1-9. Outline of this thesis

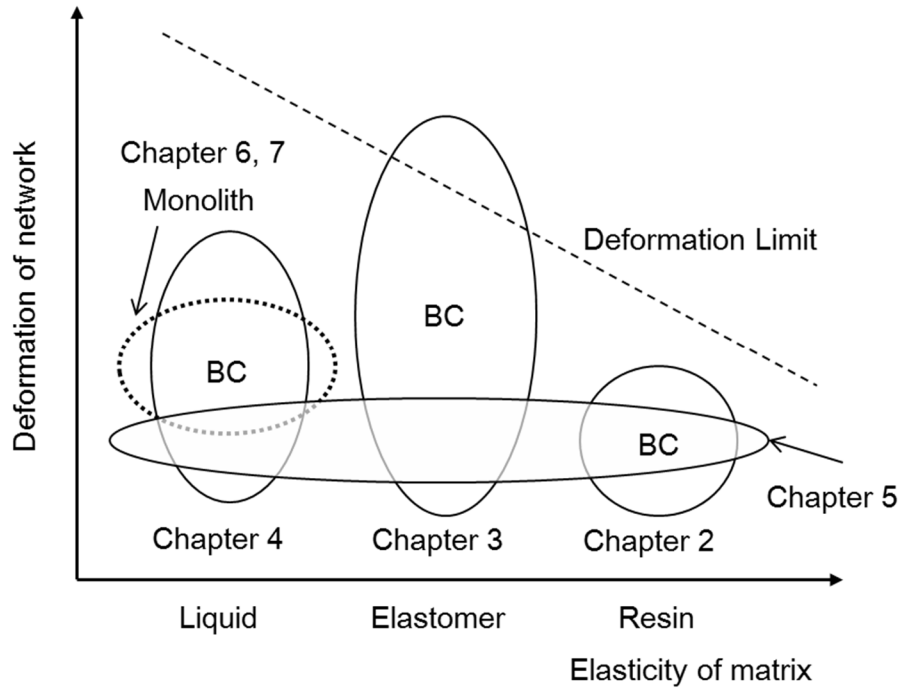

Figure 1-10. Schematic of this thesis.

Figure 1-10 shows a schematic of this thesis, which is focused on the mechanical properties of the matrix and network. In Part 1 (Chapters 2, 3, 4, and 5), BC gels were utilized as a well-defined fine network structure. We prepared BC-reinforced nanocomposites with various viscoelastic matrices such as resin, elastomer, and liquid, and mainly discussed the mechanical properties. In Part 2 (Chapters 6 and 7), an epoxy resin-based monolith was utilized as a well-defined fine network structure. We prepared a thin monolith on a substrate and mainly discussed the mechanical and frictional properties.

In Part 1, we first established an expandable system for the preparation of well-defined fine network structure-induced nanocomposites using BC gels. Subsequently, the mechanical and frictional properties of the nanocomposites were discussed by associating with a wide range of viscoelasticities and deformations of matrices.

In Chapter 2, we focused on the microscopic small compressive deformation of a rigid composite reinforced with a BC nanofiber network. Poly(methyl methacrylate) (PMMA) resin composites were prepared by stepwise solvent exchange, followed by free radical polymerization; the process is collectively termed "*in situ* solvent exchange and polymerization" (Figure 1-11). Nano-indentation experiments were performed to discuss the microscopic compressive deformation of the resin composite. We demonstrated effective reinforcement derived from the stretch-dominated deformation of a BC network by the lateral reinforcement of the matrix.

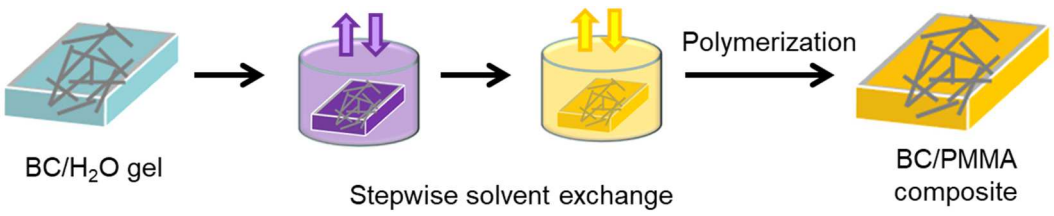

Figure 1-11. Schematic showing the preparation of a BC/PMMA composite by *in situ* solvent exchange and polymerization.

In Chapter 3, we focused on various microscopic and macroscopic stretched deformations of soft composites. A poly(ethyl acrylate) (PEA) elastomeric nanocomposite with a well-defined BC nanofiber network was prepared by *in situ* solvent exchange and polymerization (Chapter 2). Tensile tests were performed to analyze the various deformations of the BC nanofiber network in the soft matrix. A large deformation was characterized by exceptionally high fracture strain, good stretchability, and effective strain hardening with necking. Necking occurred due to the network structure of the fully aligned BC nanofibers by sliding entanglement points in response to deformation.

In Chapter 4, we focused on the dynamic deformation of gels. Bottle-brush-type hybrid gels reinforced with a BC nanofiber network were prepared by *in situ* solvent exchange and

polymerization (Figure 1-12). The gels were expected to exhibit superior mechanical and frictional properties derived from the BC nanofiber network and suppression of interfacial interaction by the bottle-brush network, based on the osmotic pressure of the concentrated polymer brush (CPB). The hybrid gels were prepared by the atom transfer radical polymerization (ATRP) of poly(ethylene glycol) methyl ether methacrylate (PEGMA) on the surface of BC and a macro-initiator network. The mechanical and frictional properties were evaluated using a rotatory tribometer and rheometer. The hybrid gel was remarkably reinforced by the BC nanofiber network depending on the BC content. The friction coefficient of the hybrid gel was of the order of 10^{-4} in magnitude, suggesting that adhesion was effectively suppressed. By dynamic viscoelasticity measurements, the friction coefficient in the shoulder regime of the Stribeck curve was derived from the elastic modulus and adhesion force of the gels.

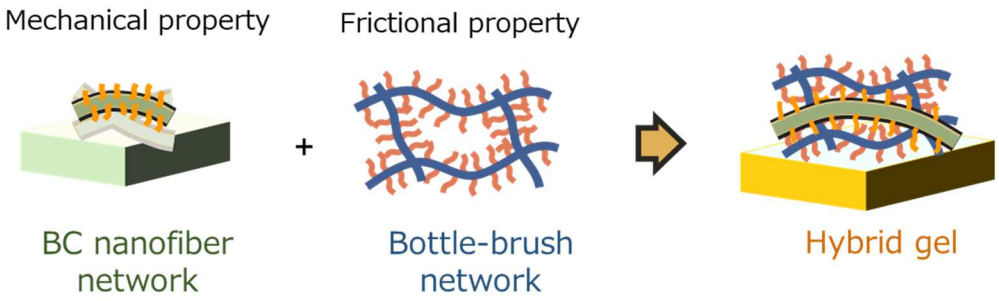

Figure 1-12. Schematic of a bottle-brush-type hybrid gel reinforced with a BC nanofiber network.

In Chapter 5, we systematically discussed the mechanical properties of the BC nanofiber network embedded in various viscoelastic matrices. The composites were reinforced by suppressing the deformation of the BC nanofiber network depending on the elasticity of the surrounding elastic matrices.

In Part 2, we first established an expandable system for the preparation of epoxy resin-based monolith films on substrates by dip coating. Subsequently, the tribological properties were discussed

by associating with the properties of the monoliths and fluid matrices.

In Chapter 6, we demonstrated the preparation of epoxy resin-based monolith films on substrates by dip coating (Figure 1-13). It is crucial to control the viscosity of the polymerization mixture during the fabrication of thin monoliths. Then, tribological properties were discussed by considering the mechanical properties of the monoliths. Suppression of deformation was achieved. The friction coefficient of the monoliths was a function of the pore size, thickness of the monoliths, and viscosity of the fluid, suggesting that the frictional properties of the monolith depended on fluid flow in the pores.

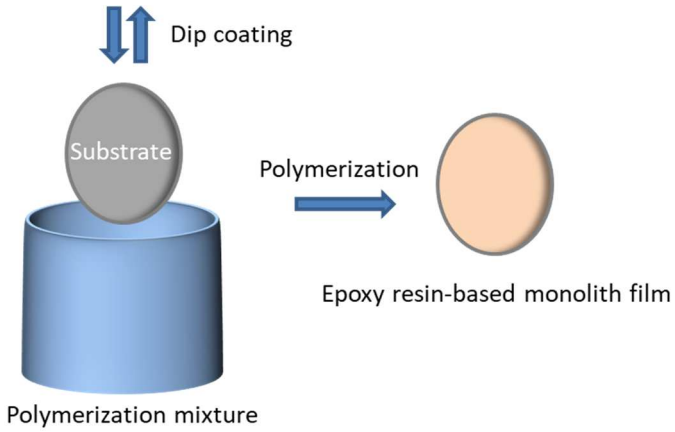

Figure 1-13. Schematic showing the preparation of an epoxy resin-based monolith film on a substrate by dip coating.

In Chapter 7, we discussed the tribological properties of the monoliths by considering the behavior of the sliding surface, including surface roughness, fluid flow, exuding, and fluid film thickness by optical interferometry. Further, we discussed in poor lubrication utilized the advantage of exuding property of monoliths. The fluid film thickness increased with the increase in sliding velocity, in accordance with the elasto-dynamic lubrication (EHL) theory. Monoliths exhibited a lesser influence of roughness due to their softness, and superior frictional properties under poor lubrication, derived

from the exuding property. In conclusion, monoliths have the potential to maintain a soft EHL despite poor lubrication, by controlling the exuding and flowing of the lubricant.

In Chapter 8, the monolith film was applied toward sliding machine elements. A monolith-coated sliding bearing a monolith film embedded in micrometer-scale-depth of aluminum alloy grooves, was prepared and tribological properties including running-in process and wear resistance was evaluated by using the apparatus which was closely correlated to actual use.

1-10. References

1. TORAY homepage (http://www.torayca.com/lineup/index.html)
2. S. Y. Fu, X. Q. Feng, B. Lauke, Y. W. Mai. *Composites, Part B* **2008**, *39*, 933–961.
3. L. Sun, R. F. Gibson, F. Gordaninejad, J. Suhr. *Compos. Sci. Technol.* **2009**, *69*, 2392–2409.
4. J. Cho, M. S. Joshi, C. T. Sun. *Compos. Sci. Technol.* **2006**, *66*, 1941–1952.
5. D. J. Cosgrove. *Nat. Rev. Mol. Cell Biol.* **2005**, *6*, 850.
6. F. A. Sophia, A. Bedi, S. A. Rodeo. *Sports health* **2009**, *1*, 461–468.
7. R. A. Berthé, G. Westhoff, H. Bleckmann, S. N. Gorb. *J. Comp. Physiol.* **2009**, *195*, 311–318.
8. C. Azuma, K. Yasuda, Y. Tanabe, H. Taniguro, F. Kanaya, A. Nakayama, Y. M. Chen, J. P. Gong, Y. Osada. *J. Biomed. Mater. Res., Part A* **2006**, *81*, 373380.
9. A. J. Svagan, M. A. A. Samir, L. A. Berglund. *Adv. Mater.* **2008**, *20*, 1263–1269.
10. L. J. Lee, C. Zeng, X, Cao, X. Han, J. Shen, G. Xu. *Compos. Sci. Technol*. **2005**, *65*, 2344–2363.
11. J. H. Affdl, J. L. Kardos. *Polym. Eng. Sci.* **1976**, *16*, 344–352.
12. H. L. Cox. *Br. J. Appl. Phys.* **1952,** *3*, 72.
13. S. Ahmed, F. R. Jones. *J. Mater. Sci.* **1990**, *25*, 4933–4942.
14. N. Ouali, J. Cavaillé, J. Perez. *Plast., Rubber Compos. Process. Appl.* **1991**, *16*, 55–60.
15. M. Takayanagi, S. Uemura, S. Minami. *J. Polym. Sci., Part C: Polym. Symp.* **1964**, 113–122.

16. V. Favier, J. Y. Cavaille, G. R. Canova, S. C. Shrivastava. *Polym. Eng. Sci.* **1997**, *37*, 1732–1739.

17. M. F. Ashby. *Philos. Trans. R. Soc., A* **2006**, *364*, 15–30.

18. L. J. Gibson, M. F. Ashby. *Cellular solids: structure and properties. Cambridge university press.* **1999**.

19. C. P. Brangwynne, F. C. MacKintosh, S. Kumar, N. A. Geisse, J. Talbot, L. Mahadevan, K. K. Parker, D. E. Ingber, D. A. Weitz. *J. Cell Biol.* **2006**, *173*, 733–741.

20. J. P. Gong. *Soft matter* **2006**, *2*, 544–552.

21. E. L. Thomas, D. M. Anderson, C. S. Henkee, D. Hoffman. *Nature* **1988**, *334*, 598–601.

22. A. S. Dorcheh, M. H. Abbasi. *J. Mater. Process. Technol*. **2008**, *199*, 10–26.

23. H. Jin, Y. Nishiyama, M. Wada, S. Kuga. *Colloids Suf. A* **2004**, *240*, 63–67.

24. Y. Kobayashi, T. Saito, A. Isogai. *Angew. Chem., Int. Ed.* **2014**, *53*, 10394–10397.

25. M. Campbell, D. N. Sharp, M. T. Harrison, R. G. Denning, A. J. Turberfield. *Nature* **2000**, *404*, 53.

26. T. A. Schaedler, A. J. Jacobsen, A. Torrents, A. E. Sorensen, J. Lian, J. R. Greer, L. Valdevit, W. B. Carter. *Science* **2011**, *334*, 962–965.

27. L. Wang, J. Lau, E. L. Thomas, M. C. Boyce. *Adv. Mater.* **2011**, *23*, 1524–1529.

28. J. H. Lee, J. P. Singer, E. L. Thomas. *Adv. Mater.* **2012**, *24*, 4782–4810.

29. N. A. Fleck, V. S. Deshpande, M. F. Ashby. *Proc. R. Soc. London, Ser. A* **2010**, *466*, 2495–2516.

30. K. Abe, S. Iwamoto, H. Yano. *Biomacromolecules* **2007**, *8*, 3276–3278.

31. A. F. Turbak, F. W. Snyder, K. R. Sandberg. *J. Appl. Polym. Sci.: Appl. Polym. Symp.* **1983**, *37*, 815–827.

32. H. Yano, S. Nakahara. *J. Mater. Sci.* **2004**, *39*, 1635–1638.

33. T. Kondo, R. Kose, H. Naito, W. Kasai. *Carbohydr. Polym.* **2014**, *112*, 284–290.

34. T. Saito, Y. Nishiyama, J. -L. Putaux, M. Vignon, A. Isogai. *Biomacromolecules* **2006**, *7*, 1687–1691.

35. I. Sakurada, Y. Nukushina, T. Ito. *J. Polym. Sci.* **1962**, *57*, 651–660.

36. T. Nishino, K. Takano, K. Nakamae. *J. Polym. Sci., Part B: Polym. Phys.* **1995**, *33*, 1647–1651.

37. T. Saito, R. Kuramae, J. Wohlert, L. A. Berglund, A. Isogai. *Biomacromolecules* **2012**, *14*, 248–253.

38. A. Sato, D. Kabusaki, H. Okumura, T. Nakatani, F. Nakatsubo, H. Yano. *Composites, Part A* **2016**, *83*, 72–79.

39. K. Sakakibara, H. Yano, Y. Tsujii. *ACS Appl. Mater. Interfaces* **2016**, *8*, 24893–24900.

40. L. Petersson, I. Kvien, K. Oksman. *Compos. Sci. Technol.* **2007**, *67*, 2535–2544.

41. J. Kim, G. Montero, Y. Habibi, J. P. Hinestroza, J. Genzer, D. S. Argyropoulos, O. J. Rojas. *Polym. Eng. Sci.* **2009**, *49*, 2054–2061.

42. J. R. Capadona, K. Shanmuganathan, S. Trittschuh, S. Seidel, S. J. Rowan, C. Weder. *Biomacromolecules* **2009**, *10*, 712–716.

43. J. R. Capadona, O. Van Den Berg, L. A. Capadona, M. Schroeter, S. J. Rowan, D. J. Tyler, C. Weder. *Nat. Nanotechnol.* **2007***, 2*, 765–769.

44. M. Iguchi, S. Yamanaka, A. Budhiono. *J. Mater. Sci.* **2000**, *35*, 261–270.

45. Y. Nishi, M. Uryu, S. Yamanaka, K. Watanabe, N. Kitamura, M. Iguchi, S. Mitsuhashi. *J. Mater. Sci.* **1990**, *25*, 2997–3001.

46. S. Yamanaka, K. Watanabe, N. Kitamura, M. Iguchi, S. Mitsuhashi, Y. Nishi, M. Uryu. *J. Mater. Sci.* **1989**, *24*, 3141–3145.

47. G. Guhados, W. Wan, J. L. Hutter. *Langmuir* **2005**, *21*, 6642–6646.

48. Y. –C. Hsieh, H. Yano, M. Nogi, S. Eichhorn. *Cellulose* **2008**, *15*, 507–513.

49. K. Watanabe, M. Tabuchi, Y. Morinaga, F. Yoshinaga. *Cellulose* **1998**, *5*, 187–200.

50. A. Nakagaito, S. Iwamoto, H. Yano. *Appl. Phys. A: Mater. Sci. Process.* **2005**, *80*, 93–97.

51. M. Nogi, H. Yano. *Adv. Mater.* **2008**, *20*, 1849–1852.

52. H. Yano, J. Sugiyama, A. Nakagaito, M. Nogi, T. Matsuura, M. Hikita, K. Handa. *Adv. Mater.* **2005**, *17*, 153–155.

53. K. Qiu, A. N. Netravali. *Polym. Rev.* **2014**, *54*, 598–626.

54. N. Shah, M. Ul-Islam, W. A. Khattak, J. K. Park. *Carbohydr. Polym.* **2013**, *98*, 1585–1598.

55. F. Liebner, E. Haimer, M. Wendland, M. A. Neouze, K. Schlufter, P. Miethe, T. Heinze, A. Potthast, T. Rosenau. *Macromol. Biosci.* **2010**, *10*, 349–352.

56. H. S. Barud, C. Barrios, T. Regiani, R. F. Marques, M. Verelst, J. Dexpert-Ghys, Y. Messaddeq, S. J. Ribeiro. *Mater. Sci. Eng., C* **2008**, *28*, 515–518.

57. H. W. Liang, Q. F. Guan, L. T. Song, H. B. Yao, X. Lei, S. H. Yu. *NPG Asia Mater.* **2012**, *4*, e19.

58. Z. Y. Wu, C. Li, H. W. Liang, J. F. Chen, S. H. Yu. *Angew. Chem.* **2013**, *125*, 2997–3001.

59. R. T. Olsson, M. A. Samir, G. Salazar-Alvarez, L. Belova, V. Ström, L. A. Berglund, O. Ikkala, J. Nogués, U. W. Gedde. *Nat. Nanotechnol.* **2010**, *5*, 584.

60. A. Nakayama, A. Kakugo, J. P. Gong, Y. Osada, M. Takai, T. Erata, S. Kawano. *Adv. Funct. Mater.* **2004**, *14*, 1124–1128.

61. A. Svensson, E. Nicklasson, T. Harrah, B. Panilaitis, D. L. Kaplan, M. Brittberg, P. Gatenholm. *Biomaterials* **2005**, *26*, 419–431.

62. E. C. Peters, F. Svec, J. M. Fréchet. *Adv. Mater.* **1999**, *11*, 1169–1181.

63. H. Zou, X. Huang, M. Ye, Q. Luo. *J. Chromatogr., A* **2002**, *954*, 5–32.

64. G. Guiochon. *J. Chromatogr., A* **2007**, *1168*, 101–168.

65. K. Liu, P. Aggarwal, J. S. Lawson, H. D. Tolley, M. L. Lee. *J. Sep. Sci.* **2013**, *36*, 2767–2781.

66. J. Urban, P. Jandera. *Anal. Bioanal. Chem.* **2013**, *405*, 2123–2131.

67. F. Svec, Y. Lv. *Anal. Chem.* **2015**, *87*, 250–273.

68. N. Tanaka, D. V. McCalley. *Anal. Chem.* **2016**, *88*, 279–298.

69. F. Svec. *J. Chromatogr. A* **2010**, *1217*, 902–924.

70. K. Sakakibara, H. Kagata, N. Ishizuka, T. Sato, Y. Tsujii. *J. Mater. Chem. A* **2017**, *5*, 6866–6873.

71. F. Svec, J. M. Frechet. *Science* **1996**, *273*, 205–211.

72. N. A. Mai, N. T. Duc, K. Irgum. *Chem. Mater*. **2008**, *20*, 6244–6247

73. N. Tsujioka, N. Hira, S. Aoki, N. Tanaka, K. Hosoya. *Macromolecules* **2005**, *38*, 9901–9903.

74. N. Tsujioka, N. Ishizuka, N. Tanaka, T. Kubo, K. Hosoya. *J. Polym. Sci., Part A: Polym. Chem.* **2008**, *46*, 3272–3281.

75. K. Sakakibara, K. Konishi, N. Ishizuka, A. Goto, Y. Tsujii. *Polym. Chem.* **2018**, *9*, 414–419.

76. Y. Mi, W. Zhou, Q. Li, D. Zhang, R. Zhang, G. Ma, Z. Su. *RSC Adv*. **2015**, *5*, 55419–55427.

77. J. Li, Z. Du, H. Li, C. Zhang. *Polymer* **2009**, *50*, 1526–1532.

78. J. Li, Z. Du, H. Li, C. Zhang. *J. Polym. Sci., Part B: Polym. Phys*. **2010**, *48*, 2140–2147.

79. T. Kubo, Y. Tominaga, K. Yasuda, S. Fujii, F. Watanabe, T. Mori, Y. Kakudo, K. Hosoya. *Anal. Methods* **2010**, *2*, 570–574.

80. Y. Liu, L. Wang. *Compos. Struct.* **2015**, *128*, 274–283.

81. L. Wang, J. Lau, E. L. Thomas, M. C. Boyce. *Adv. Mater.* **2011**, *23*, 1524–1529.

82. O. Al-Ketan, M. A. Assad, R. K. Al-Rub. *Compos. Struct.* **2017**, *176*, 9–19.

83. J. H. Lee, L. Wang, M. C. Boyce, E. L. Thomas. *Nano lett*. **2012**, *12*, 4392–4396.

84. K. Hosoya, H. Hira, K. Yamamoto, M. Nishimura, N. Tanaka. *Anal. Chem*. **2006**, *78*, 5729–5735.

85. N. P. Dinh, Q. M. Cam, A. M. Nguyen, A. Shchukarev, K. Irgum. *J. Sep. Sci.* **2009**, *32*, 2556–2264.

86. A. M. Nguyen, K. Irgum. *Chem. Mater.* **2006**, *18*, 6308–6315.

87. M. T. Gokmen, F. E. Du. Prez. *Prog. Polym. Sci.* **2012**, *37*, 365–405.

88. B. Wang, P. Prinsen, H. Wang, Z. Bai, H. Wang, R. Luque, J. Xuan. *Chem. Soc. Rev.* **2017**, *46*, 855–914.

Part 1

Bacterial Cellulose Nanofiber Network

Chapter 2

Fabrication, Structure and Mechanical Property of Resin Matrix-based Nanocomposites

2-1. Introduction

Cellulose nanofiber (CNF) produced from biomass resources such as woods and plants is microfibril with a diameter of several to 50 nm and a length of several micrometers. CNF is obtained either by the mechanical or chemical treatment. Mechanical disintegration of wood pulps in water slurries contains grinder treatment,[1] repeated-high pressure homogenization,[2, 3] aqueous counter collision method,[4] and so on. Chemistry-assisted disintegration contains the 2,2,6,6-tetramethylpiperidine-1-oxyl radical (TEMPO)-mediated oxidation/disintegration method.[5] The most important characteristic of CNF is the remarkable mechanical properties such as high Young's modulus (140 GPa[6, 7]) and strength (2−6 GPa[8]) along the longitudinal direction. Furthermore, CNF has high aspect ratio, having potential superiority as reinforcement fillers for matrix such as polyolefin, polystyrene, and poly(meth)acrylates. However, since CNF has hydrophilic nature on surface, perfect dispersion in these matrices is quite difficult unless the surface nature is changed to be hydrophobic either by chemical modification of hydrophobic groups[9] or physical adsorption of surfactants or polymers[10–12] in order to suppress sever inter- or intramolecular hydrogen bonds among CNFs. Recently, another approach successfully utilizes a preformed CNF network, as exemplified by immersion precipitation of matrix solution with CNFs,[13] casing and drying matrix solution with CNF dispersion in organic solvents,[14–16] sol-gel process with precipitation of CNF suspension to poor solvents and polymer impregnation[17, 18] and in situ polymerization.[19]

Bacterial cellulose (BC), produced by the bacterium Acetobacter xylinus cultivated in a culture medium, is naturally-occurring CNF with cross-sections of ca. 4 × 80 nm and length of several μm.[20] BC has high crystallinity (more than 70%)[21] similar to other cellulosic resources.[22] Therefore, BC also has high mechanical properties,[23–26] and indeed have been utilized as a reinforcement filler.[27] Yano and coworkers have prepared BC composites by compressing and freeze drying of BC gels, following polymer impregnation.[28, 29] Importantly, the original BC gel possesses highly fine and pure CNF network, whose self-standing structure is maintained in spite it contains only less than 1% of BC because of the high aspect ratio and the entanglement. Besides because CNFs are able to be dispersed without modification of CNF or adsorption of additive to CNF, hence, the reinforcement effect of CNF network will be verified experimentally by estimating the mechanical properties of BC gel embedded with polymer matrix. Therefore, we think that CNF network structure in BC gels is expected to be a best choice not only for ideal composites but also for understanding of reinforcement mechanisms by network structure.

Network structure, which consisted of struts, crosslinks and space, was mechanically characterized by deformation behavior of the struts including stretching and bending. The modulus of the network was proportional to its density with scaling exponents depended on the deformation modes. Scaling exponent close to 1 was indicated stretch-dominated deformation behavior of the struts, whereas exponent close to 2 was indicated bend-dominated deformation.[30–32] The deformation behavior of the network structure embedded in matrices was also discussed which provided important information to characterize mechanical properties of both the network structure and composites.[33, 34]

Here, we demonstrate a new approach for preparation of a well-defined BC nanofiber network-reinforced composite material and reveal the superior reinforcement mechanism. At first, the BC/PMMA composites maintained CNF network structure were successfully prepared via

stepwise solvent exchange from water to MMA, followed by free radical polymerization. The CNF network in composites was estimated by confocal laser scanning microscopy (CLSM) observation with fluorescent labelled BC. In second, to reveal the effectiveness of CNF reinforcement, mechanical properties were evaluated by nano-indentation measurements, which provided modulus in submicron scale. This measurement is useful as compared to conventional macroscopic compression measurements, since the latter is always influenced by local defects such as voids or aggregation. At summary, we focused on the deformation behavior of BC nanofiber network in matrices for the guideline toward network-reinforced composite materials.

2-2. Experimental Section

2-2-1. Materials

Bacterial cellulose (BC) hydrogel was purchased from Fujicco Co. Ltd. and purified according to procedures detailed in the literature.[35] Methyl methacrylate (MMA) (99% Nacalai Tesque Inc., Kyoto, Japan) was purified by passing through a column filled with activated basic alumina to remove the polymerization inhibitor. 2,2'-Azobisisobutyronitrile (AIBN) (99%, Wako Pure Chemical Industries, Ltd., Osaka, Japan) was purified by recrystallization and used as an initiator for free radical polymerization. Tetrahydrofuran (THF) (99%, Nacalai), di-n-butyltin dilaurate (90 %, Wako), rhodamine B isothiocyanate (RITC) (mixed isomers, Sigma-Aldrich), fluorescein isothiocyanate (FITC) (90%, Sigma-Aldrich) and molecular sieves 3A (Wako) were used as received. Deionized water was used for all aqueous solutions. THF used in chromatography was distilled before use.

2-2-2. Preparation of BC/PMMA Composites

Figure 2-1 shows the method for the preparation of BC/PMMA composites, containing two steps: (i) solvent exchange treatment for the BC hydrogels from water to MMA via THF, and (ii) free radical polymerization of MMA. To control BC content, the BC/MMA gel was compressed to arbitrary size, followed by free radical polymerization.

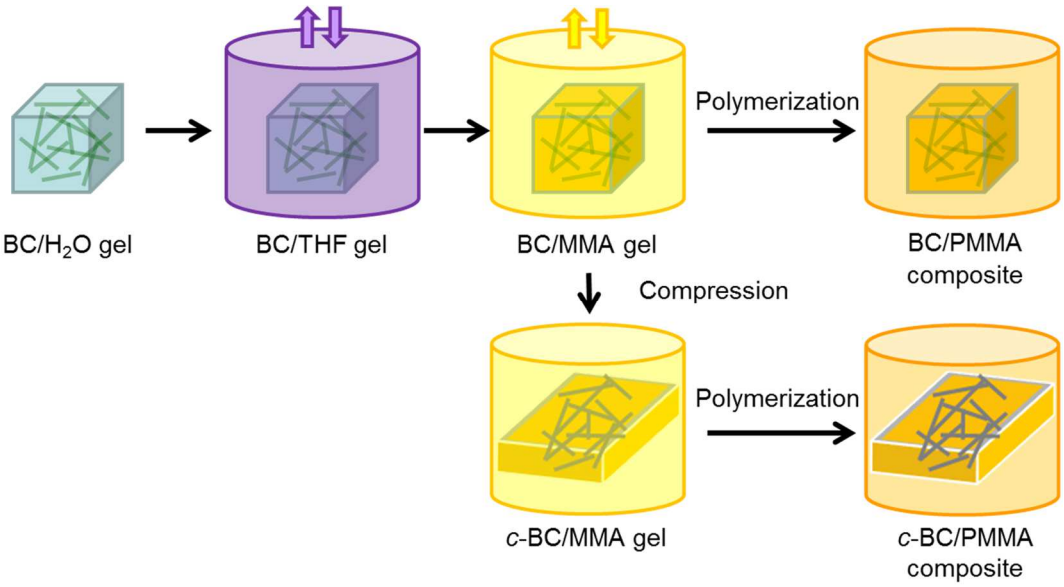

Figure 2-1. Schematic illustration for the preparation of BC/PMMA composite materials.

Direct Solvent Exchange

A BC/H_2O was added in nine-fold amount of MMA in the presence of molecular sieves 3A not to touch with each other and agitated for 24 hours with a shaking apparatus (EYELA Multi Shaker MMS, Tokyo Rikakikai Co., Ltd., Tokyo, Japan).

Stepwise Solvent Exchange

First, nine-fold amount of THF was added to the purified BC/H_2O gel and agitated for 12 hours with the shaking apparatus. This treatment was carried out three times, then, any residual water was removed using a Soxhlet extractor with THF for 6 h, yielding a BC/THF gel. Next, nine-fold amount of MMA was added to the BC/THF gel and agitated in the same manner. This treatment was

performed three times, yielding a BC/MMA gel. Weight fraction of BC in the BC/H_2O and BC/MMA gels was estimated from the weight of BC gels and dry weight of BC gels, then, converted to the volume fraction on the basis of the density of BC (the values shown in Table 2-1). The molar fractions of water, THF and MMA in the BC/MMA gel were estimated by ^{1}H-NMR analysis.

Free Radical Polymerization of MMA

The BC/MMA gel soaked in MMA solution with 5.0×10^{-3} mol% of AIBN was placed into a test tube with a three-way cock. The test tube was degassed under reduced pressure for several seconds, then, the argon gas was filled. This treatment was carried out 20 times, then the test tube was placed in an oil bath at 60 °C for 12 h, then at 70 °C for 12 h, finally at 100 °C for 12 h, according to the method for the preparation of defect-free PMMA bulk materials.[36] After the polymerization, the BC/PMMA composite was trimmed. The free PMMA was characterized by GPC and ^{1}H-NMR.

Compression of the BC/MMA Gel and Free Radical Polymerization

The weight and volume fractions of cellulose were controlled by compressing the BC/MMA gels using the stainless 300 mesh sheets on the glass plates in the direction perpendicular to the layer structures of the BC gel derived from the activity of the bacterium near the surface of culture medium,[20, 24] yielding a compressed BC/MMA (*c*-BC/MMA) gel. The free radical polymerization of MMA was conducted in a same manner as above, except the compressed BC/MMA gel was in between the glass plates to avoid decompression, to yield *c*-BC/PMMA composites.

2-2-3. Fluorescent Labelling of BC

FITC (1 wt%) dissolved in acetone was added into the BC hydrogel and agitated for 14 h with a shaking apparatus, then, the BC hydrogel was washed repeatedly with water to remove unadsorbed FITC, yielding a fluorescent labeled BC/H_2O gel.

RITC (1 wt%) and a catalytic amount of di-*n*-butyltin dilaurate dissolved in acetone were mixed with BC/THF gel and agitated for 3h at 50 °C with a shaking apparatus.[37] Then, the BC/THF gel was washed repeatedly with THF to remove unreacted RITC. Nine-fold amount of MMA was added to the BC/THF gel and agitated in the same manner. This treatment was performed three times, yielding a fluorescent labeled BC/MMA gel. Free radical polymerization was conducted in the same way as above, yielding a fluorescent labeled BC/PMMA composite.

2-2-4. Surface Polishing of BC/PMMA Composites

For the confocal laser scanning microscopic (CLSM) observation and the nano-indentation measurement, PMMA and BC/PMMA composites were cleaved and the surface was polished with abrasive papers in order of #1000, #2000, #4000 in water in order to suppress deformation by heat of friction. The polished surface was observed by a 3D laser scanning confocal microscope (KEYENCE, VK-X). Average roughness (R_a) on the surface was from 25 to 100 nm which is smaller enough than tip contact depth for nano-indentation measurement.

2-2-5. Characterization

To determine the number-average molecular weight (M_n), weight-average molecular weight (M_w), and polydispersity index (M_w/M_n), a gel permeation chromatographic (GPC) analysis was carried out with a Shodex GPC-101 high speed liquid chromatography system equipped with a guard column (Shodex GPC KF-G), two 30-cm mixed columns (Shodex GPC KF-806L, exclusion limit = 2×10^7), and a differential refractometer (Shodex RI-101). THF was used as an eluent at a flow rate of 0.8 mL/min. The GPC system was calibrated by poly (methyl methacrylate) (PMMA) standards (Polymer Laboratories, M_p = 1.31×10^3 - 1.64×10^6), and M_n and M_w/M_n were calculated as PMMA-calibrated values. ^{1}H-NMR spectra were recorded on JNM-ECA600 (JEOL, Tokyo, Japan)

(600 MHz) using deuterated chloroform as the solvent. Chemical shifts relative to tetramethylsilane (TMS) as an internal standard are given in δ values. Confocal laser scanning microscopic (CLSM) observation was carried out by an inverted-type microscope (LSM 5 PASCAL, Carl Zeiss, Germany) with a 532-nm wavelength laser and ×63 objective lens (Plan Apochromat, Carl Zeiss) in reflection mode. The contrast and brightness of the CLSM images were adjusted by common software.

Nano-indentation experiments were carried out to determine indentation modulus for the depth from the surface of the PMMA and BC/PMMA composites using Nano Indenter G200 (Agilent Technologies Inc.) with a Berkovich type indentation tip. The continuous stiffness measurement (CSM) was carried out to continuously obtain depth profile of modulus up to a depth of about 8000 nm with 45Hz of frequency, 2 nm of oscillation and 0.05 s^{-1} of strain rate. Surface of samples was determined to detect 200 N/m of stiffness. Calibration of blunting of the indentation tip and calculation of modulus is based on the Oliver-Pharr method.[38] Nano-indentation experiments were conducted from 5 to 15 indents for each sample, exceptionally 29 indents for *c*-BC/PMMA-0.8 in the edge direction in order to confirm uniformity of BC in wide range of area and 4 indents for *c*-BC/PMMA-19 in the edge direction because of small cross-sectional area by compression of BC. Some indents were failed to detection of surface. The modulus at a specific depth was calculated on average. The distance between indents was longer than 400 μm to prevent influences from the other indents. Poisson ratio of PMMA and BC/PMMA composites was assumed 0.3.

Attenuated total reflection infrared (ATR-IR) spectra were recorded on a Nicolet 670SX FT-IR (Thermo Fisher Scientific Inc.) spectrophotometer equipped with a MCT detector and a Specac Golden Gate single reflection attenuated total reflectance (ATR) accessory (germanium crystal with incident angle of 45°). All data were collected at a spectral resolution of 4 cm^{-1}. The weight/ volume

fraction of BC in the *c*-BC/PMMA composites was estimated by calibration curve of ATR-FTIR analysis.

The modulus of a BC/H_2O gel was estimated from gradients of tangent at stress-true strain curve of its compression measurement with disk-shape of 4.2 mm in radius and 1.7 mm in thickness at a speed of 0.01 mm/s. Volume fraction of BC was estimated from compression strain. Surface area of a BC/H_2O gel was assumed constant due to exuding water.

2-3. Results and Discussion

2-3-1. Preparation of well-defined BC/PMMA Composites

At first, we tried the direct exchange from water in BC/H_2O gels to MMA, however, because of immiscibility of water with MMA, the BC gel was shrunk. Subsequently, solvent exchange via THF, which was miscible with both water and MMA, was tried (Figure 2-1). Table 2-1 shows the composition of the BC/H_2O and BC/MMA gels. The volume fraction of the BC in BC/H_2O and BC/MMA gels was almost the same. In addition, contents of water and THF were slight in the BC/MMA gel, indicating solvent exchange giving a well-defined BC/MMA gel was in successful.

Table 2-1. Compositions of the BC/H_2O and BC/MMA gels. [a]

	Weight fraction (%) / Volume fraction (%)			
	BC	H_2O	THF	MMA
BC/H_2O gel	0.51 / 0.34	99.49 / 99.66	0	0
BC/MMA gel	0.49 / 0.31	Trace	0.65 / 0.69	98.86 / 99.0

[a]Densities of BC,[39] THF and MMA were assumed to be 1.5, 0.89 and 0.94 g/cm^3, respectively.

Radical polymerization was carried out for the BC/MMA gel as well as MMA in bulk. From appearance of Figure 2-2, free defect of BC/PMMA composite embedded in PMMA was prepared. Table 2-2 shows the monomer conversion, M_w and M_w/M_n of thus obtained PMMA and BC/PMMA composites. M_w and monomer conversions of PMMA in the composite were similar to those of PMMA prepared in bulk, indicating little effect on radical polymerization by the BC network and other impurities contained in the original gel.

Figure 2-2. Picture of the BC/PMMA-0.3 composite embedded in PMMA.

Table 2-2. Characterization of PMMA and the BC/PMMA composite.

	$M_w/10^6$	Conversion (%)	M_w/M_n
PMMA	6.3	98.7	2.3
BC/PMMA-0.3[a]	7.8	98.8	2.1

[a]BC/PMMA-0.3 means BC/PMMA composite with 0.3 vol% of BC.

In order to visualize the BC network through the stepwise solvent exchanges and free radical polymerization, the fluorescent-labeled BC/H_2O gel, the BC/THF gel and the BC/PMMA composites were subjected to CLSM observation (Figure 2-3). In these images, the BC was visible as blue or red colors, which were derived from emission of FITC and RITC functionalities. BC was distributed homogeneously and formed network in PMMA. The diameter of the BC was approximately 200 nm, which was overestimate owing to the resolution limit set by the diffraction light, therefore the distance between fibers was focused. The observable maximum distance between BC in the composite was estimated as a few micro meters, similar to the BC/H_2O gel or the BC/MMA gel, indicating successful immobilization of BC network without BC aggregation was attained. Figure 2-3 (d) shows a CLSM image of a compressed BC/PMMA composite with 3.7 vol% of BC (*c*-BC/PMMA-3.7). Homogeneous BC network was observed similar to the uncompressed BC/PMMA composite and distance between BCs was smaller than that of the uncompressed BC/PMMA composite.

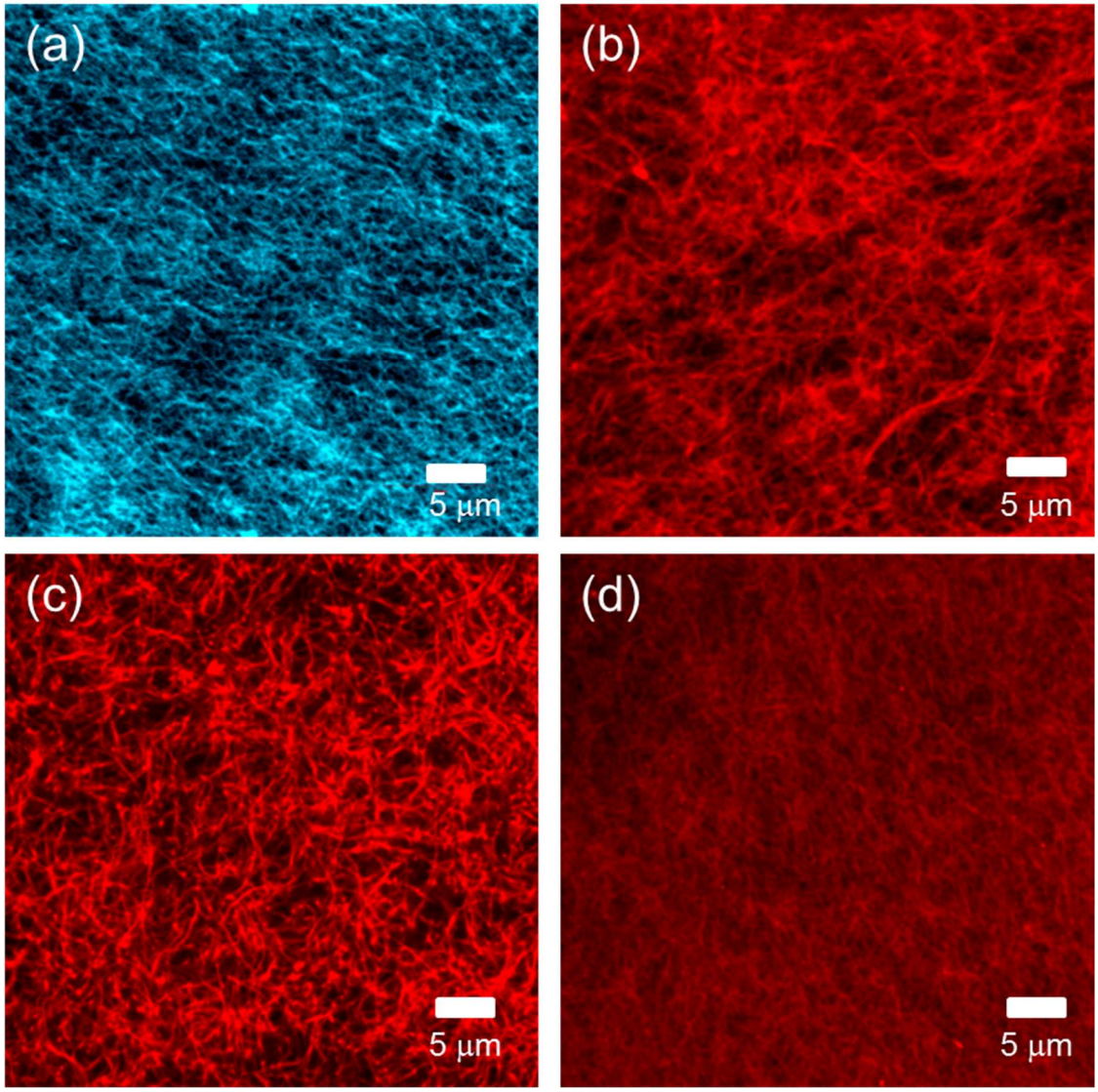

Figure 2-3. CLSM images of BC network; (a) BC/H_2O gel, (b) BC/THF gel, (c) BC/PMMA-0.3 composite and (d) *c*-BC/PMMA-3.7 composite.

2-3-2. Mechanical Properties of the BC/PMMA Composites

Figure 2-4 (a) shows plots of indentation modulus of PMMA and BC/PMMA-0.3 on the edge and face sides of BC at ranging from surface to 8000 nm contact depth. Indentation modulus at shallow contact depths was smaller than the deeper region because of the influence of roughness and damage of the BC and PMMA on the surface by polishing. The indentation modulus became constant values

at 7000–8000 nm contact depth, so that the average value in this area was defined as the elastic modulus of the samples. The elastic modulus of PMMA in bulk was suggested to be appropriate from previously reported.[40] The difference of the modulus between neat PMMA and BC/PMMA-0.3, that is, the reinforcement effect, was calculated to be 0.3 GPa, indicating significant difference because this value was consistent with the fitting line between the modulus of BC network and BC contents described later (Figure 2-5). Figure 2-4(b), (c) and (d) showed the nano-indentation results for *c*-BC/PMMA-0.8, 3.7, 19 vol%, which were shown similar tendency of BC/PMMA-0.3 and being constant at 7000–8000 nm, indicating the definition of elastic moduli was appropriated. Table 2-3 shows the elastic modulus of PMMA and the BC/PMMA composites with various contents of BC. The elastic modulus of *c*-BC/PMMA on edge side was more or less higher than those of composites on face side. This is because of the in-plane orientation of BC upon compression in the direction parallel to the layer structure.

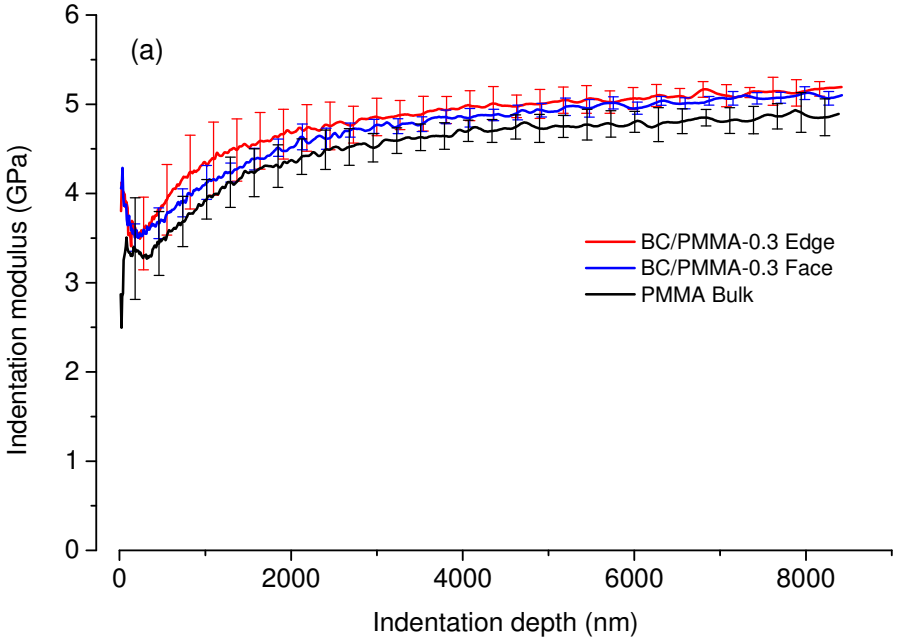

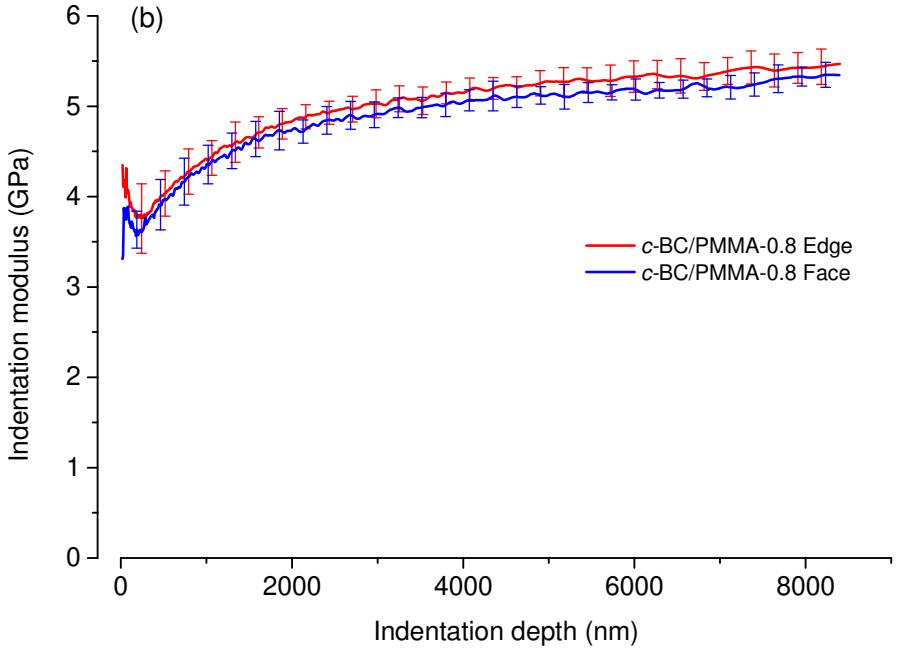
(b)
Indentation modulus (GPa)
Indentation depth (nm)
c-BC/PMMA-0.8 Edge
c-BC/PMMA-0.8 Face
0
1
2
3
4
5
6
0
2000
4000
6000
8000

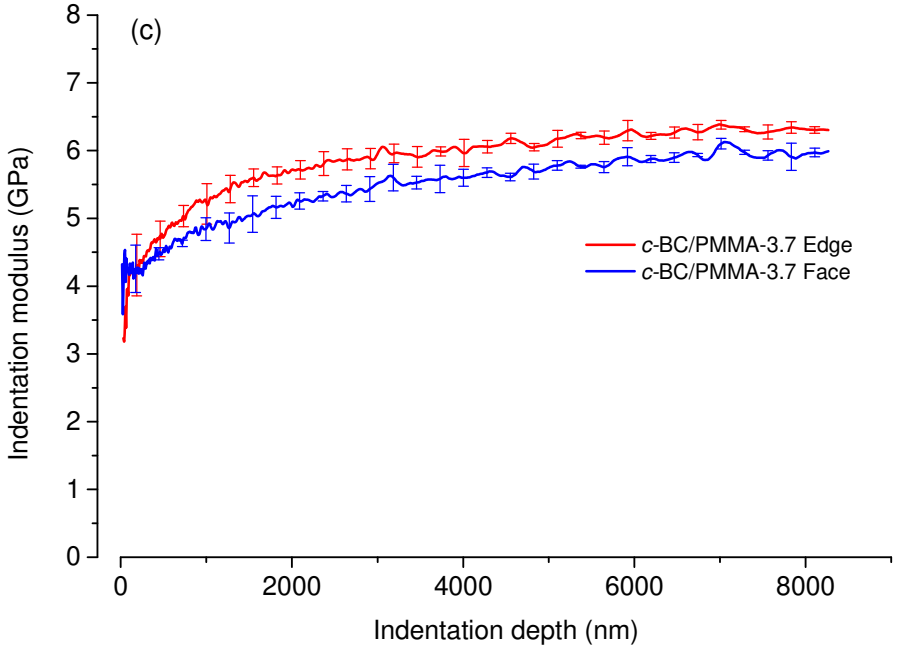
(c)
Indentation modulus (GPa)
Indentation depth (nm)
c-BC/PMMA-3.7 Edge
c-BC/PMMA-3.7 Face
0
1
2
3
4
5
6
7
8
0
2000
4000
6000
8000

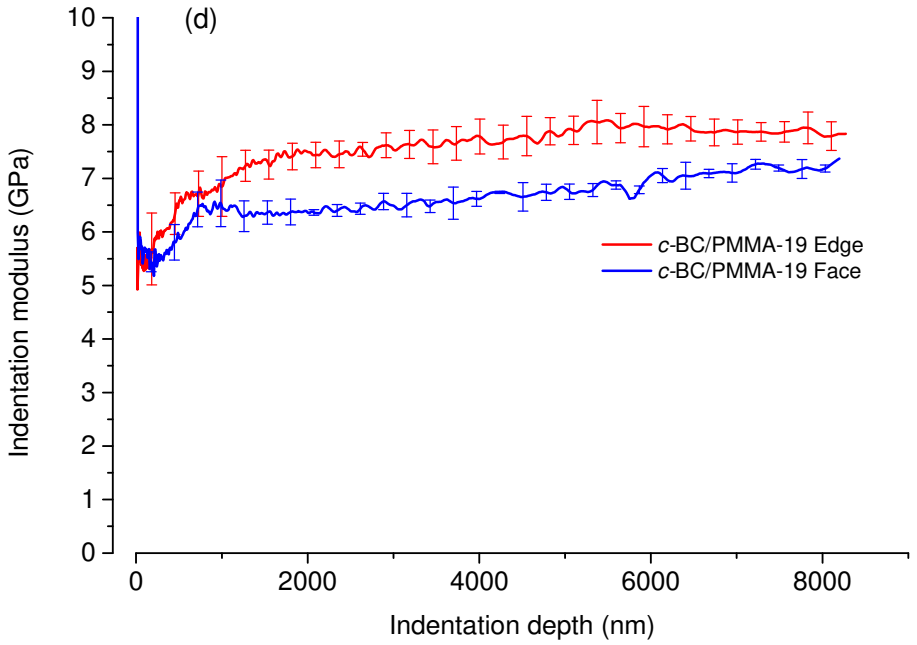

Figure 2-4. Averaged indentation modulus of (a) PMMA and BC/PMMA-0.3, (b) *c*-BC/PMMA-0.8, (c) *c*-BC/PMMA-3.7 and (d) *c*-BC/PMMA-19 composites in face and edge directions versus indentation depth. Standard deviation was given by error bars.

Table 2-3. Averaged indentation modulus and standard deviation of PMMA and the BC/PMMA composites at a range of indentation depth of 7000–8000 nm

Composites	Volume fraction of BC (vol%)	Elastic modulus (GPa)	
		Edge	Face
PMMA	0	4.8 ± 0.1	
BC/PMMA-0.3	0.3	5.1 ± 0.1	5.1 ± 0.1
c-BC/PMMA-0.8	0.8	5.4 ± 0.2	5.3 ± 0.1
c-BC/PMMA-3.7	3.7	6.3 ± 0.0	6.0 ± 0.0
c-BC/PMMA-19	19	7.9 ± 0.2	7.3 ± 0.3

Here, we discuss the BC network structure embedded in the composites and its reinforcement effect on mechanical properties. We assumed that the BC network was periodically entangled with high connectivity but not connectivity was depended on the volume fraction,[41, 42] as can be seen in Figure 2-3, showing the BC network was homogenously and continuously entangled at only 0.3 vol% of BC.

It has been reported that the relative modulus of network with similar geometry is scaled as $E \sim \rho^n$, in general, where, E and ρ are the relative modulus and density of a network, respectively.[30, 31] Scaling exponent n close to 1 indicates mainly expansion or contraction behavior of fibers in the axial direction, i.e. stretch-dominated deformation, whereas exponent n close to 2 indicates mainly bending behavior of fibers in the lateral direction, i.e. bend-dominated deformation. Exponent n larger than 2 indicates some parts in the network are inefficient for load transfer due to inhomogeneity of the network such as defects, loop, or dangling of chains. We adapted this model in thus obtained composites.

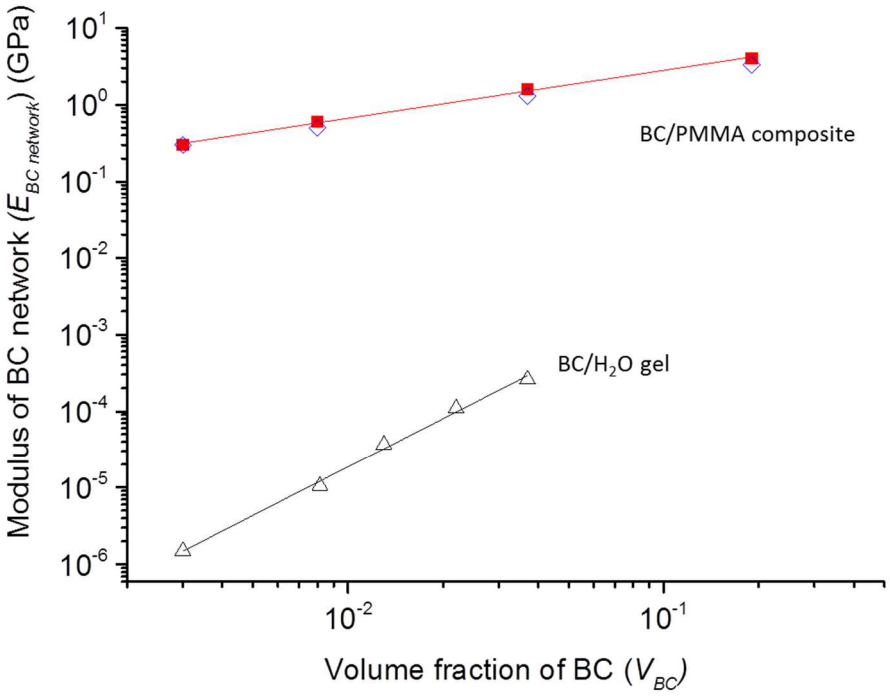

Figure 2-5. Double logarithmic plots of the modulus of BC network estimated for BC/PMMA composites in face (open squares) and edge (closed squares) directions and a BC/H_2O gel (open triangles) versus volume fraction of BC. Red and black lines represent prediction of moduli in edge direction of the BC/PMMA composites and the BC/H_2O gel by linear fitting, respectively.

Table 2-4. Parameters for fitting line of BC/PMMA composites and a BC/H_2O gel in Figure 2-5.

	Slope n	$E_{BC\ bulk}$ (GPa)
BC/PMMA composites	0.62	13
BC/H_2O gel	2.1	0.30

Figure 2-5 shows double logarithmic plots of modulus of the BC network ($E_{BC\ network}$) estimated for BC/PMMA composites and BC/H_2O gel versus volume fraction of BC. The elastic modulus of BC network in composites ($E_{BC\ network}$) was estimated as follow based on the rule of mixtures.

$$E_{BC\ network} = E_c - E_m(1 - V_{\mathrm{BC}}) \quad (2\text{-}1)$$

where, E_c and E_m were the elastic modulus of a BC/PMMA composite and PMMA and V_{BC} was the volume fraction of the BC network. The $E_{BC\ network}$ linearly increased with the increase of the volume fraction of BC. Lines in Figure 2-6 were prediction of $E_{BC\ network}$ and slope n and the modulus of BC bulk ($E_{BC\ bulk}$) predicted from the extrapolation of linear fitting was shown in Table 2-4. Subsequently, the elastic modulus of BC bulk ($E_{BC\ bulk}$) was estimated as below,

$$E_{BC\ bulk} = \eta\, E_{BC\ fiber} \quad (2\text{–}2)$$

where, $E_{BC\ fiber}$ was the modulus along the longitudinal direction of the BC nanofibers, assumed 114 GPa in the literature.[26] η was efficiency factor derived from degree of orientation, estimated as below in the case randomly oriented fibers,[43, 44]

$$\eta = \int_0^{\pi/2} \sin\theta \cos^4\theta d\theta = 1/5 \quad (2\text{–}3)$$

From the equation (2) and (3), theoretically estimated $E_{BC\ bulk}$ was 23 GPa, which was roughly consistent with thus estimated the $E_{BC\ bulk}$ from the linear fitting in Table 2-4.

Subsequently, exponent n for BC/PMMA composites was estimated 0.62 close to 1, which was much smaller than that for BC/H_2O gel, indicating the BC network behaved as mainly stretch-dominated deformation and the load was effectively transferred. In addition, the aggregation or deformation of the BC network associated with inefficient load transfer did not occurred. Furthermore, it should be noted that bend-dominated deformation of BC network was suppressed in spite of the looped structure of BC network. These results suggest that bend-deformation of BC network was suppressed by the lateral reinforcement of matrix, otherwise the segment of matrix was needed to be forced large and heterogeneous deformation.[45] In the present system, deformation modes of both BC network and matrix were remarkably limited by homogenously embedded nanofiber fine networks, enabling the ideal reinforcement of composites with only slight of BC

contents. The understanding of the deformation mode of network would lead to guideline toward network-reinforced composite materials.

2-4. Conclusion

We successfully prepared ideal BC/PMMA composites reinforced with well-defined fine BC nanofiber network structure and demonstrated effectively high mechanical properties predicted theoretically from the elastic modulus of BC by the nano-indentation experiments. These composites were prepared by "in situ stepwise solvent exchanges and polymerization", in which BC hydrogels were placed MMA via THF and free radical polymerization of MMA using initiator. The CLSM images of BC gels and BC/PMMA composites showed that the networks in BC/PMMA composites were maintained homogenous distribution. In addition, we revealed the reinforcement mechanisms by network structure. The BC nanofiber network was forcefully behaved stretch-dominated deformation in PMMA matrix instead of bend-dominated deformation, and effective load transfer. Thus restricted stretch deformation was attained derived from both reinforcement of the fine BC network and the lateral reinforcement of matrix, in spite of the looped structure and only slight amount of BC network. Understanding thus phenomenon in matrices would give guidelines for design mechanically controlled composites with network structures.

2-5. References

1. K. Abe, S. Iwamoto, S. Yano. *Biomacromolecules* **2007**, *8*, 3276–3278.

2. A. F. Turbak, F. W. Snyder, K. R. Sandberg. *J. Appl. Polym. Sci.: Appl. Polym. Symp.* **1983**, *37*, 815–827.

3. H. Yano, S. Nakahara. *J. Mater. Sci.* **2004**, *39*, 1635–1638.

4. T. Kondo, R. Kose, H. Naito, W. Kasai. *Carbohydr. Polym.* **2014**, *112*, 284–290.

5. T. Saito, Y. Nishiyama, J. -L. Putaux, M. Vignon, A. Isogai. *Biomacromolecules* **2006**, *7*, 1687–1691.

6. I. Sakurada, Y. Nukushina, T. Ito. *J. Polym. Sci.* **1962**, *57*, 651–660.

7. T. Nishino, K. Takano, K. Nakamae. *J. Polym. Sci., Part B: Polym. Phys.* **1995**, *33*, 1647–1651.

8. T. Saito, R. Kuramae, J. Wohlert, L. A. Berglund, A. Isogai. *Biomacromolecules* **2012**, *14*, 248–253.

9. A. Sato, D. Kabusaki, H. Okumura, T. Nakatani, F. Nakatsubo, H. Yano. *Composites, Part A* **2016**, *83*, 72–79.

10. K. Sakakibara, H. Yano, Y. Tsujii. *ACS Appl. Mater. Interfaces* **2016**, *8*, 24893–24900.

11. L. Petersson, I. Kvien, K. Oksman. *Compos. Sci. Technol.* **2007**, *67*, 2535–2544.

12. J. Kim, G. Montero, Y. Habibi, J. P. Hinestroza, J. Genzer, D. S. Argyropoulos, O. J. Rojas. *Polym. Eng. Sci.* **2009**, *49*, 2054–2061.

13. F. Fahma, N. Hori, T. Iwata, A. Takemura. *J. Appl. Polym. Sci.* **2013**, *128*, 1563–1568.

14. E. E. Kiziltas, A. Kiziltas, S. C. Bollin, D. J. Gardner. *Carbohydr. Polym.* **2015**, *127*, 381–389.

15. S. Fujisawa, T. Ikeuchi, M. Takeuchi, T, Saito, A. Isogai. *Biomacromolecules* **2012**, *13*, 2188–2194.

16. H. Dong, Y. R. Sliozberg, J. F. Snyder, J. Steele, T. L. Chantawansri, J. A. Orlicki, S. D. Walck, R. S. Reiner, A. W. Rudie. *ACS Appl. Mater. Interfaces* **2015**, *7*, 25464–25472.

17. J. R. Capadona, K. Shanmuganathan, S. Trittschuh, S. Seidel, S. J. Rowan, C. Weder. *Biomacromolecules* **2009**, *10*, 712–716.

18. J. R. Capadona, O. Van Den Berg, L. A. Capadona, M. Schroeter, S. J. Rowan, D. J. Tyler, C. Weder. *Nat. Nanotechnol*. **2007**, *2*, 765–769.

19. Z. Shi, J. Huang, C. Liu, B. Ding, S. Kuga, J. Cao, L. Zhang. *ACS Appl. Mater. Interfaces* **2015**, *7*, 22990–22998.

20. M. Iguchi, S. Yamanaka, A. Budhiono. *J. Mater. Sci.* **2000**, *35*, 261–270.

21. J. Sugiyama, R. Vuong, H. Chanzy. *Macromolecules* **1991**, *24*, 4168–4175.

22. K. Watanabe, M. Tabuchi, Y. Morinaga, F. Yoshinaga. *Cellulose* **1998**, *5*, 187–200.

23. Y. Nishi, M. Uryu, S. Yamanaka, K. Watanabe, N. Kitamura, M. Iguchi, S. Mitsuhashi. *J. Mater. Sci.* **1990**, *25*, 2997–3001.

24. Y. Nishi, M. Uryu, S. Yamanaka, K. Watanabe, N. Kitamura, M. Iguchi, S. Mitsuhashi. *J. Mater. Sci.* **1989**, *24*, 3141–3145.

25. G. Guhados, W. Wan, J. L. Hutter. *Langmuir* **2005**, *21*, 6642–6646.

26. Y.-C. Hsieh, H. Yano, M. Nogi, S. Eichhorn. *Cellulose* **2008**, *15*, 507–513.

27. S. Iwamoto, A. N. Nakagaito, H. Yano. M. Nogi. *Appl. Phys. A* **2005**, *80*, 93–97.

28. M. Nogi, H. Yano. *Adv. Mater.* **2008**, *20*, 1849–1852.

29. H. Yano, J. Sugiyama, A. N. Nakagaito, M. Nogi, T. Matsuura, M. Hikita, K. Handa. *Adv. Mater.* **2005**, *17*, 153–155.

30. L. J. Gibson, M. F. Ashby. *Cellular solids: structure and properties*. *Cambridge university press.* **1999**.

31. M. F. Ashby. *Philos. Trans. R. Soc., A* **2006**, *364*, 15–30.

32. C. P. Broedersz, X, Mao, T. C. Lubensky, F. C. MacKintosh. *Nat. Phys.* **2011**, *7*, 983–988.

33. L. Wang, L. Lau, E. L. Thomas, M. C. Boyce. *Adv. Mater*. **2011**, *23*, 1524–1529.

34. O. Al-Ketan, M. A. Assad, R. K. A. Al-Rub. *Compos. Struct.* **2017**, *176*, 9–19.

35. A. Hirai, O. Inui, F. Horii, M. Tsuji. *Langmuir* **2009**, *25*, 497–502.

36. A. Tsuchida, W. Sakai, M. Nakano, M. Yamamoto. *J. Phys. Chem.* **1992**, *96*, 8855–8858.

37. A. N. de Belder, K. O. Wik. *Carbohydr. Res.* **1975**, *44*, 251–257.

38. W. C. Oliver, G. M. Pharr. *J. Mater. Res.* **1992**, *7*, 1564–1583.

39. W. Gindl, J. Keckes. *Compos. Sci. Technol.* **2004**, *64*, 2407–2413.

40. B. Briscoe, L. Fiori, E. Pelillo. *J. Phys. D: Appl. Phys.* **1998**, *31*, 2395–2405.

41. M. Takayanagi, S. Uemura, S. Minami. *J. Polym. Sci., Part C: Polym. Symp.* **1964**, 113–122.

42. N. Ouali, J. Y. Cavaillé, J. Perez. *Plast., Rubber Compos. Process. Appl.* **1991**, *16*, 55–60.

43. H. Krenchel. *Fibre reinforcement; theoretical and practical investigations of the elasticity and strength of fibre-reinforced materials* **1964**.

44. R. Rusli, S. J. Eichhorn. *Appl. Phys. Lett.* **2008**, *93*, 033111.

45. C. P. Brangwynne, F. C. MacKintosh, S. Kumar, N. A. Geisse, J. Talbot, L. Mahadevan, K. K. Parker, D. E. Ingber, D. A. Weitz. *J. Cell Biol.* **2006**, *173*, 733–741.

Chapter 3

Fabrication, Structure and Mechanical Property of Elastomeric Matrix-based Nanocomposites

3-1. Introduction

Cellulose nanofiber (CNF) has remarkable physical properties including high elasticity (Young's modulus close to 140 GPa[1, 2]) and strength (2–6 GPa[3]) along the longitudinal direction, therefore, has great potential as a reinforcement filler for polymeric composites. However, because CNF has a hydrophilic surface, perfect dispersion in a hydrophobic matrix is quite difficult.

Bacterial cellulose (BC) gel is produced by the bacterium *Acetobacter xylinus*, and is composed of a ribbon-shaped CNF network with cross-sections of approximately 4×80 nm and lengths of several μm.[4] BC also has desirable mechanical properties, similar to the wood-derived CNF,[5-8] and has been utilized as a reinforcement filler for polymer composite materials.[9-11] In Chapter 2, we successfully embedded a well-defined original nanofiber network into a resin matrix via stepwise solvent exchange in a 0.3 vol%-BC hydrogel from water to hydrophobic monomers followed by *in situ* free radical polymerization.[12] The key to success was the use of tetrahydrofuran (THF) as a co-solvent during the solvent-exchange process, as it played a crucial role in inhibiting shrinkage. These obtained composites thus enabled a better understanding of the reinforcement properties of the CNF network.

In Chapter 3, an elastomer was selected as the matrix polymer. Fiber-reinforced elastomers have been used as engineering materials for energy absorbents. In fact, high-strength CNF-reinforced elastomers have been prepared via the conventional mixing method of a CNF slurry and matrix polymers or via *in situ* polymerization, and have exhibited high strength and improved stretching

properties.[13-15] However, it remains challenging to achieve homogenous dispersion of the nanofibers and to embed a well-defined nanofiber network as well as to clarify the detailed mechanism of reinforcement. Herein, we demonstrate the preparation of a crosslinked poly(ethyl acrylate) (PEA) composite with a well-defined BC nanofiber network by the approach in Chapter 2, and discuss their mechanical and structural features and reinforcement mechanism from a view point of large deformation of composites by tensile tests and microscopic analysis.

3-2. Experimental section

3-2-1. Materials

BC hydrogel (BC/H_2O gel) was purchased from Fujicco Co. Ltd. and purified according to procedures detailed in the literature.[16] The gel was sliced to a thickness of 2 mm parallel to the surface of its sheet by a razor blade. Ethyl acrylate (EA) (99%, Nacalai Tesque Inc., Kyoto, Japan) was purified by passing it through a column filled with activated basic alumina to remove the polymerization inhibitor. Ethylene glycol dimethacrylate (EGDMA) (97%, Wako Pure Chemical Industries, Ltd., Osaka, Japan), 2,2-dimethoxy-2-phenylacetophenone (DMPAP) (98%, Tokyo Chemical Industry Co., Ltd., Tokyo, Japan), di-*n*-butyltin dilaurate (90%, Wako), and rhodamine B isothiocyanate (RITC) (mixed isomers, Sigma-Aldrich) were used as received. Reagent-grade solvents were used for all extractions. Deionized water was used for all aqueous solutions. The THF used in the chromatography was distilled before use.

3-2-2. Preparation of BC/PEA composites

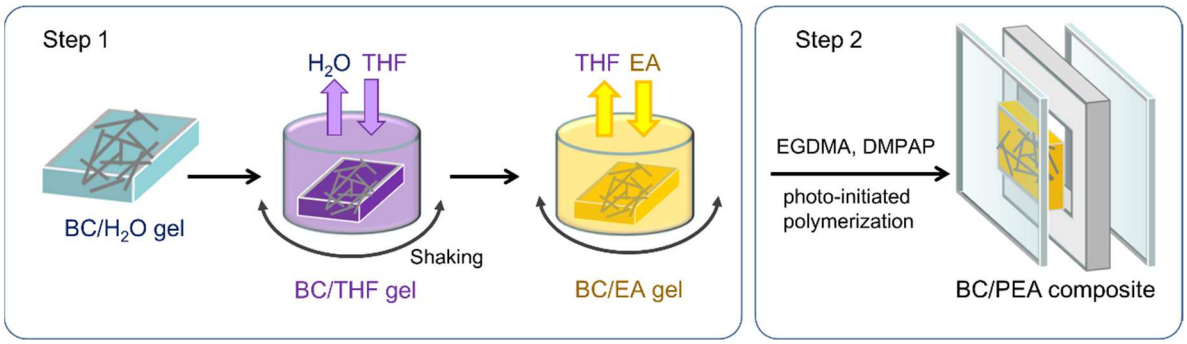

Figure 3-1. Schematic illustration of the preparation of BC/PEA composites.

BC/PEA composites were prepared by the following two steps (Figure 3-1): (i) solvent-exchange treatment of the BC hydrogels from water to EA via THF, and (ii) *in situ* photo-initiated free radical polymerization of EA. *Step 1: Solvent exchange.* A nine-fold amount of THF was added to the purified BC/H_2O gel and agitated for 24 h with a shaking apparatus (EYELA Multi Shaker MMS, Tokyo Rikakikai Co., Ltd., Tokyo, Japan). This was performed three times and any residual water was removed using a Soxhlet extractor with THF for 6 h, yielding a BC/THF gel. Next, a nine-fold amount of EA was added to the BC/THF gel and agitated in the same manner. This treatment was performed three times, yielding a BC/EA gel. The weight fraction of BC was estimated by weighing the sample before and after drying, and then converted to a volume fraction based on the density of BC. *Step 2: Free radical polymerization of EA.* The monomer in the BC/EA gel was replaced by a monomer mixture with 2.1×10^{-2} mol% of EGDMA and 8.2×10^{-3} mol% of DMPAP. The obtained gel was placed in a cell consisting of two glass plates with a 2-mm thick polytetrafluoroethylene spacer. Finally, the cell was filled with the same monomer mixture. The oxygen dissolved in the monomer mixture was removed by argon bubbling for 5 min. Then, the cell was placed 30 cm away from a 300 W Xe-lamp (MAX-301, Asahi spectra, Japan) equipped with a UV-cutoff filter (LUC300) and a rod lens (RLQ-1). The light intensity at the irradiation surface was measured with a power meter. The cell was irradiated at a power of 92 W/ m^2 for 14 h at approximately 25 °C to yield

the BC/PEA composite. The composite was dried under vacuum at approximately 25 °C overnight to remove any unreacted EA.

3-2-3. Preparation of the fluorescent labeled BC/PEA composites

RITC (1 wt%) and a catalytic amount of di-*n*-butyltin dilaurate dissolved in acetone were mixed with the BC/THF gel and agitated for 3 h at 70 °C with the shaking apparatus. The obtained fluorescent-labeled BC/THF gel was then washed repeatedly with THF and used in the same way as the above-mentioned non-labelled BC.

3-2-4. Characterization

To determine the number-average molecular weight (M_n), weight-average molecular weight (M_w), and polydispersity index (M_w/M_n), a gel permeation chromatographic (GPC) analysis was performed with a Shodex GPC-101 high speed liquid chromatography system equipped with a guard column (Shodex GPC KF-G), two 30 cm mixed columns (Shodex GPC KF-806L, exclusion limit = 2×10^7), and a differential refractometer (Shodex RI-101). THF was used as an eluent at a flow rate of 0.8 mL/min. The GPC system was calibrated with poly(methyl methacrylate) (PMMA) standards (Polymer Laboratories, M_p = 1.31×10^3–1.64×10^6), and the M_n and M_w/M_n were calculated as PMMA-calibrated values. ^{1}H-NMR spectra were recorded on a JNM-ECA600 instrument (JEOL, Tokyo, Japan, 600 MHz) using deuterated chloroform as the solvent. Chemical shifts relative to tetramethylsilane (TMS) as an internal standard are given in δ values. Confocal laser scanning microscopic (CLSM) observation was performed with an inverted-type microscope (LSM 5 PASCAL, Carl Zeiss, Germany) with a 532 nm wavelength laser and ×63 objective lens (Plan Apochromat, Carl Zeiss) in reflection mode. The contrast and brightness of the CLSM images were adjusted by a common software. Tensile tests were conducted using a universal testing machine

(Tensilon RTG-1310, A&D Co., Tokyo, Japan) with a 50 N load cell (UR-50N-D, A&D) at a test speed of 2 mm/min. The dumbbell specimens were prepared by a punching apparatus were 12 mm long, 2 mm wide, and 2 mm thick at the necked part. Thickness was measured using a digital length measuring system (DIGIMICRO, Nikon Co. Ltd., Japan). A non-contact video extensometer (TRView X, Shimadzu Co., Kyoto, Japan) was used for the determination of strain less than approximately 500%. The strain over 500% was estimated by the extrapolation of the strain data of the video extensometer against the distance between the crossheads.

3-3. Results and discussion

3-3-1. Preparation and characterization of the BC/PEA composites

Table 3-1. Compositions of the BC/H_2O and BC/EA gels

	Weight fraction (%) / Volume fraction (%)			
	BC[a]	H_2O	THF	EA
BC/H_2O gel	0.63/0.42	99.37/99.58	0	0
BC/EA gel	0.64/0.39	0.35/0.32	0.48/0.49	98.53/98.80

[a] Densities of BC,[17] THF, and EA were assumed to be 1.5, 0.89, and 0.92 g/cm^3, respectively.

Table 3-1 shows the composition of the BC/H_2O and BC/EA gels. The volume fractions of BC in the BC/H_2O and BC/EA gels were 0.42 and 0.39 vol%, respectively, indicating that little shrinkage of the BC gel occurred through the solvent exchange. The residual amounts of H_2O and THF were minimal in the BC/EA gel, which is indicative of successful solvent exchange. Subsequently, photo-initiated free radical polymerization of EA and EGDMA in the gel was conducted. The obtained BC/PEA composite was sufficiently transparent to show a light transmittance at 800 nm of

85% for the 2 mm thick sample. The monomer conversion was calculated to be over 95% from the weight before and after vacuum treatment. To analyze the molecular weight of the primary polymer chain of crosslinked PEA, EA was polymerized under the same conditions without EGDMA as a reference, and the produced "uncrosslinked" PEA was analyzed by GPC; M_n and M_w/M_n of the PEA were 2.5×10^6 and 3.11, respectively.

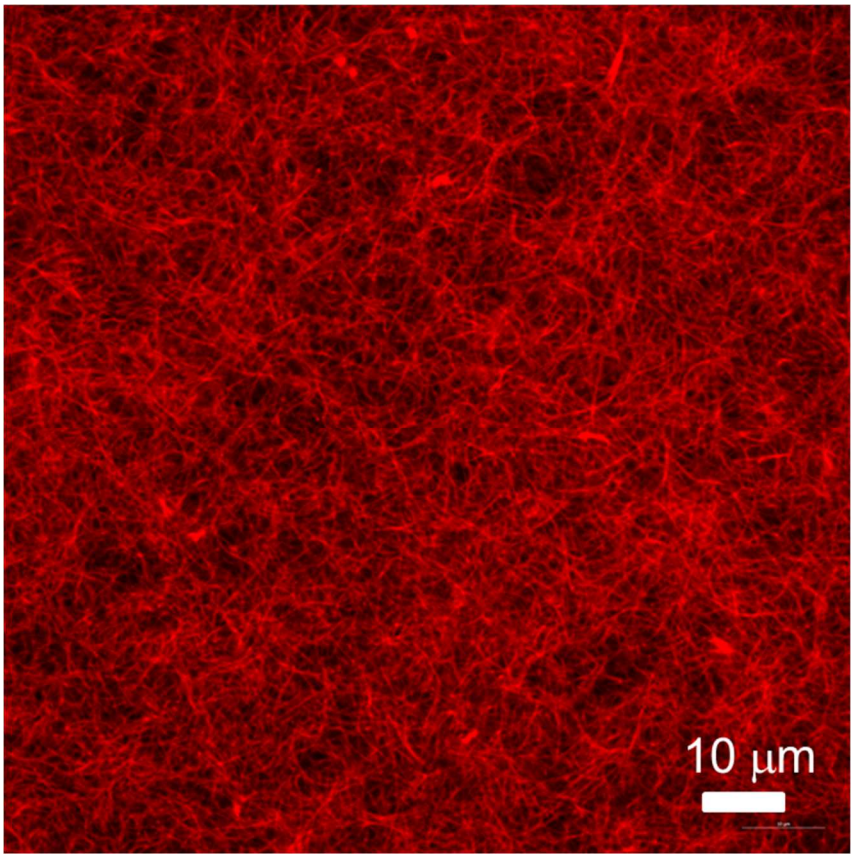

Figure 3-2. CLSM image of the BC/PEA composite in the in-plane direction.

To visualize the BC-network structure in the BC/PEA composite, a fluorescent-labeled BC/PEA composite was subjected to CLSM observation (Figure 3-2). In this image, the BC nanofiber is visible as the red color. It shows that the BC was distributed homogeneously and formed a network in the PEA matrix. The diameter of the BC nanofibers was approximately 200 nm, which was an

overestimate owing to the resolution limit set by the diffraction of light. The maximum distance between BC nanofibers in the BC/PEA composite was estimated as a few micrometers, similar to the original BC/H_2O.[4] Consequently, we concluded that minimal BC aggregation occurred during the solvent exchange and following polymerization, and the BC/PEA composite preserved the original CNF network.

3-3-2. Tensile properties of the BC/PEA composite

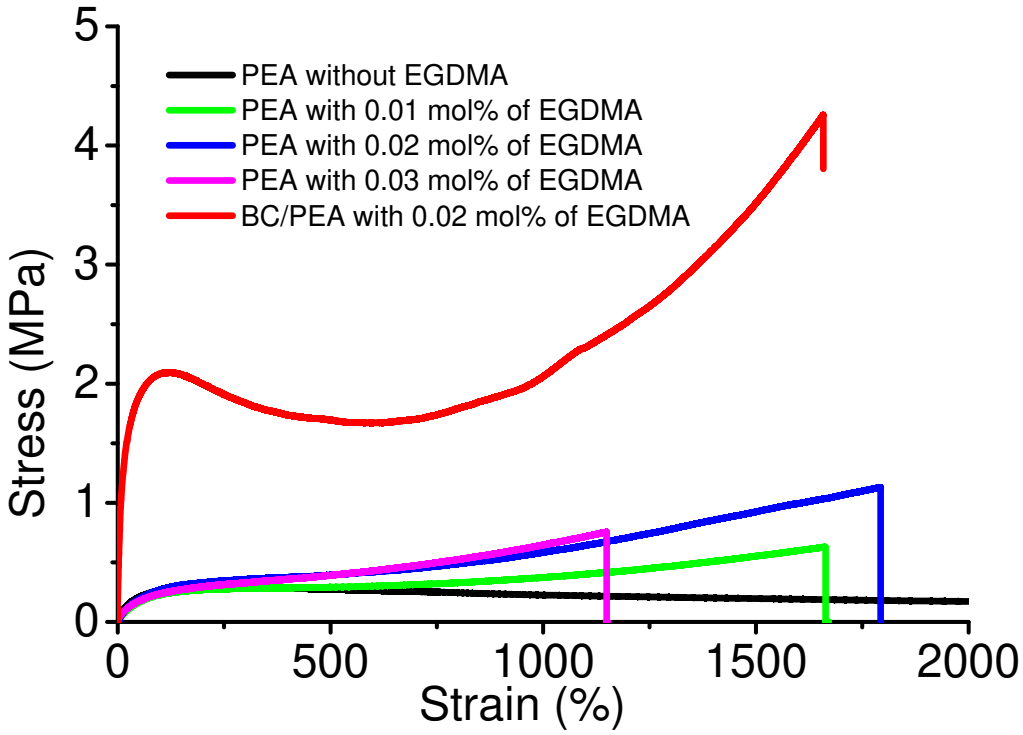

Figure 3-3. Stress-strain curves of the PEA and BC/PEA composites in the tensile tests.

Figure 3-3 shows typical stress-strain curves of the uncrosslinked and crosslinked PEAs as well as the BC/PEA composite. The tensile test of the BC/PEA composite was conducted in the in-plane direction of BC sheet. Uncrosslinked PEA (without EGDMA) yielded at 250% strain, and the stress decreased from the yielding point to over 2000% strain. On the contrary, the stress of crosslinked

PEAs with 0.01–0.03 mol% EGDMA increased via a plateau region after the yielding point. The sample with 0.03 mol% EGDMA gave an evidently lower fracture strain than the other two. Thus, we concluded that the EGDMA concentration suitable for preparing highly stretchable and sufficiently crosslinked elastomeric matrix was 0.02 mol%. The BC/PEA composite with 0.02 mol% of EGDMA yielded at 130% strain, slightly decreasing the stress, which continued its increase from about 540 to 1660% strain. High stress values at the yielding point and the following pseudo-plateau region suggest good reinforcement by the BC nanofibers.

Table 3-2. Mechanical properties of the BC/PEA composites and PEA with 0.02 mol% of EGDMA[a]

	Young's modulus E (MPa)	Strain hardening modulus E' (MPa)	Tensile strength σ (MPa)	True tensile strength σ' (MPa)	Fracture strain (%)	Fracture energy (MJ/m^3)
BC/PEA	15 ± 1	197 ± 41	3.5 ± 0.6	57 ± 13	1520 ± 110	32 ± 4
PEA	0.58 ± 0.19	35 ± 4	1.0 ± 0.1	17 ± 4	1660 ± 240	8.4 ± 2.0

[a] Average values and standard deviation of three samples were given.

Table 3-2 shows the mechanical properties of the BC/PEA composite and the PEA with 0.02 mol% of EGDMA. The strain-hardening modulus (E') and the true tensile strength (σ') were estimated from the slope of true stress-strain curve and the strength at the fracture strain. True stress σ_{true} and true strain ε_{true} were calculated as follows by assuming that the volume of composites was unchanged throughout tensile tests and cross-section area was uniform:

$$\sigma_{true} = \sigma_{exp}(1 + \varepsilon_{exp}) \qquad (3-1)$$

$$\varepsilon_{true} = \ln(1 + \varepsilon_{exp}) \qquad (3-2)$$

where σ_{exp} and ε_{exp} were experimentally obtained stress and strain, respectively. The mechanical properties of the composites were dramatically improved by introducing a BC network. It should be noted that despite such high reinforcement, the fracture strain of the BC/PEA composite was kept as high as 1520 %, similar to the crosslinked PEA without a BC network. The BC network increased the fracture energy of the composites by 3.8 times when compared to the crosslinked PEA without a BC network.

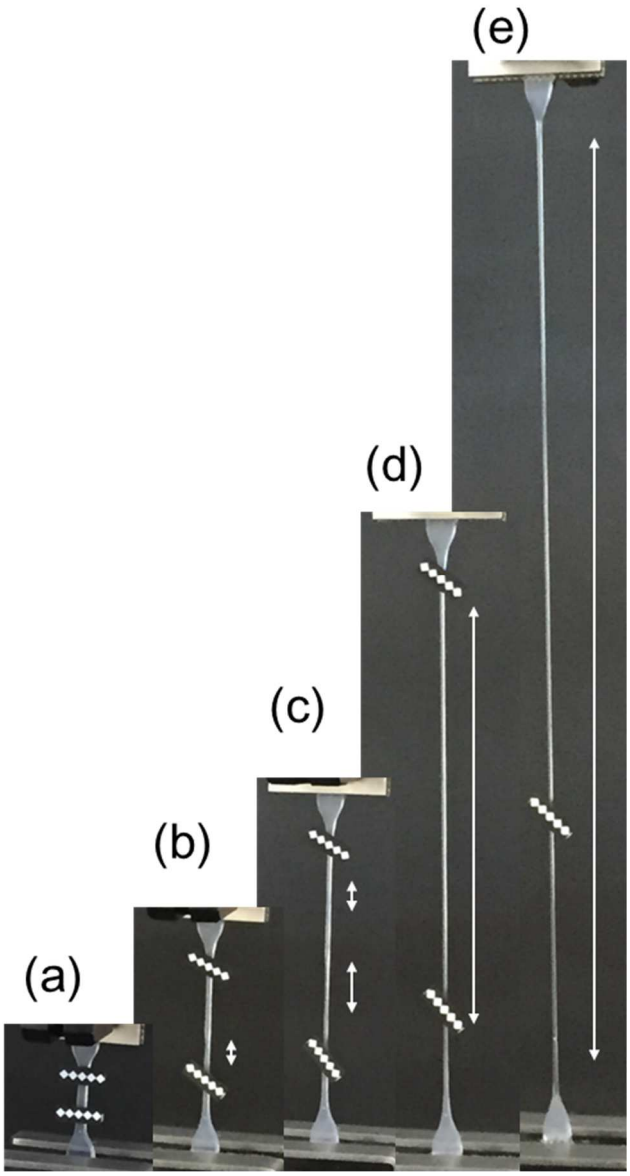

Figure 3-4. Images of the BC/PEA composite in the tensile tests. The strains were (a) 0%, (b) approx. 200%, (c) approx. 400%, (d) approx. 800%, and (e) approx. 1400%. White arrows indicate necking regions. The two pairs of the white diamond rows on the dumbbell specimen were markers for the non-contact video extensometer. In (e) at approx. 1400% strain, one marker dropped.

Figure 3-4 shows images of the BC/PEA dumbbell samples during a tensile test. Just after the yielding point at approximately a 200% strain, so-called necking was observed where the sample

specimen was locally stretched and tapered off, forming a neck. Upon further elongation, the necked region gradually expanded, finally permeating the whole specimen at approximately a 1400% strain. Such a necking phenomenon was not observed for the crosslinked PEA and can reasonably be ascribed to the effect of the BC network embedded in the matrix. Hajji et al. reported a similar necking phenomenon in styrene-butyl acrylate latex composites with 6 wt% cellulose whiskers and ascribed it to the network formation.[18] It should be noted that in this case, the filler concentration was much lower and the stress increased again after the yielding plateau. Especially, the second increase in stress contributed to the significant improvement of the above-mentioned tensile properties.

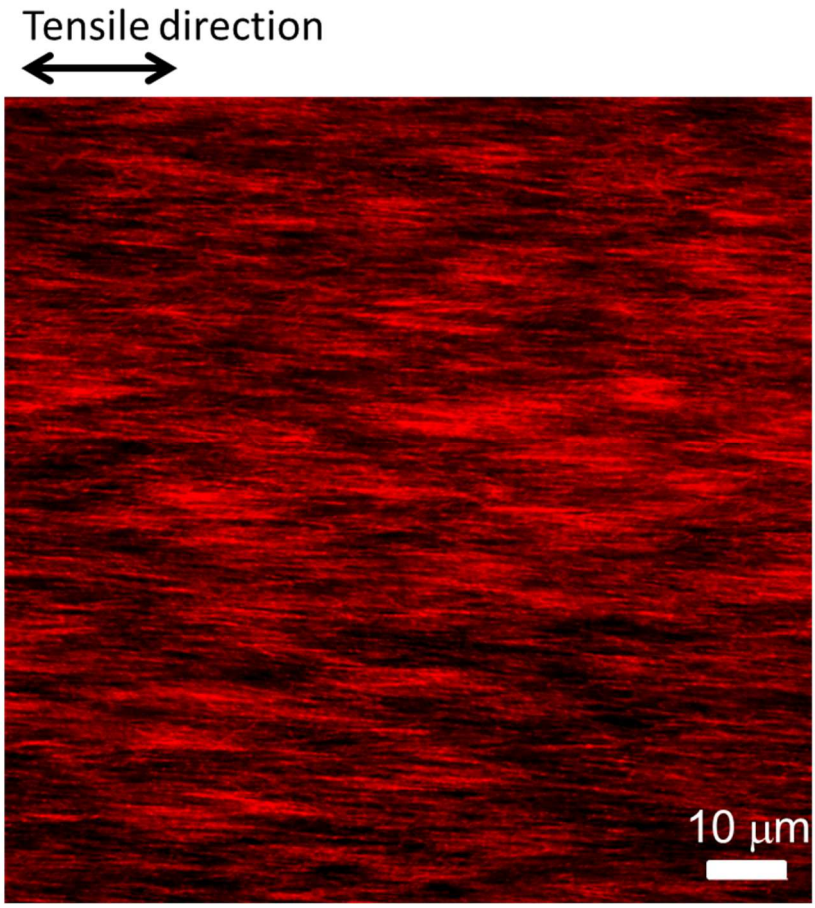

Figure 3-5. CLSM image of the necked region of a BC/PEA composite in the in-plane direction at approximately a 1000% strain.

Figure 3-5 shows a CLSM image of the necked region of the BC/PEA composite at approximately a 1000% strain. This image clearly suggests that almost all of the nanofibers were highly aligned parallel to the tensile direction. Thus, we reasonably ascribed the necking phenomenon to the strain-hardening induced by the uniaxial orientation of the BC nanofibers. The effect of strain hardening was quantitatively confirmed in Table 3-2. The strain-hardening modulus, i.e., the modulus just before the fracture, of the composite was approximately 6 times larger than that of the crosslinked PEA without a BC network and approximately 13 times larger than the Young's modulus, i.e., the modulus at the initial strain, of the composite. This strongly suggests that the high strain-hardening was caused predominantly by the BC network and not by the crosslinked PEA.

The elastic modulus (E) and tensile strength (σ) were theoretically estimated based on the rule of mixtures (Voigt model) by a factor of its volume fraction V_f to the mechanical properties of the composite.[19] The predicted values $E_{predicted}$ and $\sigma_{predicted}$ were calculated as follows:

$$E_{predicted} = E_f V_f + E_m(1 - V_f) \quad (3-3)$$

$$\sigma_{predicted} = \sigma_f V_f + \sigma_m(1 - V_f) \quad (3-4)$$

where the subscriptions, f and m, represent the filler (BC fiber) and the matrix (crosslinked PEA), respectively. For the calculation, we focused on the composite sample with highly oriented BC nanofibers around the fracture strain, similar to the experimental situation (as was observed in Figure 5). For this, E_f and σ_f was set to the literature data along the longitudinal direction of the BC nanofibers (E_f = 138 GPa, σ_f = 6 GPa), and E_m and σ_m were set to be the strain hardening modulus and the true tensile strength of the crosslinked PEA, respectively (see Table 3-2), experimentally determined at the fracture strain. Consequently, $E_{predicted}$ and $\sigma_{predicted}$ were calculated to be 552 MPa and 41 MPa, respectively. Even a simplified model could give good agreement between the experimental and predicted values for both the elastic modulus and tensile strength. This confirms

that almost all the BC fibers are highly oriented with minimal breaking and effectively contribute to the improvement of mechanical properties at the fracture strain (Figure 3-5). Here, it should be noted that the above-mentioned rule of mixtures usually assumes sufficiently strong interaction of the interface between the matrix and the filler. But, this may not be the present case; the interfacial interaction may be weak because of low affinity. Therefore, the present system must have the structure capable of independently transferring the stress between the fillers without via the matrix, suggesting a highly and macroscopically percolated structure of the fillers kept during the course of stretching.

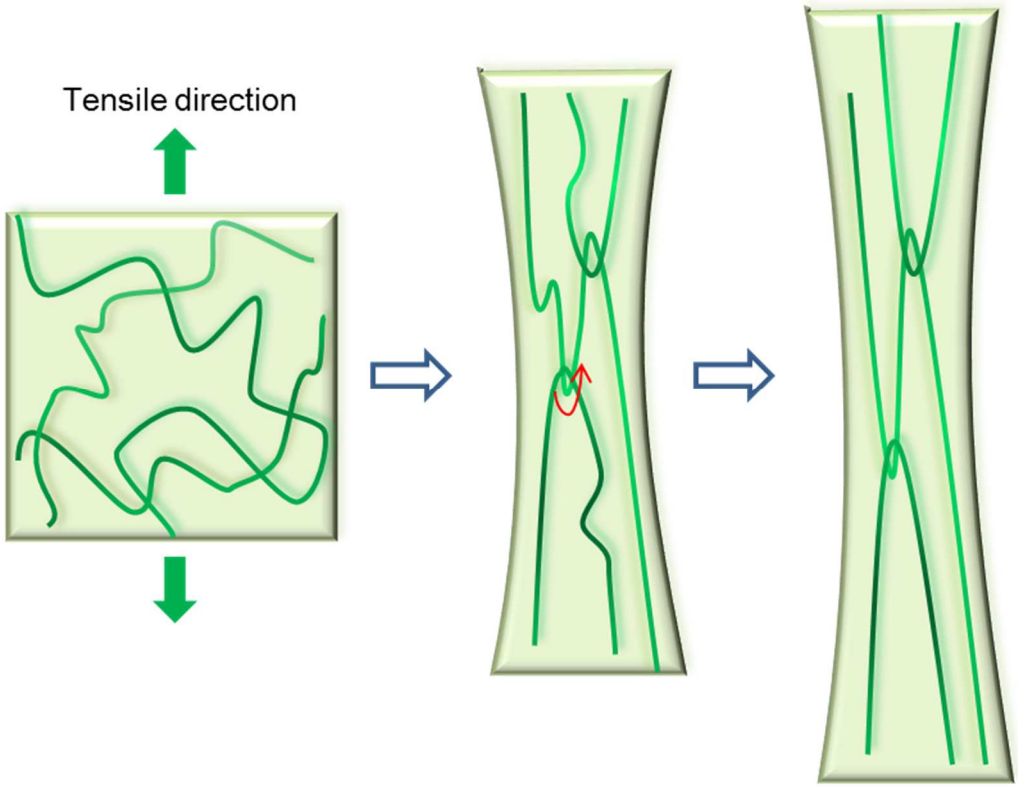

Figure 3-6. Schematic illustration of the proposed BC-reinforcement mechanism of the BC/PEA elastomer.

According to the above-mentioned experimental evidences and thereby deriving considerations, we

propose the following mechanism of the BC reinforcement as shown in Figure 3-6, in which the weak interaction between the BC fiber and the PEA matrix was assumed. As shown in Figure 3-2, the BC fibers are long enough to be regarded as entangled coils, forming a BC network and a gel not only in water but also in various matrices. Subsequently, interfacial slip due to low interfacial strength and high flexibility of the BC nanofiber enables easy deformation of the BC network, promoting the synchronized orientation of fibers. In this case, the entanglement points could slide in response to deformation, otherwise the segments of such long nanofibers with a large distribution in the contour length between the entanglement points could not be so highly aligned and effectively percolated without fracturing the BC network as shown in Figure 3-5. Previously, it was reported that the BC hydrogel was not so highly stretched.[20] This may be ascribed to microscopically heterogeneous and non-slippy aggregation or crosslinking, formed by pre-compressing (for increasing the BC content) or stretching the hydrogel, between the BC fibers. In the present system, the matrix was considered to suppress such aggregation or crosslinking even at large deformation by disturbing the contact with the fibers and also the crucial fracture of the composite by mitigating the local fracture energy of BC fibers, enabling the large deformation of the BC network without fracture. This is why the composite can be so effectively reinforced so as to be predicted by the rule of mixtures despite weak interfacial strength of the filler and the matrix.

3-4. Conclusions

BC-reinforced elastomers with a well-defined nanofiber network were prepared by "*in situ* solvent exchange and polymerization". The obtained elastomeric composite showed good mechanical properties even with a small volume fraction of BC. It was characterized by exceptionally high fracture strain, good stretchability, and effective strain hardening providing the necking phenomenon during the tensile test. The CLSM observations revealed successful embedding of a well-defined

nanofiber network of the original BC in the PEA matrix as well as uniform orientation of the BC nanofibers in the stretched sample. These remarkable mechanical and structural features could reasonably be ascribed to the rigidity and flexibility of the BC nanofibers and thereby produced a percolated structure of totally aligned nanofibers by elongation. This is likely due to the appropriate dispersion and entanglement of the native BC nanofibers produced by the bacterium. This process can be applied to various materials, revealing the reinforcement capability for composites with a BC nanofiber network.

3-5. References

1. I. Sakurada, Y. Nukushina, T. Ito. *J. Polym. Sci.* **1962**, *57*, 651–660.

2. T. Nishino, K. Takano, K. Nakamae, *J. Polym. Sci., Part B: Polym. Phys.* **1995**, *33*, 1647–1651.

3. T. Saito, R. Kuramae, J. Wohlert, L. A. Berglund, A. Isogai. *Biomacromolecules* **2012**, *14*, 248–253.

4. M. Iguchi, S. Yamanaka, A. Budhiono. *J. Mater. Sci.* **2000**, *35*, 261–270.

5. Y. Nishi, M. Uryu, S. Yamanaka, K. Watanabe, N. Kitamura, M. Iguchi, S. Mitsuhashi. *J. Mater. Sci.* **1990**, *25*, 2997–3001.

6. S. Yamanaka, K. Watanabe, N. Kitamura, M. Iguchi, S. Mitsuhashi, Y. Nishi, M. Uryu. *J. Mater. Sci.* **1989**, *24*, 3141–3145.

7. G. Guhados, W. Wan, J. L. Hutter. *Langmuir* **2005**, *21*, 6642–6646.

8. Y.-C. Hsieh, H.Yano, M. Nogi, S. Eichhorn. *Cellulose* **2008**, *15*, 507–513.

9. A. Nakagaito, S. Iwamoto, H. Yano. *Appl. Phys. A: Mater. Sci. Process.* **2005**, *80*, 93–97.

10. M. Nogi, H. Yano. *Adv. Mater.* **2008**, *20*, 1849–1852.

11. H. Yano, J. Sugiyama, A. Nakagaito, M. Nogi, T. Matsuura, M. Hikita, K. Handa. *Adv. Mater.* **2005**, *17*, 153–155.

12. Y. Shimizu, S. Akimoto, K. Sakakibara, Y. Tsujii, to be submitted.

13. V. Favier, H. Chanzy, J. Y. Cavaille. *Macromolecules* **1995**, *28*, 6365–6367.

14. N. E. Marcovich, M. L. Auad, N. E. Bellesi, S. R. Nutt, M. I. Aranguren. *J. Mater. Res.* **2006**, *21*, 870–881.

15. Q. Wu, M. Henriksson, X. Liu, L. A. Berglund. *Biomacromolecules* **2007**, *8*, 3687–3692.

16. A. Hirai, O. Inui, F. Horii, M. Tsuji. *Langmuir* **2009**, *25*, 497–502.

17. W. Gindl, J. Keckes. *Compos. Sci. Technol.,* **2004**, *64*, 2407–2413.

18. P. Hajji, J. Y. Cavaille, V. Favier, C. Gauthier, G. Vigier. *Polym. Compos.* **1996**, *17*, 612–619.

19. A. Kelly, W. R. Tyson. *J. Mech. Phys. Solids* **1965**, *13*, 329–350.

20. K. Uetani, T. Okada, H. T. Oyama. *ACS Macro Lett.* **2017**, *6*, 345-349.

Chapter 4

Fabrication, Structure and Tribological Property of Bottle-Brush Gel Matrix-based Nanocomposites

4-1. Introduction

A gel, in which a large amount of liquid was held within cross-linked fine networks, exhibited unique properties such as low friction, swelling and softness, therefore, had a potential for soft tribomaterials. However, the gel was mechanically weak and brittle due to containing of a large amount of liquid and cross-linking structure. To overcome this problem, many mechanically reinforced gels were reported including fiber-reinforced gels,[1] double network gels,[2] slide-ring gels[3] and tetra-PEG gels[4] and so on. Among them, fiber-reinforced gels were widely used not only as biological organizations such as plant cell wall and cartilage but also biomimetic applications such as cell scaffolds and artificial tissues.[5, 6] In addition, many of them were combined multiple different types of networks to achieve mechanical and functional improvement.

Bacterial cellulose (BC) gel, which was composed of CNF network, had desirable mechanical properties[7–10] such as high Young's modulus (114 GPa[11]) derived from high crystallinity. The most important characteristics of the BC gel was that highly fine and pure CNF network structure was maintained in water in spite it contains only less than 1% of BC because of the high aspect ratio and entanglement. Therefore, the BC gel was expected to be utilized as precursor material to prepare mechanically reinforced gels and composites for tissue engineering and other applications.[12, 13]

On the other hand, a gel exhibits specific frictional behaviors. In order to discuss them, repulsion-adsorption model was proposed from a viewpoint of interfacial interaction between polymer chains of a gel and a substrate.[14] In this model, the friction of a gel was determined by two

factors, elastic deformation of polymer chain derived from adsorption and lubrication of the hydrated layer of the polymer network. Therefore, frictional properties of a gel were depended on mechanical properties, interfacial interaction and viscosity of the hydrated layer.

Concentrated polymer brush (CPB) consisting of low-polydispersity polymers grown up from the substrates densely was highly extended in a good solvent, because of the exceptionally high osmotic pressure of the polymers.[15, 16] CPBs exhibit low friction coefficient because of less hindrance to the shear flow of fluid in the brush layer derived from high resistance of highly stretched structure against compression, and suppression of adsorption to opposite substrates.[17–21] CPBs were constructed on various kinds of shapes or materials including particles, fibers and bottle-brush polymers by using the surface-initiated living radical polymerization.[22–26] Among them, concentrated bottle-brush polymers, in which highly-branched macromolecules where polymers were grafted densely to a backbone polymer, had unique tribological properties depending on side chains.[27]

In Chapter 4, we focused on gels toward tribomaterials. BC nanofiber network was used for the supporting structure of the functional bottle-brush network. It was noted that this strategy was different from the double network gel in the point of that the two networks were divided to mechanical and frictional properties to improve both properties.[2] First of all, we described preparation of bottle-brush type hybrid gels reinforced with BC nanofiber network. They were expected to be shown high mechanical properties and low friction derived from i) combined networks of BC nanofiber and bottle-brush networks, ii) formation of hydrated layer and suppression of interfacial interaction based on osmotic pressure of CPBs. We prepared hybrid gels with concentrated polymer brush-grafted BC and bottle-brush networks by atom transfer radical polymerization (ATRP) of poly(ethylene glycol) methyl ether methacrylate (PEGMA) from initiator on surface of BC and macro-initiator network, yielding a PPEGMA-grafted BC/PBIEM gel. In the second, we investigated frictional behavior of the hybrid gels by using pin on disc type of

tribological measurements, and then discussed by using dynamic viscoelasticity measurements from a viewpoint of the elasticity and adhesion force of the gels. Thus we suggested the design for tribomaterials with significant mechanical and frictional properties.

4-2. Experimental Section

4-2-1. Materials

Bacterial cellulose (BC) hydrogel was purchased from Fujicco Co. Ltd. and purified according to procedures detailed in the literature.[28] 2-(2-bromo-2-methylpropanoyloxy)ethyl methacrylate (BIEM) (94%, Chemicrea Inc., Japan) was purified by passing through a column filled with activated basic alumina to remove the polymerization inhibitor. 2-bromoisobutyryl bromide (BiBB) (97%, Alfa Aesar), Ethyl 2-bromoisobutyrate (EBIB) (98 %, Tokyo Chemical Industry Co., Ltd.), Poly(ethylene glycol) methyl ether methacrylate (PEGMA) (M_n=475, Sigma-Aldrich), Poly(ethylene glycol) dimethacrylate (PEGDMA) (M_n=500, Sigma-Aldrich), 4,4'-dinonyl-2,2'-bipyridine (dNbipy) (>97 %, Wako Pure Chemical Industries, Ltd., Japan), copper(II) chloride ($CuCl_2$) (98%, Nacalai Tesque Inc., Japan), di-n-butyltin dilaurate (90 %, Wako), rhodamine B isothiocyanate (RITC) (mixed isomers, Sigma-Aldrich), anisole (99.9%, Wako), 1-Methyl-2-pyrrolidone (NMP) (99%, Wako), ammonia solution (28%, Nacalai) and 1-butyl-3-methylimidazolium trifluoromethanesulfonate (BMIM-Tf) (99%, IoLiTec Inc.) were used as received. Copper(I) chloride (CuCl) (99.9%,Wako) was washed with glacial acetic acid (99.7%, Wako) to remove any soluble oxidized impurities, filtered, washed with ethanol (99.5%, Wako) and diethyl ether (99.5%, Wako), and dried. 2,2'-Azobisisobutyronitrile (AIBN) (99%, Wako) was purified by recrystallization and used as an initiator for free radical polymerization. (2-Bromo-2-methyl) propionyloxypropyltriethoxysilane (BPE) was synthesized according to procedures detailed in the literature.[29] A silicon wafer (Ferrotec, Japan) was used as substrates for polymer brush surface. The

silicon wafer was cleaned by ultrasonication in order of acetone, chloroform and 2-propanol for 30 min, respectively, followed by treatment with ultraviolet (UV)/ozone for 30 min just before immobilization of ATRP initiator. PPEGMA was fabricated on the surface of the silicon wafer by surface-initiated ATRP.

4-2-2. Preparation of PPEGMA-grafted BC/PBIEM gel

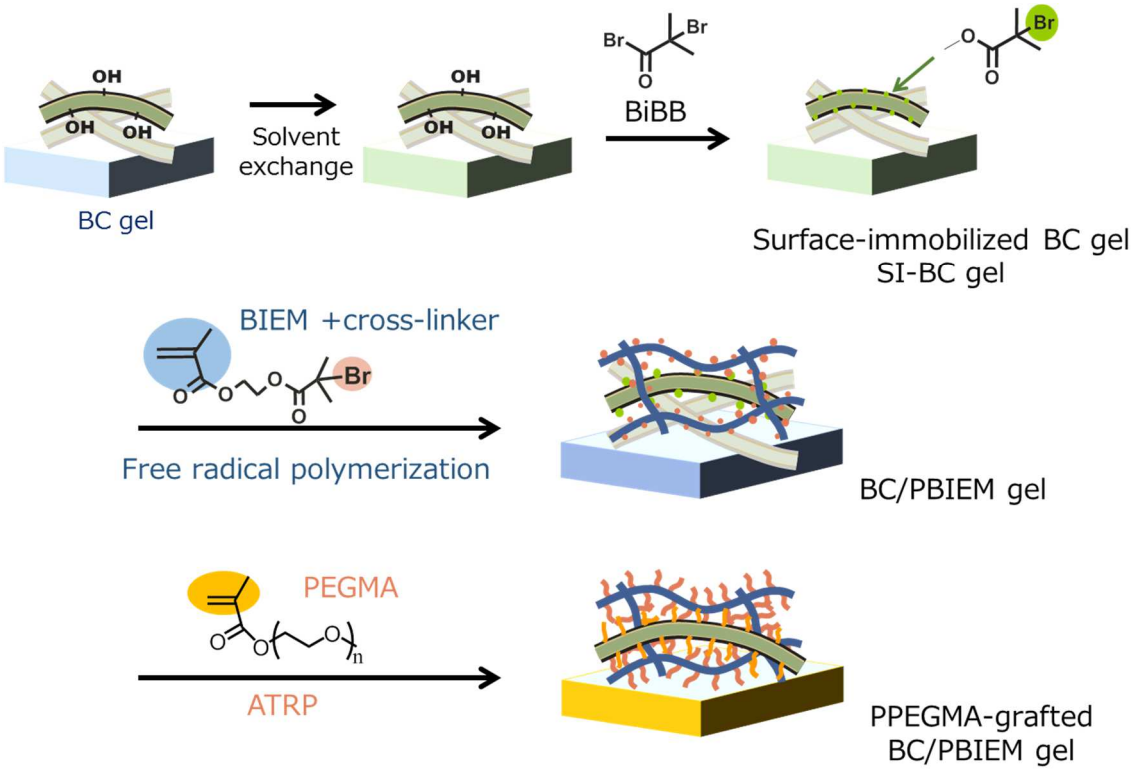

Figure 4-1. Schematic illustration for preparation of a PPEGMA-grafted BC/PBIEM gel.

Figure 4-1 shows a scheme for preparation of a PPEGMA-grafted BC gel, mainly containing three steps: introducing of (i) ATRP initiator on surface of a BC, yielding a surface-immobilized BC gel (SI-BC gel), (ii) ATRP macro-initiator network in the BC gel, yielding a BC/PBIEM gel and (iii) grafted PPEGMA on the surface of the BC and the macro-initiator network in the gel.

SI-BC gel

First, nine-fold amount of THF was added to the purified BC/H_2O gel and agitated for 12 h with a shaking apparatus (EYELA Multi Shaker MMS, Tokyo Rikakikai Co., Ltd., Japan). This treatment was carried out three times, then, any residual water was removed using a Soxhlet extractor with THF for 6 h, yielding a BC/THF gel. Next, NMP was added to the BC/THF gel and agitated in a same manner. This treatment was performed three times, yielding a BC/NMP gel. BiBB (2 eq/OH) was dropped into NMP solution of pyridine (4 eq/OH) and the BC/NMP gel in a three-necked flask cooled by an ice bath, then, the ice bath was removed and stirred at room temperature overnight. The BC gel was washed with methanol repeatedly to remove reaction residue and exchanged solvent to anisole, yielding a SI-BC gels. Density of initiator on the surface of BC was estimated from weight fraction of bromine by elemental analysis. Cross-section of BC was assumed 50 × 7.5 nm. Degree of substitution was 0.12 and density of initiator on the surface of BC was 2.2 unit/nm^2, which was large enough to be introduced concentrated polymer brushes.

BC/PBIEM gel 1 (for PPEGMA-grafted BC/PBIEM gel 1 and gel 4)

A SI-BC gel and anisole solution (70 wt%) of BIEM (1.08 M), PEGDMA (5.4 mM) and AIBN (0.54 mM) were put into a Schlenk flask with a three-way cock and purged argon gas. The flask was placed at 0 °C overnight in order to immerse the reaction mixtures into the gel uniformly. The gel was compressed and placed on a glass plate equipped with 2 mm thick polytetrafluoroethylene spacers, then, another glass plate was placed on the gel. The sample was clamped with double clips, then put into a polyethylene-coated aluminum pack, followed by filling with reaction mixture and argon gas, then, sealed. The sample was put into an oil bath and heated at 60 °C for 48 h. After polymerization, the gel was washed with anisole repeatedly, yielding a BC/PBIEM gel 1. Bromine content of the gel dried under vacuum was 24.55%.

BC/PBIEM gel 2 (for PPEGMA-grafted BC/PBIEM gel 2)

A SI-BC gel was compressed by using spacers with 0.5 mm in thickness, otherwise the same described as above, yielding a BC/PBIEM gel 2.

BC/PBIEM gel 3 (for PPEGMA-grafted BC/PBIEM gel 3)

A SI-BC gel and anisole solution (75 wt%) of BIEM (0.72 M), PEGDMA (3.6 mM) and AIBN (0.36 mM) were treated and the SI-BC gel was compressed by using spacers with 0.5 mm in thickness, otherwise the same described as above, yielding a BC/PBIEM gel 3.

PPEGMA-grafted BC/PBIEM gel 1

An argon purged anisole solution of PEGMA (0.47 M), CuCl (11.8 mM). $CuCl_2$ (2.4 mM), and dNbipy (28 mM) was put into an argon purged anisole solution (75 wt%) of EBIB (2.4 mM), a BC/PBIEM gel 1 (Initiator, 49 mM) and a SI-BC gel (Initiator 0.83 mM) in a Schlenk flask equipped with a three-way cock. The reaction mixtures were placed at 0 °C overnight in order to immerse the anisole solution into the gels uniformly. Then, the flask was heated at 60 °C for 2 h. The gels were washed with anisole repeatedly to remove reaction mixtures, yielding a PPEGMA-grafted BC/PBIEM gel 1 and a PPEGMA-grafted BC gel 1. The reaction mixture was diluted with DMF and analyzed by gel permeation chromatographic equipped with a multiangle laser light-scattering detector (GPC-MALLS). Weight of gels was measured. Weight fraction of the gels were estimated from dry weight measurement, and weight fractions of BC, PBIEM main chain and PPEGMA graft chain of BC and PBIEM were estimated from weight of SI-BC gel, BC/PBIEM gel and PPEGMA-grafted BC/PBIEM gel and each of dried residue.

PPEGMA-grafted BC/PBIEM gel 2

BC/PBIEM gel 2 (Initiator, 43 mM) and a SI-BC gel (Initiator 0.56 mM) in reaction mixtures as above were treated in a same manner, yielding a PPEGMA-grafted BC/PBIEM gel 2 and a PPEGMA-grafted BC gel 2.

PPEGMA-grafted BC/PBIEM gel 3 and 4

An argon purged anisole solution of PEGMA (0.46 M), CuCl (11.5 mM). $CuCl_2$ (2.3 mM), and dNbipy (28 mM) was put into an argon purged anisole solution (75 wt%) of EBIB (2.3 mM), a BC/PBIEM gel 3 and 1 (Initiator, 72 mM) and a SI-BC gel (Initiator 0.34 mM) were treated in a same manner, otherwise the flask was heated at 60 °C for 3 h, yielding a PPEGMA-grafted BC/PBIEM gel 3, 4 and a PPEGMA-grafted BC gel 3.

Fluorescent labelled PPEGMA-grafted BC/PBIEM gel

SI-BC/NMP gels (46.73 g, Degree of substitution was 0.10), RITC (45.5 mg), a catalytic amount of di-*n*-butyltin dilaurate and NMP (350 mL) were mixed and heated for 48 h at 100 °C. Then, the SI-BC gel was washed repeatedly with methanol to remove unreacted RITC and exchanged solvent to anisole, yielding fluorescent labelled SI-BC gels with 0.048 degree of substitution. The SI-BC gel and anisole solution (70 wt%) of BIEM (1.07 M), PEGDMA (5.4 mM) and AIBN (0.54 mM) were treated, otherwise the same described as above, yielding a fluorescent labelled BC/PBIEM gel. An argon purged anisole solution of PEGMA (0.49 M), CuCl (12.1 mM). $CuCl_2$ (2.4 mM), and dNbipy (29 mM) was put into an argon purged anisole solution (75 wt%) of EBIB (2.4 mM), the fluorescent labelled BC/PBIEM gel (Initiator, 39 mM) and a SI-BC gel (Initiator, 0.30 mM) in a Schlenk flask equipped with a three-way cock. otherwise the same described as above, yielding a fluorescent labelled PPEGMA-grafted BC/PBIEM gel.

Swelling of the PPEGMA-grafted BC/PBIEM gels in water and ionic liquid

A PPEGMA-grafted BC/PBIEM gel with mixture of ATRP solution was put into anisole, and agitated for 24 h with a shaking apparatus. This treatment was carried out more than three times. Next, THF, water and BMIM-Tf were added in order in a same manner, yielding a PPEGMA-grafted BC/PBIEM gel swelled in water or BMIM-Tf.

Cleavage of the grafted PPEGMA from the gel[30]

A freeze dried PPEGMA-grafted BC/PBIEM gel 1 (0.07 g) was immersed in THF (2 mL) under

argon atmosphere, and sodium methoxide (0.77 g, 20 wt% solution in methanol) was added. The mixture was heated at 50 °C for 16 h and washed by saturated aqueous NH_4Cl (3 mL) and brine (3 mL). Aqueous phase was extracted by ethyl acetate (6 mL) and the organic phase was dried over $MgSO_4$. The solvent was removed under reduced pressure, and the residue was dissolved in DMF and analyzed by GPC-MALLS.

4-2-3. Preparation of PPEGMA polymer brush on a silicon wafer

A silicon wafer was immersed in an ethanol solution of BPE (1 wt%) and 28% aqueous NH_3 (10 wt%) for 12 h at room temperature to immobilize initiating groups, then, washed with ethanol. A BPE-immobilized silicon wafer was immersed in an argon purged anisole solution of PEGMA (0.52 M), CuCl (5.3 mM), dNbipy (11.1 mM) and EBiB (0.27 mM). The mixture was heated at 60 ℃ for 24 h. After the polymerization, the silicon wafer was washed with methanol. The solution was diluted with DMF and analyzed by GPC-MALLS. The thickness of PPEGMA brushes on the silicon wafer was determined by a spectroscopic ellipsometer (M-2000U, J. A. Woolam, Lincoln, NE). Thickness of PPEGMA film was 49 nm. The graft density on a Si wafer was 0.13 chains/nm^2 and the surface coverage of grafted polymers on Si wafer was 36% calculated from cross-section area of PPEGMA (A_{PEGMA}=2.74 nm^2).

4-2-4. Characterization

To determine the number-average molecular weight (M_n), weight-average molecular weight (M_w), and polydispersity index (M_w/M_n), GPC analysis was carried out with a Shodex GPC-101 high speed liquid chromatography system equipped with a guard column (Shodex GPC KF-G), two 30-cm mixed columns (Shodex GPC LF-804, exclusion limit = 2×10^6), and a differential refractometer (Shodex RI-101). THF was used as an eluent at a flow rate of 0.8 mL/min. The GPC system was

calibrated by poly (methyl methacrylate) (PMMA) standards (Polymer Laboratories, M_p = 1.31 × 10^3–1.64 × 10^6), and M_n and M_w/M_n were calculated as PMMA-calibrated values. Sample detection was also made with MALLS detector (Wyatt Technology DAWN HELEOS, Santa Barbara, CA), equipped with a Ga-As laser (λ = 658 nm). The refractive index increments (d_n/d_c) of PPEGMA was determined to be 0.0470 mL g^{-1} using a Wyatt Technology Optilab rEX differential refractometer (λ = 658 nm). Confocal laser scanning microscopic (CLSM) observation was carried out by an inverted-type microscope (LSM 5 PASCAL, Carl Zeiss, Germany) with a 532-nm wavelength laser and ×63 objective lens (Plan Apochromat, Carl Zeiss) in reflection mode. The contrast and brightness of the CLSM images were adjusted by common software. The thickness of the brush layer in the dry state was determined using a compensator-rotating, spectroscopic ellipsometer (M-2000U TM, J. A. Woolam, NE) equipped with a D2 and QTH lamps. The polarizer angle was 45, and the incident angle was 70.

4-2-5. Measurements

Friction force and friction coefficient

Friction force (F_s) and friction coefficient (μ) were measured by pin on disc type of rotatory tribometer (UMT, Bruker Co., United States). A gel was sliced to 1 mm thick by a microtome blade and cut to a disk-shape of 6 mm in radius by using commercially available laser cutter. The gel was bonded on a metal pin by an adhesive agent of cyanoacrylate and set in a holder equipped with a spring sensor and a dumper. A glass disk or silicon wafer grafted PPEGMA was set on the rotatory disk. The metal pin with the gel was set on the location with a distance of 5 mm from the center of the rotary disk. The loading force (F) was 4, 10, and 30 N, and the number of rotation was from 500 to 0.1 rpm in stepwise, corresponding to 260–0.5 mm/s of sliding velocity. The rotary direction was switched clockwise to counter clockwise at each rotatory velocity. F_s was defined as an average of

detected absolute value in clockwise and counterclockwise rotation. The μ was defined as F_s /F. Water and BMIM-Tf were used as lubricants, and gels and PPEGMA on Si wafer were swelled by the lubricant in advance. Vertical displacement of a gel was measured by a laser sensor (LK-G-5000V, KEYENCE).

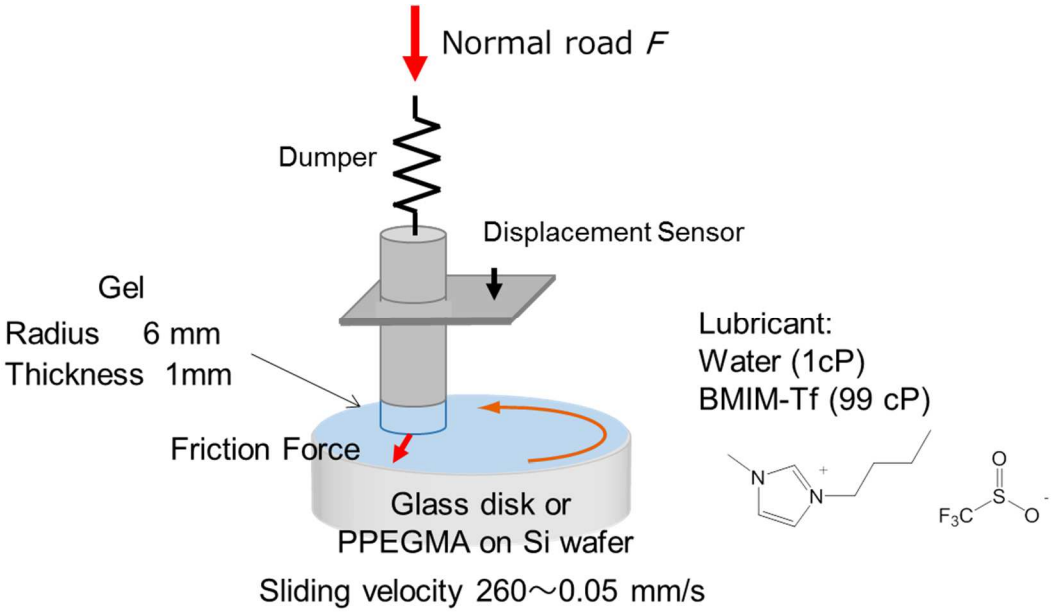

Figure 4-2. Schematic illustrated set up for friction measurements.

Force curve

A gel (Radius of the gel: ϕ = 6 mm, thickness: 1 mm) bonded on a metal pin was compressed at a speed of 40 N/min by the tribometer. Compressed displacement of the gel was measured by a laser sensor.

Rheometer measurements

Dynamic oscillatory was conducted by using a rheometer (ARES-G2, TA Instruments) equipped with a stainless plate (ϕ = 4 mm) and a gel immersed in BMIM-Tf (ϕ = 6 mm) bonded on a glass plate at room temperature (approx. 25 °C). The shear storage modulus G' and the shear loss modulus G'' were measured at strain amplitude of 5×10^{-4} in the angular frequency range of 0.1–300 rad/s.

Stress growth measurement was performed in shear rate range of 0.01–10 s^{-1} in clockwise and counterclockwise rotation at 0.10–0.21 of compression strain. Measurements were conducted after mitigation with constant strain compression.

4-3. Results and discussion

4-3-1. Preparation of PPEGMA-grafted BC/PBIEM gels

We applied "*in situ* stepwise solvent exchanges and polymerization" described in previous chapters for the preparation of a PPEGMA-grafted BC/PBIEM gel. First of all, in order to visualize a BC network, a fluorescent-labelled BC/PBIEM gel and a PPEGMA-grafted BC/PBIEM gel were prepared and subjected to CLSM observation (Figure 4-3). The BC was distributed homogeneously and observable maximum distance between BC was estimated as a few micro meters, similar to the original BC gel. Consequently, we concluded that successful fabrication of hybrid gels embedded with BC nanofiber network without aggregation of BC was attained by this approach despite additional multiple steps of solvent exchanges and polymerization process were included.

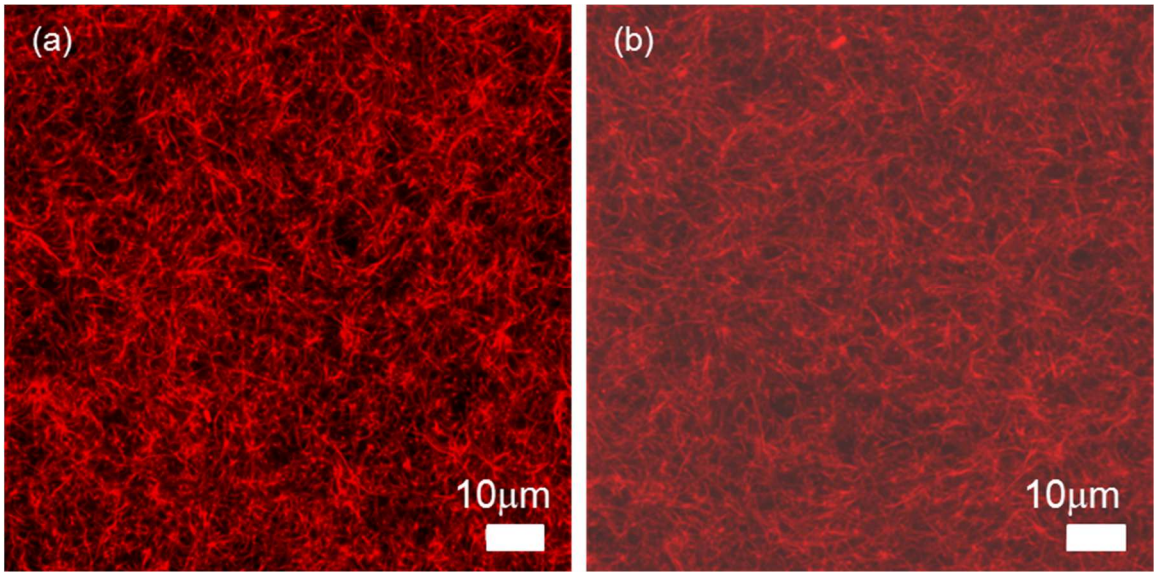

Figure 4-3. CLSM image of a (a) BC/PBIEM gel and (b) a PPEGMA-grafted BC/PBIEM gel.

Table 4-1. Compositions of BC/PBIEM gels.

	Weight fraction (wt %)		
	SI-BC	PBIEM	Anisole
BC/PBIEM gel 1	0.84	7.8	91.4
BC/PBIEM gel 2	2.6	15.5	81.9
BC/PBIEM gel 3	2.5	7.6	89.9

Subsequently, several kinds of BC/PBIEM gels were prepared, which were precursor for PPEGMA-grafted BC/PBIEM gels. Table 4-1 shows composition of BC/PBIEM gels. The reaction mixture was gel-like after polymerization, indicating cross-linked polymerization was proceeded. The gel-like reaction mixture was removed, then the BC/PBIEM gel was washed by anisole repeatedly to remove the monomer and uncross-linked polymers. The gel was rather swelled during solvent exchange from reaction mixture to anisole. The content of bromine was 24.55% for the BC/PBIEM gel 1 by an elemental analysis, indicating ATRP initiator was introduced in the BC/PBIEM gel with less elimination of bromine during polymerization and purification.

Table 4-2. Compositions of a PPEGMA-grafted BC gel 1 and PPEGMA-grafted BC/PBIEM gels swelled in water (upper) and BMIM-Tf (lower).

	Weight fraction (%)				M_n	Outer
	SI-BC	PBIEM	PPEGMA	Water BMIM-Tf	$\times 10^3$	surface coverage
PPEGMA-grafted	0.63		0.22	99.2		
BC gel 1	-		-	-		
PPEGMA-grafted	0.52	4.8	19.3	75.4	3.2	27%
BC/PBIEM gel 1	0.41	3.8	15.3	80.5		
PPEGMA-grafted	1.14	6.9	25.0	67.0	3.6	20%
BC/PBIEM gel 2	0.92	5.6	20.2	73.3		
PPEGMA-grafted	1.19	3.6	16.7	78.5	5.4	12%
BC/PBIEM gel 3	0.95	2.9	13.3	82.9		
PPEGMA-grafted	0.58	5.4	19.9	74.1	5.4	10%
BC/PBIEM gel 4	0.43	4.0	14.8	80.8		

Subsequently, PPEGMA-grafted BC gels were prepared by using the BC/PBIEM gels. Table 4-2 shows compositions of a PPEGMA-grafted BC gel and PPEGMA-grafted BC/PBIEM gels swelled in water and BMIM-Tf. The weight fraction of water was smaller than BMIM-Tf at each gel, mainly due to the difference of the density of water and BMIM-Tf.

Free initiator was also added in the reaction mixture as indicator of the M_n and M_w/M_n of grafted polymers. However, in this case, concentration of initiator in a gel was much larger than that outside

of the gel because macro-initiator was only in the gels. That might cause different characterization between the free polymer and the grafted polymer, otherwise concentration of the monomer was maintained uniform, that is, diffusion rate of the monomer was faster enough than the consume rate of the monomer. Therefore, rate of polymerization was controlled slowly by adding Cu(II) catalyst. In addition, in order to characterize grafted polymers, cleavage of grafted polymers by transesterification of the PPEGMA-grafted BC/PBIEM gel was performed. Collection ratio of the cleaved polymer was approximately 20%, considering that the grafted polymer could be characterized by the cleaved polymers. Figure 4-4 shows GPC profiles. A peak of the cleaved polymer was spread to lower molecular weight regime compared to that of free polymer because of some PEG side chains of the cleaved polymer were cleaved. Accordingly, the M_n of grafted PPEGMA in the gel was considered almost same as that of the free polymer.

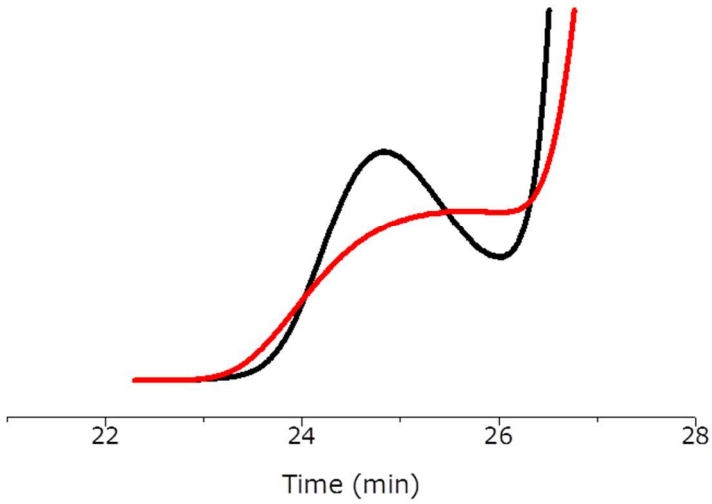

Figure 4-4. GPC profiles of free polymer (black) and cleaved polymer (red) of PPEGMA-grafted BC/PBIEM gel 1

Subsequently, A SI-BC gel was also added into the reaction mixture for the purpose of characterizing the polymer grafted from surface of a BC because of the difficulty of characterizing of

grafted polymers on the BC in the PPEGMA-grafted BC/PBIEM gel, which was much less than the grafted polymers derived from bottle-brush network. The graft density on BC was 0.32 chains/nm^2, which was calculated from the weight ratio of PPEGMA chains and BC for the PPEGMA-grafted BC gel. The surface coverage of grafted polymers on BC was 89% calculated from cross-section area of PPEGMA, which was larger than expected, probably because of spread of cross-sectional corner space of BC and extension of PEG side chains to the direction of main chains. In conclusion, concentrated polymer brush was performed with high graft density on BC.

Subsequently, outer surface coverage (σ^*) of bottle-brush network was calculated by using cylinder model of bottle-brush, that is, expressed by

$$\sigma^* = \frac{r_{main\ chain}}{r_{bottle-brush,extended}} \times \sigma^*_{main\ chain} \qquad (4-1)$$

where, $r_{main\ chain}$ and $r_{bottle\text{-}brush,\ extended}$ were cross-sectional radius of PBIEM main chain and bottle-brush graft chains were extended. $\sigma^*_{main\ chain}$ was surface coverage on main chains. They were given by

$$r_{bottle-brush,extended} = L \times \frac{M_{n,side\ chain}}{M_{n,PEGMA}} + r_{main\ chain} \qquad (4-2)$$

$$\sigma^*_{main\ chain} = \frac{(W_{side\ chain}/W_{main\ chain})}{\left(M_{n,side\ chain}/M_{n,BIEM}\right)} \times \frac{A_{PEGMA}}{S_{BIEM}} \qquad (4-3)$$

$$S_{BIEM} = 2\pi\, L\, r_{main\ chain} \qquad (4-4)$$

where, A_{PEGMA}, S_{BIEM} were cross-section area of PEGMA and surface area of BIEM, respectively. $M_{n,\ side\ chain}$, $M_{n,\ BIEM}$ were molecular weight of PPEGMA grafted chains and BIEM, respectively. $W_{side\ chain}$ and $W_{main\ chain}$ were weight of PPEGMA grafted chains and main chains, respectively. L was unit length of polymer chains (L = 0.25 nm). By using parameters of cross-section area of PEGMA (A_{PEGMA} = 2.74 nm^2) and cross-sectional radius of PBIEM ($r_{main\ chain}$ = 0.6 nm), the outer surface coverages of bottle-brush networks were calculated as Table 4-2, indicating bottle-brush with concentrated polymer brush on surface was prepared. In conclusion, concentrated bottle-brush type

hybrid gels reinforced with BC network was fabricated in success.

4-3-2. Frictional properties of PPEGMA-grafted BC/PBIEM gels

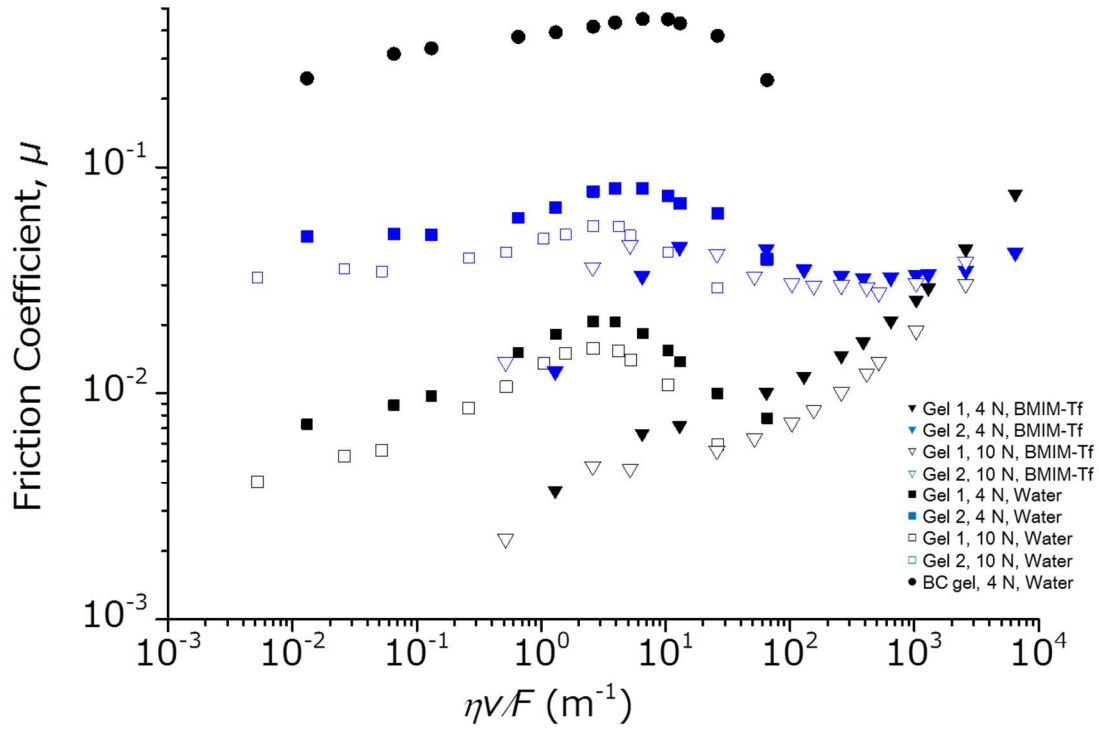

Figure 4-5. Plots of friction coefficient μ against characteristic parameter $\eta v/F$ for a BC gel (closed circle) and PPEGMA-grafted BC/PBIEM gels 1, 2 versus a glass disk in BMIM-Tf (triangle) and water (circle and square) at 4 N (closed symbol) and 10 N (open symbol).

The μ of gels were measured by a pin on disk type of tribometer. Water and BMIM-Tf were selected as lubricants because of good solvent for PPEGMA and high viscosity (99 cP at 25 °C), which enabled swelling the gels and measuring wide range of $\eta v/F$. The parameters η, v, and F were viscosity, sliding velocity and normal load, respectively. Figure 4-5 shows plots of the μ against $\eta v/F$, i. e. Stribeck curve of PPEGMA-grafted BC/PBIEM gels and a BC gel versus a glass

disk in BMIM-Tf and water. In Figure 4-5, first of all, the μ for the PPEGMA-grafted BC/PBIEM gel 1 was attained as low as 10^{-3}, which was more than one order of magnitude smaller than those of a BC gel (10^{-1}) and the double network gel composed of poly(2-acrylamido-2-methylpropane sulfonic acid) and poly(acrylamide) (10^{-1}–10^{-2}),[31] indicating adhesion force was extremely suppressed by introduction of the bottle-brush network. It was noted that thus hybrid gels were exhibited low μ without electrostatic repulsive interaction unlike the double network gel. Subsequently, frictional behavior including the appearance of peaks for water and shoulders for BMIM-Tf was different depending on kinds of gels and lubricants, indicating characteristic of the gels including the lubricants was affected.

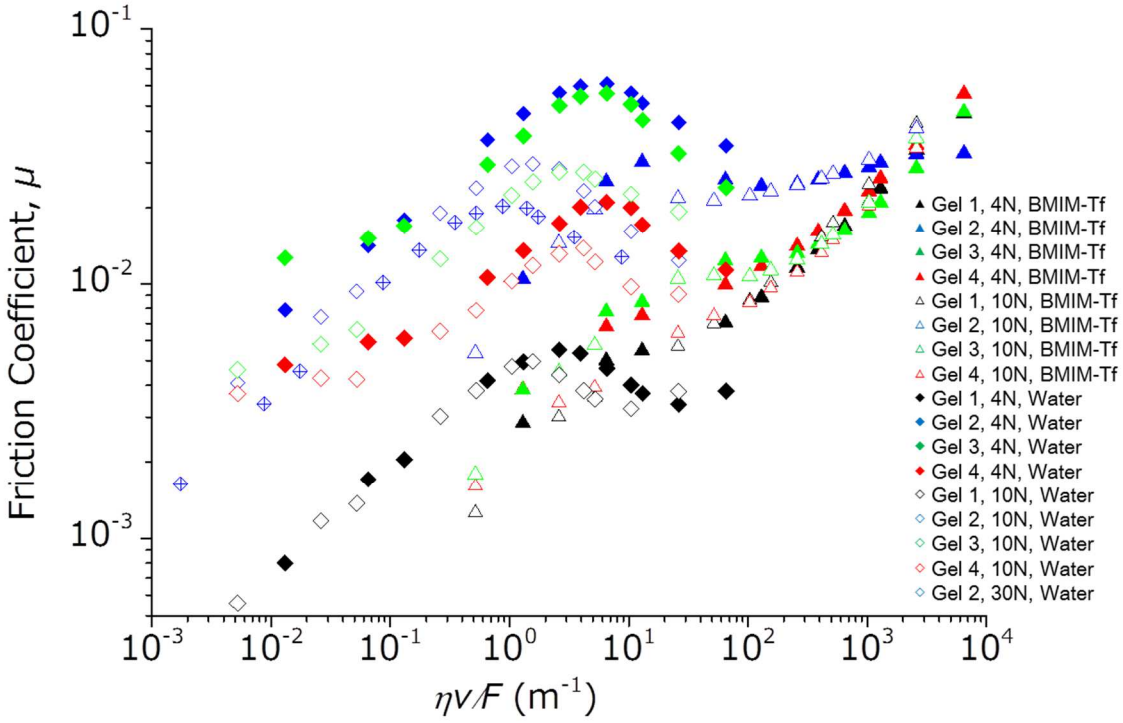

Figure 4-6. Plots of friction coefficient μ against characteristic parameter $\eta v/F$ for PPEGMA-grafted BC/PBIEM gels 1–4 versus PPEGMA-grafted Si wafer in BMIM-Tf (triangle) and water (diamond) at 4 N (closed symbol), 10 N (open symbol) and 30 N (diamond with cross).

Figure 4-6 shows Stribeck curve for PPEGMA-grafted BC/PBIEM gels versus CPB in BMIM-Tf and water. Frictional behavior in the regime of large $\eta v/F$ was almost similar among the gels, indicating less influencing the properties of the gels due to the hydrodynamic lubrication. Shoulders for BMIM-Tf and peaks for water were also appeared, while the μ in these regimes was smaller than that versus a glass disk in Figure 4-5. In addition, with the decrease of sliding speeds, μ decreased to be attained in 10^{-4} order of the μ for the PPEGMA-grafted BC/PBIEM gel 1, indicating adhesion force was extremely suppressed by immobilized lubrication film derived from osmotic pressure of opposite CPB. It was noted that the thin CPB had superior wear resiliency against friction of the gels, suggesting the combination of the soft hybrid gels and the CPB layer were suitable for the design of tribomaterials.

4-3-3. Dynamic viscoelasticity of gels

Here, we discuss the dynamic viscoelasticity in order to understand sliding and deformation behavior of the gels, and the origin of the shoulder in the Stribeck curve for the PPEGMA-grafted BC/PBIEM gels with BMIM-Tf.

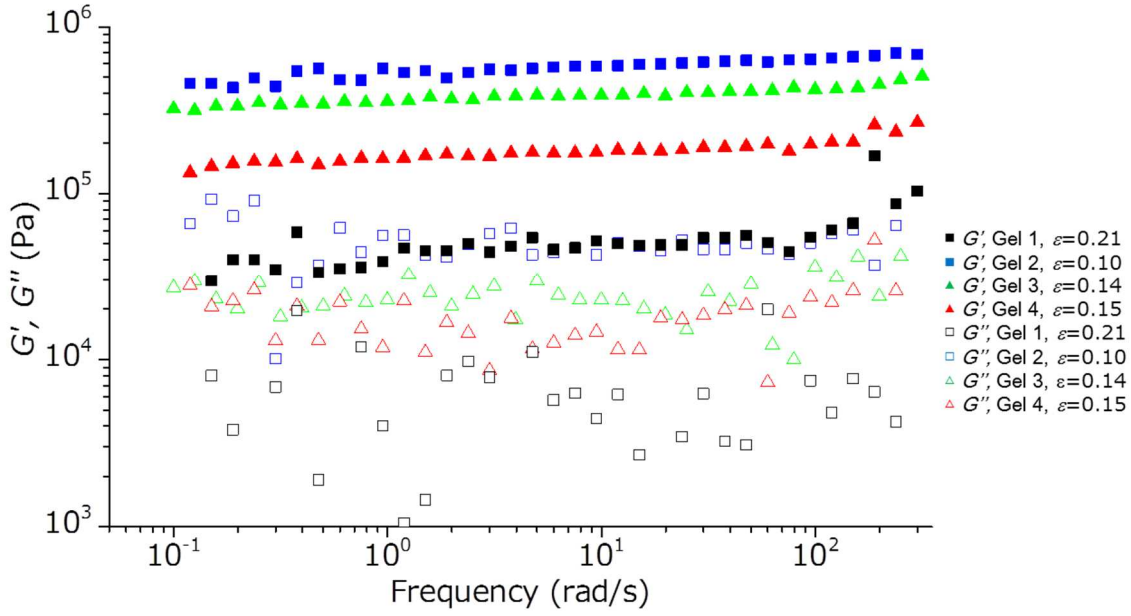

Figure 4-7. Shear storage modulus *G'* (closed symbols) and shear loss modulus *G"* (open symbols) for PPEGMA-grafted BC/PBIEM gels 1–4 immersed with BMIM-Tf at oscillation frequency range of 0.1–300 rad/s at strain amplitude of 5×10^{-4}. Compressive strain (ε) of the gels was 0.10–0.21.

First of all, Figure 4-7 shows the shear storage modulus *G'* and the shear loss modulus *G"* for PPEGMA-grafted BC/PBIEM gels with BMIM-Tf at strain amplitude of 5×10^{-4}. For these gels, the *G'* was larger than *G"*, indicating they had gel-like behavior. The extrapolated *G'* of the gels 1–4 at 0.1 rad/s were 34, 453, 326 and 144 kPa, respectively, which were much higher than a BC hydrogel and PBIEM gels, roughly similar to that of the double network gel (10^5 Pa).[31] In addition, the *G'* was mainly depended on the fraction of BC network (See Table 4-2), concluding reinforcement of bottle-brush with only small amount of BC nanofiber network was achieved in success.

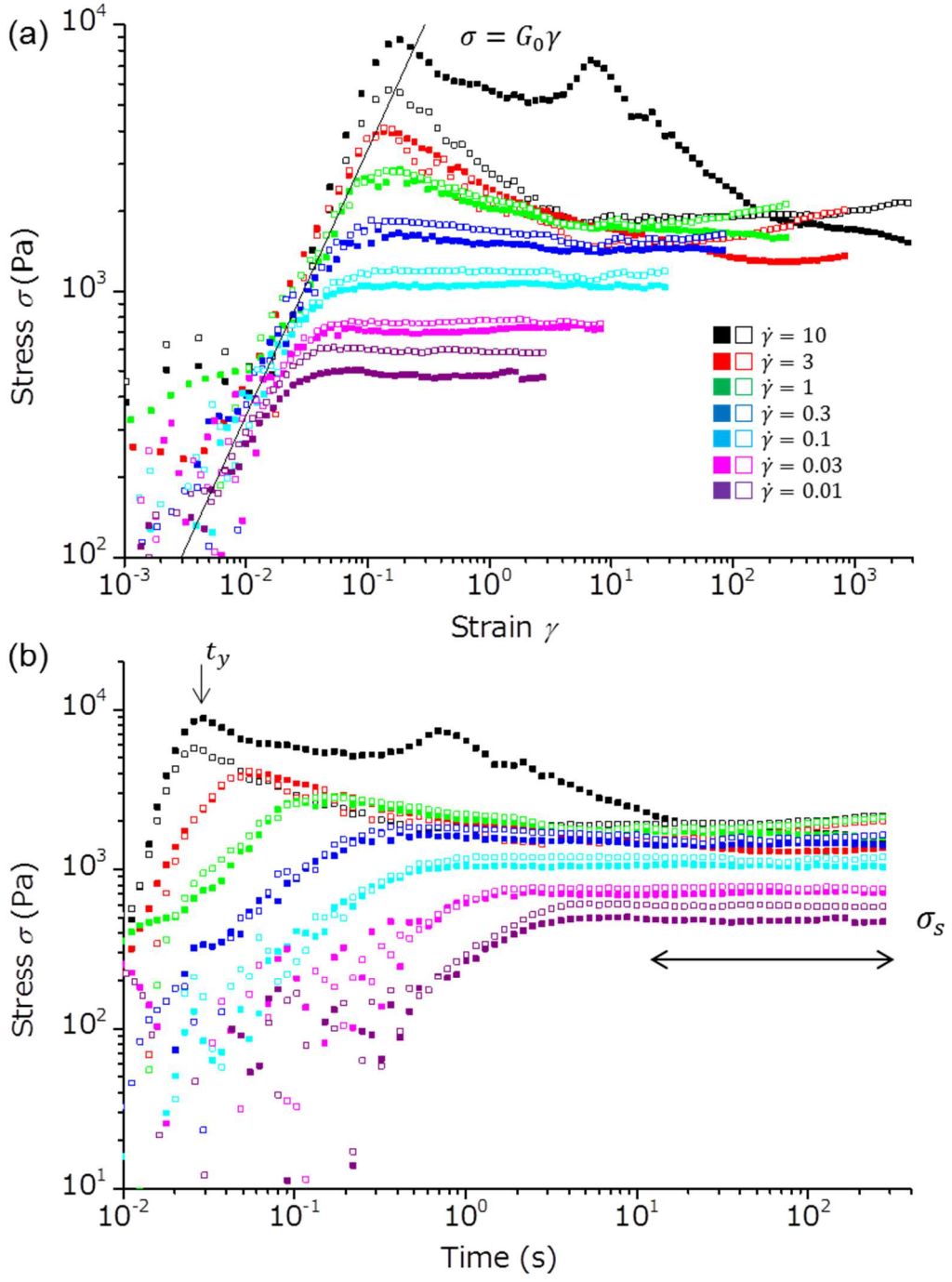

Figure 4-8. Stress growth behavior for PPEGMA-grafted BC/PBIEM gel 1 immersed with BMIM-Tf at shear rate of 10–0.01 s^{-1} versus (a) strain and (b) time. Closed and open symbols show clockwise and counter-clockwise of rotation, respectively. The line shows $\sigma = G_0\gamma$ with 34 kPa of G_0.

Figure 4-8 shows stress growth behavior of PPEGMA-grafted BC/PBIEM gel 1 with BMIM-Tf at the shear rate ($\dot{\gamma}$) of 10–0.01 s^{-1}. Here, we discussed three types of regimes; i) start-up state in which stress (σ) increased, ii) transition state around yielding points of the σ, and iii) steady-state of the σ after yielding.

In the regime of start-up state, the σ increased linearly against the γ with a slope of 1 derived from elastic deformation of the gel (Figure 4-8(a)). The line $\sigma = G_0\gamma$ with G_0 =34 kPa which was the G' at 0.1 rad/s was overlapped with the plots, appropriating that the elastic modulus (G_0) was assumed the G' at 0.1 rad/s in Figure 4-7.

In the regime of transition state around yielding points, stress overshoot phenomenon was observed and after yielding, the σ decreased toward steady-state at larger shear rate, whereas was not observed at smaller shear rate. Yielding time t_y was much smaller than time scale of plateau region of the G' in Figure 4-7, indicating slipping of the gels were started around yielding points without internal fracture, otherwise, the σ was unstable due to fracture of gels.

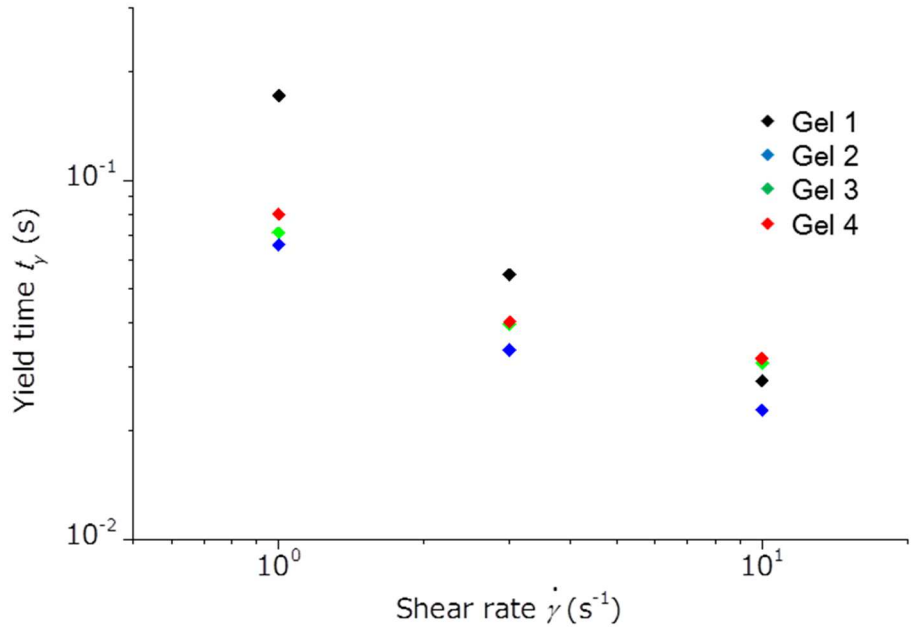

Figure 4-9. Yield time t_y for PPEGMA-grafted BC/PBIEM gels 1–4 immersed with BMIM-Tf in

the shear rate range of 10–1 s^{-1}.

Figure 4-9 shows yield time t_y for the PPEGMA-grafted BC/PBIEM gels 1–4 against the shear rate, at which overshoot phenomenon was appeared in Figure 4-8(b). With increase of shear rate, t_y decreased to converge, suggesting characteristic time for desorption of the gels, which would be caused occurrence of starting up friction force.

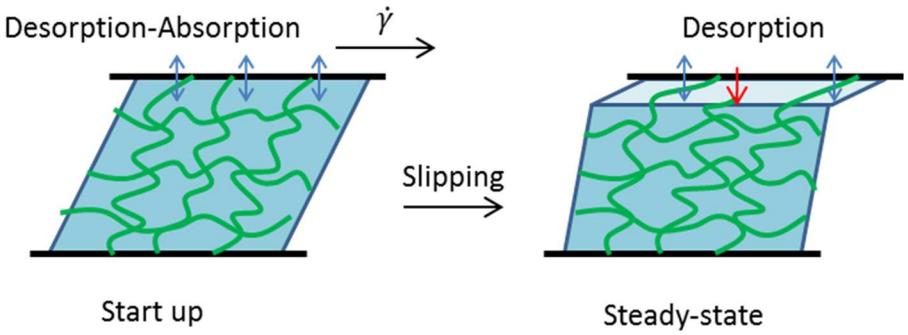

Figure 4-10. Illustration of transition from start-up-state to steady-state for the gel.

Figure 4-10 shows illustration of transition from start-up-state to steady-state for the gel. The gel was uniformly deformed due to absorption with desorption-absorption lifetime of polymer chains to a substrate at start-up. After desorption of the chains with restoration of the gel was occurred, a part of chains was no longer absorbed probably because of the insertion of fluid films and fluid flow and sliding of interface.

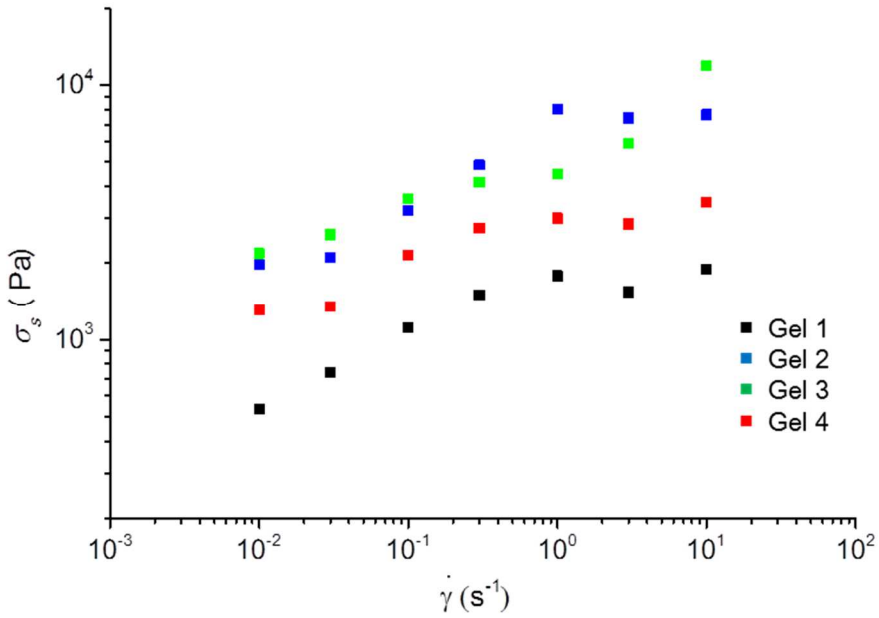

Figure 4-11. Steady-state stress σ_s for PPEGMA-grafted BC/PBIEM gels 1–4 immersed with BMIM-Tf at shear rate of 10–0.01 s^{-1}.

Subsequently, we discuss the regime of steady-state. Figure 4-11 shows the average stress of 10–300 s, which was defined as the stress of steady-state (σ_s), for the PPEGMA-grafted BC/PBIEM gels 1–4 with BMIM-Tf. The σ_s linearly increased with the increase of $\dot{\gamma}$ and was become almost constant in larger $\dot{\gamma}$ for all gels. Since the normal stress was assumed roughly constant at each gel during the stress growth measurements, it was considered that the shoulders in Figure 4-11 were also corresponded to those of the gels with BMIM-Tf in Figure 4-5. Here, the σ_s was defined as below,

$$\sigma_s = G_{eff}\gamma_{eff} \qquad (4-5)$$

where, G_{eff} and γ_{eff} were the effective elastic modulus and strain, respectively. In this case, the G_{eff} was assumed G_o because sliding behavior were occurred only on the surface of the gels without internal fracture. Accordingly, the σ_s was shown as below,

$$\sigma_s = G_0\gamma_{eff} \qquad (4-6)$$

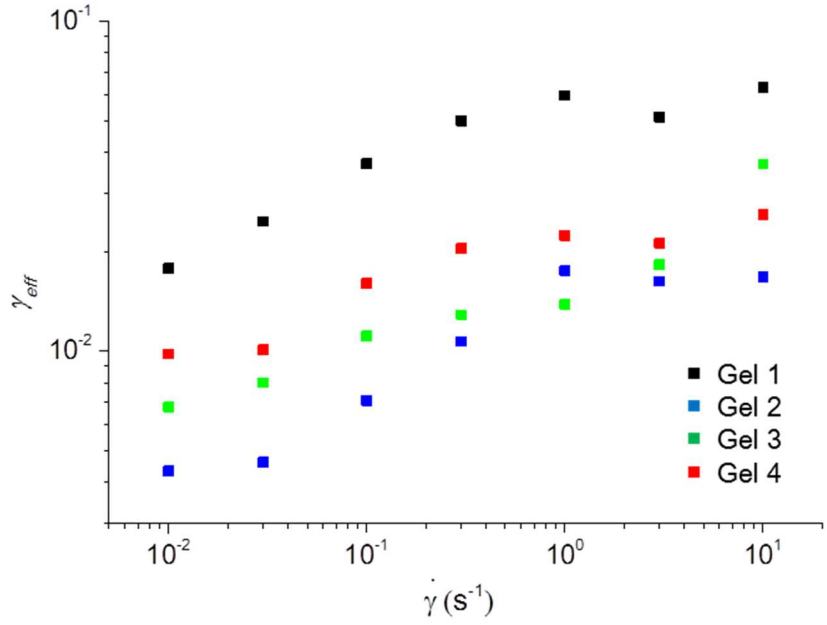

Figure 4-12. The γ_{eff} for PPEGMA-grafted BC/PBIEM gels 1–4 immersed with BMIM-Tf at shear rate of 10–0.01 s^{-1}.

Figure 4-12 shows the γ_{eff} for PPEGMA-grafted BC/PBIEM gel 1–4 with BMIM-Tf. The γ_{eff} linearly increased with the $\dot{\gamma}$ because the increase of $\dot{\gamma}$ was predominant over decrease of adsorption lifetime of polymer chains, while the γ_{eff} was become constant at larger $\dot{\gamma}$ because gels were desorbed at the strain that stretching force of polymer chains was reached to adhesion force within lifetime of adsorption. In conclusion, σ_s in the shoulder region of Stribeck curve was derived from adhesion force and elastic modulus of the gels.

Finally, we discussed the difference of frictional force between the PPEGMA-grafted BC/PBIEM gel 1 with extremely low σ_s and the PPEGMA-grafted BC/PBIEM gel 2 and 3 with large σ_s in Figure 4-11. The σ_s was expressed by the parameter of G_0 and γ_{eff} in eq. 4-6. While the hybrid gels showed negative correlation between G_0 and γ_{eff} (See Figure 4-7 and 4-12), the σ_s showed positive and negative correlation against G_0 and γ_{eff}, respectively, indicating σ_s was mainly depended to G_0. On the other hand, the difference of σ_s between the gel 2 and 3 was small,

indicating the surface coverage was less affected probably because that of the gels were large enough.

4-4. Conclusion

We demonstrated preparation of hybrid gels with concentrated polymer brush-grafted BC nanofiber and bottle-brush networks by "*in situ* stepwise solvent exchanges and polymerization" and surface-initiated ATRP of PEGMA. The moduli of the hybrid gels were much higher than a BC hydrogel and a PBIEM gel depending on BC contents, concluding remarkable reinforcement of bottle-brush was achieved by embedded with small amount of BC nanofiber fine network in success. Friction coefficient of thus obtained hybrid gels was attained to an order of 10^{-4} in magnitude, suggesting that adhesion force was effectively suppressed by bottle-brush network and immobilized lubrication film derived from the CPB. In addition, the hybrid gels had superior wear resiliency against the thin CPB on the rigid substrate, suggesting the potential toward tribomaterials. The rheometer measurements suggested friction force at the shoulder region of Stribeck curve was derived from adhesion force and the elastic modulus of the gel. From these results, we revealed the general approach toward tribomaterials by dividing two networks to mechanically reinforced network and low frictional network with small adhesion force.

4-5. References

1. A. Nakayama, A. Kakugo, J. P. Gong, Y. Osada, M. Takai, T. Erata, S. Kawano. *Adv. Funct. Mater.* **2004**, *14*, 1124–1128.
2. J. P. Gong, Y. Katsuyama, T. Kurokawa, Y. Osada. *Adv. Mater*. **2003**, *15*, 1155–1158.
3. Y. Okumura, K. Ito. *Adv. Mater.* **2001**, *13*, 485–487.
4. T. Sakai, T. Matsunaga, Y. Yamamoto, C. Ito, R. Yoshida, S. Suzuki, N. Sasaki, M. Shibayama,

U.-I. Chung. *Macromolecules* **2008**, *41*, 5379–5384.

5. A. C. Jen, M. C. Wake, A. G. Mikos. *Biotechnol. Bioeng.* **1996**, *50*, 357–364.
6. J. K. F. Suh, H. W. Matthew. *Biomaterials* **2000**, *21*, 2589–2598.
7. M. Iguchi, S. Yamanaka, A. Budhiono. *J. Mater. Sci.* **2000**, *35*, 261–270.
8. Y. Nishi, M. Uryu, S. Yamanaka, K. Watanabe, N. Kitamura, M. Iguchi, S. Mitsuhashi. *J. Mater. Sci.* **1990**, *25*, 2997–3001.
9. S. Yamanaka, K. Watanabe, N. Kitamura, M. Iguchi, S. Mitsuhashi, Y. Nishi, M. Uryu. *J. Mater. Sci.* **1989**, *24*, 3141–3145.
10. G. Guhados, W. Wan, J. L. Hutter. *Langmuir* **2005**, *21*, 6642–6646.
11. Y. -C. Hsieh, H. Yano, M. Nogi, S. Eichhorn. *Cellulose* **2008**, *15*, 507–513.
12. A. Nakayama, A. Kakugo, J. P. Gong, Y. Osada, M. Takai, T. Erata, S. Kawano. *Adv. Funct. Mater.* **2004**, *14*, 1124–1128.
13. A. Svensson, E. Nicklasson, T. Harrah, B. Panilaitis, D. L. Kaplan, M. Brittberg, P. Gatenholm. *Biomaterials* **2005**, *26*, 419–431.
14. J. P. Gong, Y. Osada. *J. Chem. Phys.* **1998**, *109*, 8062–8068.
15. M. Ejaz, S. Yamamoto, K. Ohno, Y. Tsujii, T. Fukuda. *Macromolecules* **1998**, *31*, 5934–5936.
16. S. Yamamoto, M. Ejaz, Y. Tsujii, M. Matsumoto, T. Fukuda. *Macromolecules* **2000**, *33*, 5602–5607.
17. S. Yamamoto, M. Ejaz, Y. Tsujii, T. Fukuda. *Macromolecules* **2000**, *33*, 5608–5612.
18. Y. Tsujii, K. Ohno, S. Yamamoto, A. Goto, T. Fukuda. *Adv. Polym. Sci.* **2006**, *197*, 1–45.
19. Y. Tsujii, A. Nomura, K. Okayasu, W. Gao, K. Ohno, T. Fukuda. *J. Phys.: Conf. Ser.* **2009**, *184*, 012031.
20. A. Nomura, K. Okayasu, K. Ohno, T. Fukuda, Y. Tsujii. *Macromolecules* **2011**, *44*, 5013–5019.
21. A. Nomura, K. Ohno, T. Fukuda, T. Sato, Y. Tsujii. *Polym. Chem.* **2012**, *3*, 148–153.

22. K. Ohno, T. Morinaga, S. Takeno, Y. Tsujii, T. Fukuda. *Macromolecules* **2006**, *39*, 1245–1249.

23. R. Barbey, L. Lavanant, D. Paripovic, N. Schüwer, C. Sugnaux, S. Tugulu, H. A. Klok. *Chem. Rev.* **2009**, *109*, 5437–5527.

24. K. L. Beers, S. G. Gaynor, K. Matyjaszewski, S. S. Sheiko, M. Möller. *Macromolecules* **1998**, *31*, 9413–9415.

25. K. Yamada, M. Miyazaki, K. Ohno, T. Fukuda, M. Minoda. *Macromolecules* **1999**, *32*, 290–293.

26. P. S. Lacerda, A. M. Barros-Timmons, C. S. Freire, A. J. Silvestre, C. P. Neto. *Biomacromolecules* **2013**, *14*, 2063–2073.

27. X. Banquy, J. Burdyńska, D. W. Lee, K. Matyjaszewski, J. Israelachvili. *J. Am. Chem. Soc.* **2014,** *136*, 6199–6202.

28. A. Hirai, O. Inui, F. Horii, M. Tsuji. *Langmuir* **2009**, *25*, 497–502.

29. K. Ohno, T. Morinaga, K. Koh, Y. Tsujii, T. Fukuda. *Macromolecules* **2005**, *38*, 2137–2142.

30. S. Yamago, Y. Yahata, K. Nakanishi, S. Konishi, E. Kayahara, A. Nomura, A. Goto, Y. Tsujii. *Macromolecules* **2013**, *46*, 6777–6785.

31. D. Kaneko, T. Tada, T. Kurokawa, J. P. Gong, Y. Osada. *Adv. Mater*. **2005**, *17*, 535–538.

Chapter 5

Functionality of Bacterial Cellulose Nanofiber Network Embedded in Matrices

5-1. Introduction

Network structure, which consisted of struts, joints and spaces, was mechanically characterized by the deformation behaviors of the struts including stretching and bending. The modulus of the network was proportional to the density with scaling exponents depended on the deformation behaviors.[1–3] Mechanical properties of composites were also discussed by the deformation behavior of network structure in matrices.[4, 5]

We successfully prepared ideal composites such as resins, elastomers and gels, which were reinforced with well-defined fine BC nanofiber network structure by "*in situ* stepwise solvent exchanges and polymerization". This method was expandable for various matrix including small affinity with BC nanofiber because interfacial tension was controlled by using solvent with intermedial affinity between BC and a monomer, and demonstrated superior mechanical and tribological properties derived from BC nanofiber networks in Chapters 2-4.

In this chapter, we discussed mechanical properties of the composites and deformation behavior of the BC nanofiber network in matrices with various viscoelasticity by using the composites prepared in previous chapters.

5-2. Experimental Section

5-2-1. Materials

Bacterial cellulose (BC) hydrogel was purchased from Fujicco Co. Ltd. and purified according to

procedures detailed in the literature.[6] Poly(methyl methacrylate) (PMMA), BC/PMMA composites, crosslinked poly(ethyl acrylate) (PEA) elastomer, BC/PEA elastomer and PPEGMA-grafted BC/PBIEM gels prepared in Chapters 2, 3 and 4 were used.

5-2-2. Estimation of modulus

The modulus of PMMA and BC/PMMA composites was adapted the averaged indentation modulus at 7000-8000 nm contact depth by nano-indentation analysis in Chapter 2. The modulus of PEA and BC/PEA elastomer was adapted Young's modulus by tensile tests in Chapter 3. Compressed BC/PEA elastomer was prepared for the method in Chapter 3, yielding *c*-BC/PEA elastomer with 1.4 vol% of BC and 46 MPa of Young's modulus. The modulus of PPEGMA-grafted BC/PBIEM gels was adapted averaged shear storage modulus $\overline{G'}$ over oscillation frequency range of 0.1–200 rad/s in Chapter 4. The modulus of a BC hydrogel was estimated from gradients of tangent at stress-strain curve of its compression measurement with disk-shape of 4.2 mm in radius and 1.8 mm in thickness at a speed of 0.01 mm/s. Surface area of a BC hydrogel was observed during compression, assumed constant due to exuding water. Volume fraction of BC was estimated from compression strain. The modulus of BC network $(E_{BC\ network})$ was estimated from the network model in Chapter 2, that is, described as follow based on the rule of mixtures.

$$E_{BC\ network} = E_c - E_m(1 - V_{\mathrm{BC}}) \qquad (5-1)$$

where, E_c was the modulus of a composite and V_{BC} was the volume fraction of the BC network. The moduli of liquid and bottle-brush network were ignored.

5-3. Results and Discussion

5-3-1. Modulus of BC nanofiber network embedded in matrices

At summary of Part 1, we systematically discussed the elasticity of BC nanofiber network

embedded in matrices with various viscoelasticity. We assumed that the BC network was periodically entangled with high connectivity but not connectivity was depended on the volume fraction, because the BC network was homogenously and continuously entangled at only 0.3 vol% of BC by CLSM. It has been reported that the relative modulus of network with similar geometry was scaled as $E \sim \rho^n$, in general, where, E and ρ are the relative modulus and density of a network, respectively.[1, 2] Scaling exponent n close to 1 indicates stretch-dominated deformation behavior of the network, whereas exponent n close to 2 indicates bend-dominated deformation. Exponent n larger than 2 indicates some parts in the network are inefficient for load transfer due to inhomogeneity of the network such as defects, entanglement, loop, or dangling of chains. We adapted this model in thus obtained composites.

Figure 5-1 shows double logarithmic plots of modulus of BC network for nanocomposites with well-defined BC nanofiber prepared in Part 1 and a BC hydrogel. In Figure 5-1, the $E_{BC\ network}$ increased linearly with the increase of the volume fraction of BC for every kind of composites and BC hydrogel (only two plots for BC/PEA elastomer). In addition, the $E_{BC\ network}$ was dependent on matrices, indicating matrices were affected the modulus of BC network. The modulus of BC bulk ($E_{BC\ bulk}$) predicted from the extrapolation of linear fitting was shown in Table 5-1. The thus assumed $E_{BC\ bulk}$ was roughly consistent with $E_{BC\ bulk}$ theoretically estimated (23 GPa) (see equation (2-3) in Chapter 2).

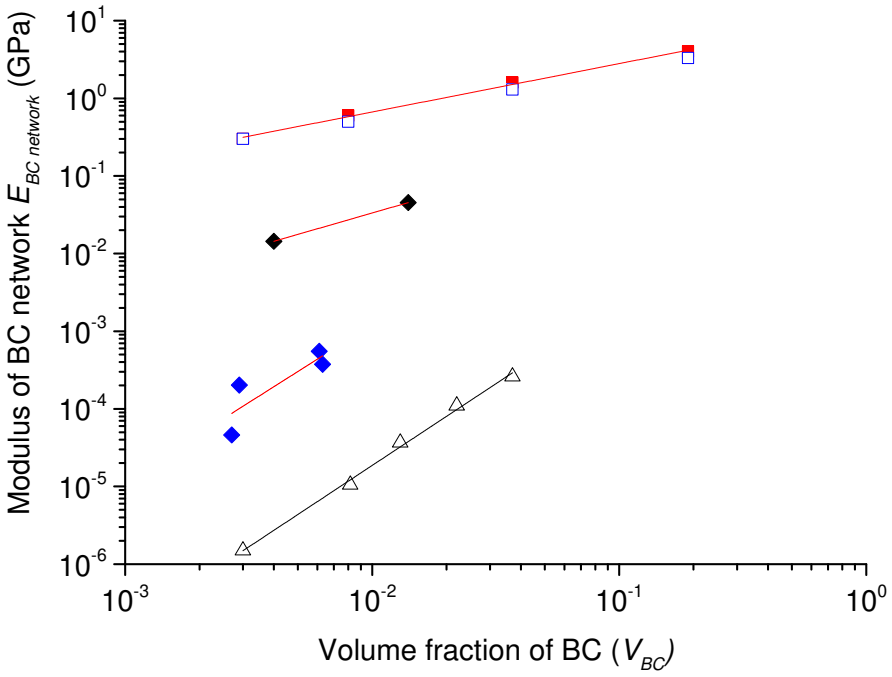

Figure 5-1. Double logarithmic plots of modulus of BC network versus volume fraction of BC for nanocomposites embedded with well-defined BC nanofiber and a BC hydrogel. The modulus of BC network was estimated from the method shown in Chapter 2. Symbols represent BC/PMMA resin composites (squares), BC/PEA elastomers (black diamonds), BC/bottle-brush hybrid gels (blue diamonds) and a BC gel (open triangles). Lines represent prediction of the modulus by linear fitting.

Table 5-1. Parameters for fitting line of nanocomposites with well-defined BC nanofiber and a BC hydrogel in Figure 5-1.

	Slope n	$E_{BC\ bulk}$ (GPa)
BC/PMMA composite	0.62	13
BC/PEA elastomer	0.92	2.3
PPEGMA-grafted BC/PBIEM gel	2.0	13
BC hydrogel	2.1	0.30

Subsequently, slopes for the BC/PMMA composites and the BC/PEA elastomers were roughly 1 which was consistent with the rule of mixtures, indicating large deformation by bending was extremely suppressed by the surrounding rigid matrix, resulting in stretch-dominated deformation was predominant. On the other hand, slope for the BC/bottle-brush hybrid gels and a BC hydrogel was around 2, which was inconsistent with assumption of the role of mixtures, indicating heterogeneous strain or sliding of entanglement of BC nanofiber was occurred. In any case, bend-dominated deformation of BC network was predominant. In addition, the difference of moduli between stretching and bending deformation was larger in the case of small fraction of network, therefore, effective reinforcement was achieved by introducing only a slight nano-sized network.

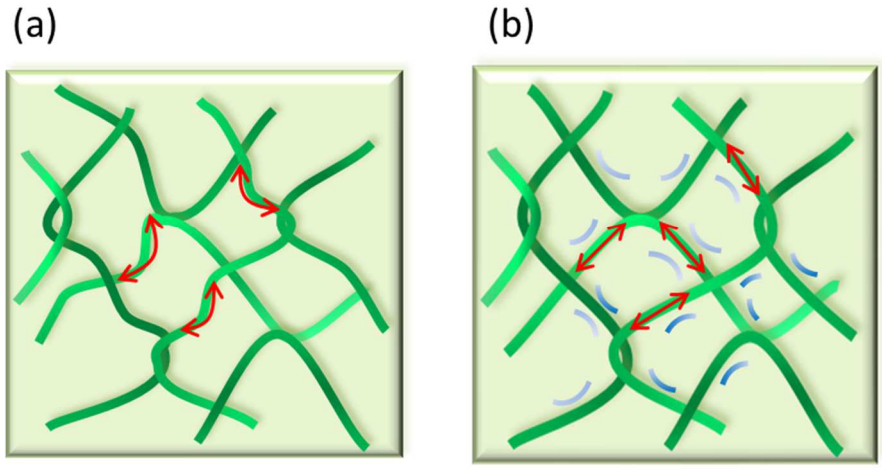

Figure 5-2. Illustration of behavior of network embedded in matrix. (a) bending-dominated deformation and (b) stretch-dominated deformation.

To summarize these results, the modulus of well-defined BC nanofiber network was shown linear increase with BC contents toward theoretically estimated modulus of BC bulk. As described in Figure 5-2, the BC network was shifted from bending-deformation to stretch-deformation depending on the increase of elasticity of matrices, i.e. composites were reinforced by suppression of

deformation of BC nanofiber network depending on elasticity of surrounding elastic matrices.

5-4. Conclusion

We have established the systematic understanding between deformation behavior and the modulus of BC nanofiber network embedded in matrices. The modulus of network was drastically improved by shifting bending to stretching deformation, especially in the case of small volume fraction of network. The composites were reinforced by suppression of deformation of BC nanofiber network depending on elasticity of surrounding elastic matrices. This systematic understanding can provide design toward functionalized composites embedded with network structure.

5-5. References

1. L. J. Gibson. M. F. Ashby. *Cellular solids: structure and properties*. *Cambridge university press.* **1999**.

2. M. F. Ashby. *Philos. Trans. R. Soc., A* **2006**, *364*, 15–30.

3. C. P. Broedersz, X. Mao, T. C. Lubensky, F. C. MacKintosh. *Nat. Phys.* **2011**, *7*, 983–988.

4. L. Wang, J. Lau, E. L. Thomas, M. C. Boyce. *Adv. Mater*. **2011**, *23*, 1524–1529.

5. O. Al-Ketan, M. A. Assad, R. K. A. Al-Rub. *Compos. Struct.* **2017**, *176*, 9–19.

6. A. Hirai, O. Inui, F. Horii, M. Tsuji. *Langmuir* **2009**, *25*, 497–502.

Part 2

Epoxy Resin-based Monolith Network

Chapter 6

Preparation, Structure and Tribological Property of Epoxy Resin-based Monolith Films by Dip Coating Method

6-1. Introduction

Soft materials composed of organic polymers were expected to be utilized as tribological materials from a viewpoint of followability derived from softness, resulting suppressing wear of sliding surfaces and mitigating impacts, in particular among them, plastics were lightweight and had superior self-lubricating compared to hard materials such as metals.[1–6] However, soft materials caused the increase of contact areas and ploughing force by large deformation, resulting in the increase of friction force.[7, 8] In addition, large deformation cause the spread of clearance, resulting in destabilization of sliding behavior. In roughly estimation, for example, clearance of journal bearings was designed roughly ten-thousandth of diameter,[9] accordingly, less than 10 μm of deformation is acceptable in the case of 10 cm in diameter.

To overcome these problems, layer structures composed of thin films on hard based-materials were commonly used, which were generally obtained by surface modification, coating, deposition, sputtering, and so on.[10] Deformation of soft materials was suppressed due to its thin thickness and a hard layer under them. As a result, the decrease of contact area was lead to the decrease of friction force derived from adhesion and ploughing.

Epoxy resin-based polymer monolith, which was formed by polymerization induced phase separation including the reaction of epoxy and amine monomers in non-reactive porogen, was high strength derived from the epoxy resin frame itself and fine network, in addition, high liquid holding property into the pores, therefore, it was focused on tribological applications.

Some approaches for preparation of monoliths were reported. Molding process was general for preparation of various kinds of shapes such as block, rod and membrane.[11-13] Suspension polymerization process was also possible to prepare particles.[14-17] In this study, we focused on dip coating method, which was one of the most simple and general approaches to deposit a thin film on a substrate uniformly. A thickness of the film was controlled by viscosity of liquid, pulling up speed of the substrate and surface tension of liquid. By optimizing their conditions, various films with wide range of thickness were coated on the substrate. Furthermore, various shapes of substrates such as a bearing with curved surface were applied.

In Chapter 6, our purpose of study was as follows. First of all, we demonstrated a new approach for preparation of an epoxy resin-based thin monolith on a substrate by dip coating method, which enabled to be applied various applications toward machine elements. In this method, the viscosity of polymerization mixture was the most important factor for controlling a film, which was affected thickness and uniformity of the film. In addition, the decrease of the viscosity during heating (polymerization) should be considered. Therefore, we controlled the viscosity of the polymerization mixture by adding silica nanoparticles and volatile solvent. The silica nanoparticles were expected to increase viscosity of the mixture and control the thickness of the film. The volatile solvent was expected to be volatilized to increase the viscosity of the film after coating on a substrate to suppress dripping during heating. In the second, tribological properties were discussed from a viewpoint of mechanical properties of monoliths depended on rigid substrates and resistance of fluid flow in the pores.

6-2. Experimental Section

6-2-1. Materials

1,3-Bis(*N,N'*-diglycidylaminoethyl)cyclohexane (TETRAD-C) (98%, Mitsubishi Gas Chemical

Company, Inc., Japan), bis(4-aminocyclohexyl)methane (BACM) (mixture of isomers, 97%, Wako), Polyethylene glycol 200 (PEG200) (averaged molecular weight: 190–210, Kishida Chemical Co., Ltd., Japan), 1-butyl-3-methylimidazolium iodide (BMIM-I) (KANTO CHEMICAL CO., INC., Japan), *N*,*N*-diethyl-*N*-methyl-*N*-(2-methoxyethyl)ammonium bis (trifluoromethane-sulfonyl)imide (DEME-TFSI) (KANTO CHEMICAL CO.,INC., Japan), acetone (99.5%, Super Dehydrated, Wako, Japan), methanol (1st grade, Wako), AEROSIL 130 (Hydrophilic fumed silica, Evonik Industries), a stainless steel (SUS) disk roughened by sand blast on one side (diameter 30 mm, thickness 2 mm, arithmetic average roughness R_a = 1.21 μm, Kumamoto Seiken Kogyo, Japan) and a glass lens (SLB-10-15P, BK-7, curvature radius 7.79 mm, Sigmakoki Co., Ltd., Japan) were used as received.

6-2-2. Preparation of monoliths on substrates

Thick monolith on a substrate

AEROSIL 130 (1.12 g, 2.0 wt%) was added into PEG200 (40 g) and stirred at 10000 rpm for 4 min using a homogenizer. BACM (5.75 g, 1 eq.) melted at 60 °C was dissolved in the mixture, followed by the addition of TETRAD-C (10 g, 1 eq.). The monomer mixture was stirred using with a mixer (Awatori-rentaro, THINKY Ltd.). The mixture was added slowly into a polypropylene container in which SUS disk was placed. The mixture was heated at the prescribed temperature (100 and 130 °C) for 1 h in an oven, removed the container, heated at 180 °C for 30 minutes. The sample was immersed in methanol overnight to remove PEG200, and dried under vacuum at 60 °C. The top-surface of the monolith was polished to remove a skin layer by using abrasive papers in order of #500, #1000 and #2000 in water in order to suppress deformation by heat of friction, yielding a thick monolith with 2 mm in thickness on a SUS disk (Figure 6-1(a)).

Thin monolith with 60 μm in thickness by dip coating

A SUS substrate and a slide glass masked backside by a protective tape was dipped into the

monomer mixture as mentioned above and pulled up vertically at the speed of 25 μm/s using micro-speed dip coater (MD-0408-S5, SDI Co., Ltd., Japan). The SUS substrate coated with the mixture was heated at the prescribed temperature (100 and 130 °C) for 1 h in an oven, heated at 180 °C for 30 minutes, immersed in methanol overnight to remove PEG200, and dried under vacuum at 60 °C, yielding a monolith on the SUS disk and the slide glass with a thickness of around 60 μm (Figure 6-1(b)).

Thin monolith with 30 μm in thickness by dip coating

Acetone (20 wt%) was added in the monomer mixture, otherwise the same described as above, yielding a monolith on substrates with a thickness of around 30 μm.

6-2-3. Characterization

Field emission scanning electron microscopy (FE-SEM) observations were carried out on a JEOL JSM-6700F SEM operated at 1.5 kV or 3.0 kV. During the preparation of samples for cross-sectional observations, the samples were fractured in liquid nitrogen to obtain fresh cross sections. Prior to SEM observations, the samples were sputter-coated with a thin layer of platinum to enhance their conductivity (Hitachi ion sputter E-1010); sputter time: 20 s; coat thickness: ca. 5 nm.

6-2-4. Measurements

Indentation

The monolith was immersed in DEME-TFSI under vacuum overnight for intrusion of DEME-TFSI in pores. Load and displacement were measured using tribometer (UMT, Bruker Co., United States) equipped with a 50N-load cell sensor (DFH-5, Bruker Co.). A glass lens glued to a pin was used as an indenter and pressed at a speed of 40 N/min on a surface of the monolith. Displacement was estimated by correcting displacement of spring in the load cell sensor.

Frictional measurement by ball on disk method

Before measurements, the monoliths were immersed BMIM-I or DEME-TFSI under vacuum overnight. The friction force and friction coefficient of a monolith on a SUS disk were measured by ball on disc type of a rotatory tribometer equipped with the 50N-load cell sensor, a dumper and a rotary drive at 25 °C. A glass lens glued to a pin was set on the location with a distance of 5–10 mm from center of a rotary drive. BMIM-I (1340 cP at 25 °C) and DEME-TFSI (71 cP at 25 °C) were used as lubricants. The normal loads (F) were 0.1, 1 and 4 N and the number of rotation was from 1000 to 1 rpm in stepwise, corresponding to 5.2×10^{-4}–1.1 m/s of sliding velocity. The rotary direction was switched clockwise to counter clockwise at each sliding velocity. Friction force (F_s) was defined as an average of detected absolute value in clockwise and counterclockwise rotation. Friction coefficient (μ) was defined as F_s/F.

6-3. Results and discussion

6-3-1. Preparation of thick and thin monoliths with skinless on a substrate

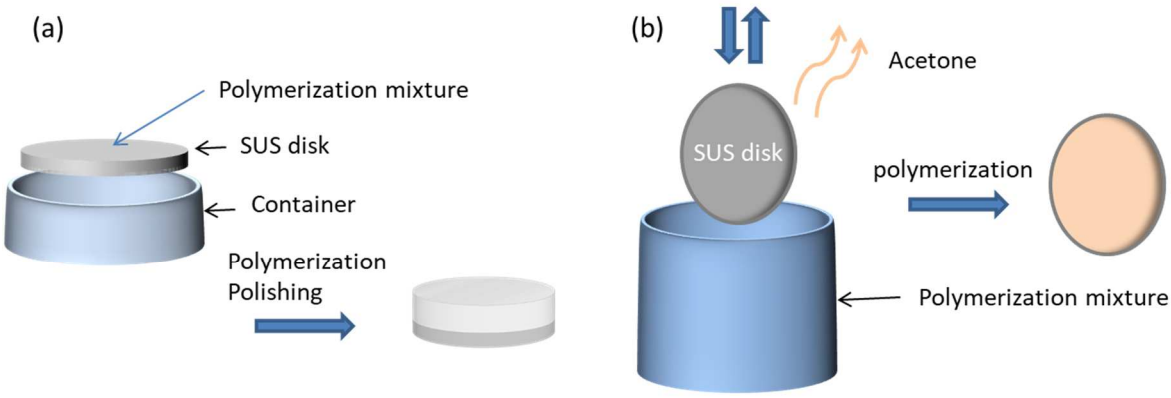

Figure 6-1. Preparation of (a) a thick monolith by molding and (b) thin monoliths by dip coating method.

Figure 6-1 shows preparation method for thick and thin monoliths with skinless. At first, thick monoliths were prepared by molding process, followed by polishing of a skin layer. The monomer mixture was added on a substrate in a container, followed by heating. A skin layer was removed by polishing. Next, thin monoliths were prepared by dip coating process. Thickness of a monolith film was controlled by adjusting viscosity of monomer mixture. Silica nanoparticles and acetone were used to control viscosity of monomer mixture and mixture film on the substrate. Acetone was expected to suppress dripping of mixture film on a substrate with the increase of viscosity by volatilizing.

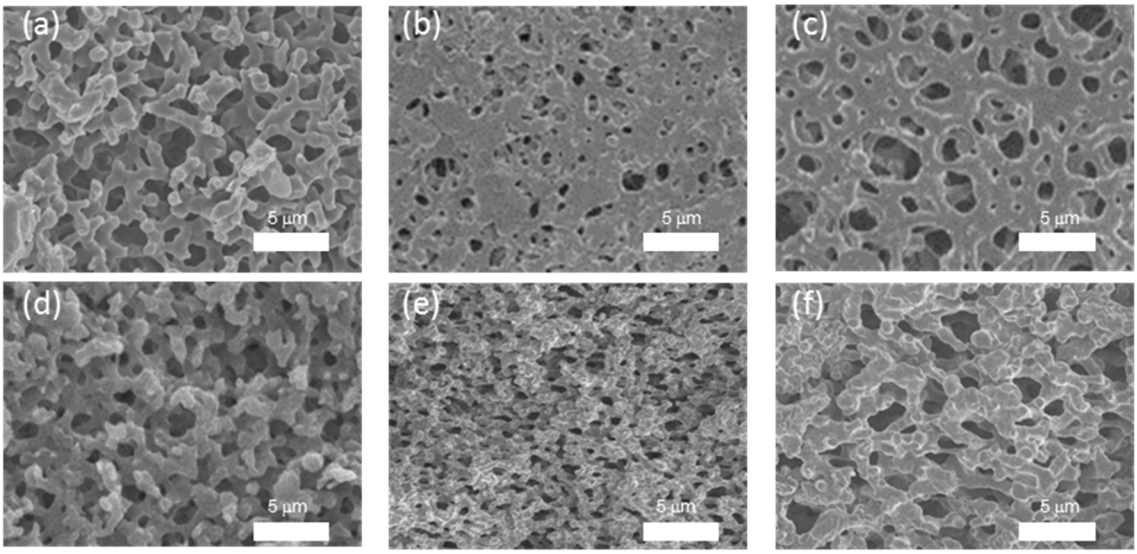

Figure 6-2. FE-SEM images of monoliths prepared at 100 °C. Top-surface of (a) a thick monolith after polishing and (b), (c) thin monoliths with a thickness of 60 μm and 30 μm prepared by dip coating. Cross-section of (d) a thick monolith and (e), (f) thin monoliths with a thickness of 60 μm and 30 μm.

Figure 6-2 shows top-surface and cross-sectional FE-SEM images of a thick monolith and thin monoliths with around 60 μm, 30 μm in thickness prepared at 100 °C. For the observation by

FE-SEM, thin monoliths were prepared on slide glasses. Both a thick and thin monoliths were prepared by adding silica nanoparticles (2.0 wt%) in the monomer mixture. In the case of the thin monolith with 30 μm, acetone (20 wt%) was also added. A skin layer of a thick monolith, which was formed due to smaller surface tension of epoxy resin than that of PEG, was removed by polishing with abrasive papers in water, yielding a thick monolith with skinless surface without deformation of epoxy resin frameworks (Figure 6-2 (a)). On the other hands, as shown in Figure 6-2 (b) and (c), pores were formed on top-surface with skinless in the case of thin monoliths. Pore size of the thin monolith with 60 μm in thickness was smaller than that of thick monolith and the thin monolith with 30 μm in thickness, which was probably due to rapid heat transfer derived from the thickness and small reaction rate derived from remaining acetone during heating.

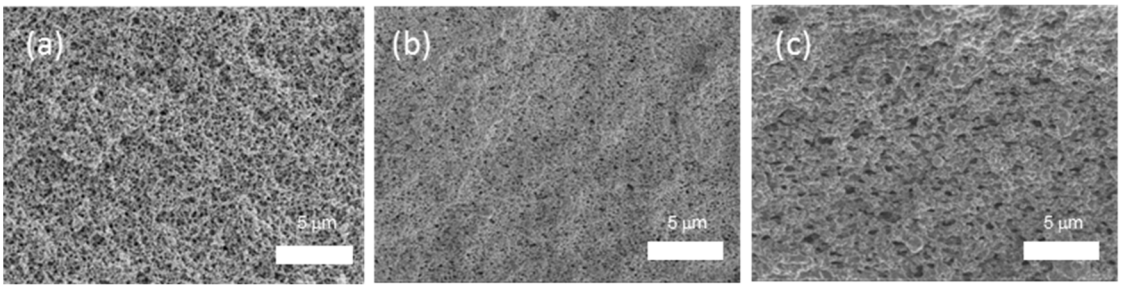

Figure 6-3. Cross-sectional FE-SEM images of (a) a thick monolith and thin monoliths with (b) 60 μm and (c) 30 μm in thickness at 130°C.

Figure 6-3 shows cross-sectional FE-SEM images of a thick monolith and thin monoliths with 60 μm and 30 μm in thickness prepared at 130 °C. Pore sizes of the thick and thin monolith with 30 μm in thickness at 130 °C was rather larger than that of the thin monolith with 60 μm in thickness, whereas much smaller than that of monoliths prepared at 100 °C. Pore sizes of thick monoliths at 100 °C and 130 °C were estimated 180 nm and 80 nm by mercury intrusion porosimetry,

respectively. Accordingly, pore sizes of monoliths were mainly controlled by polymerization temperature.

6-3-2. Mechanical properties of monoliths

Figure 6-4 shows normal load against compression displacement of monoliths prepared at 130°C and 100°C. Monoliths filled with DEME-TFSI in pores were suppressed deformation compared to dried monoliths probably due to fluid resistance in the pores. Subsequently, displacement of monoliths with 2 mm and 30 μm in thickness at 30 N was around 90 μm 10 μm, respectively, that is, small deformation could be attained by thinning the monolith film.

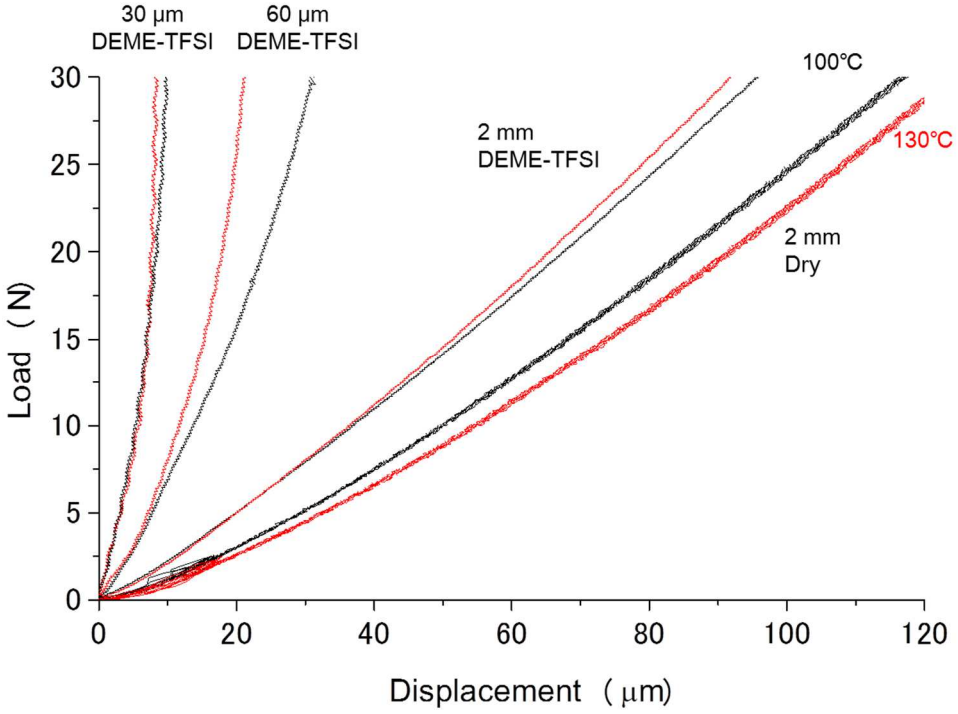

Figure 6-4. Normal load against compression displacement of a dried thick monolith and monoliths with 2 mm, 60 μm and 30μm in thickness with DEME-TFSI prepared at 130°C (red) and 100°C (black).

Herein, the elastic moduli of opposite materials were assumed by using Hertzian contact equation with deformation depth δ and applied load F as below.

$$\delta = \frac{a^2}{R} = \left(\frac{9}{4}\frac{F^2}{RE^2}\right)^{1/3} \quad (6-1)$$

$$\frac{2}{E} = \frac{1-\nu_1^2}{E_1} + \frac{1-\nu_2^2}{E_2} \quad (6-2)$$

where, a and R were static contact radius and curvature radius. E_1, E_2, ν_1 and ν_2 were elastic modulus and poisson's ratio of a glass lens and a monolith, respectively. The modulus of a glass lens was assumed 80 GPa. Poisson's ratio of a glass lens and a monolith was assumed 0.23 and 0.3, respectively.

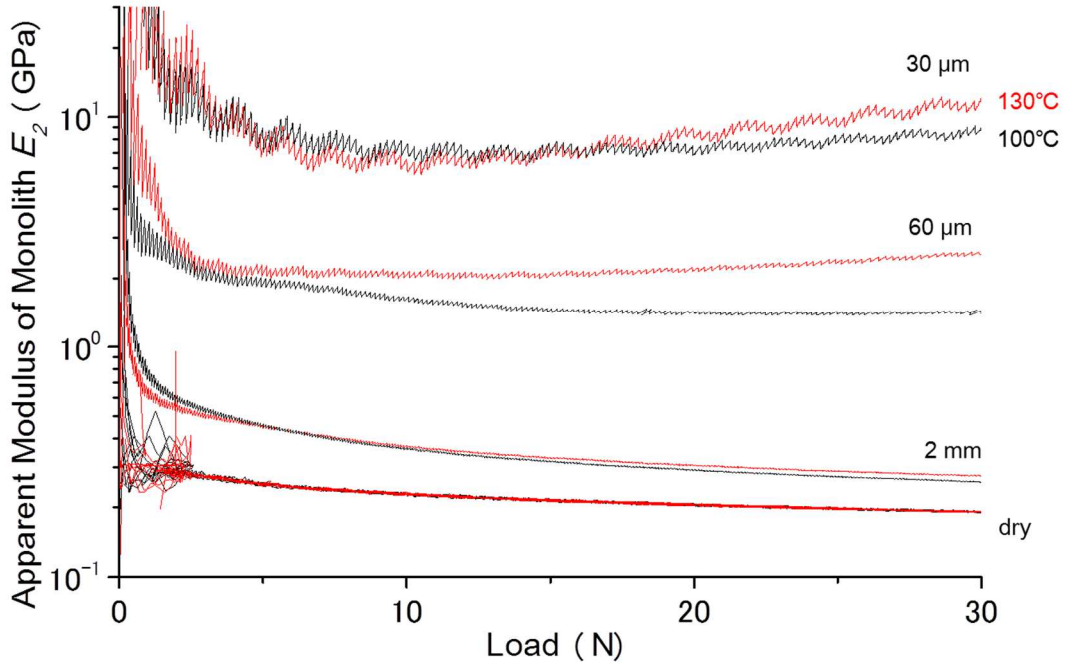

Figure 6-5. Apparent modulus against the normal load for dried monolith with 2 mm in thickness and monoliths with DEME-TFSI with 2 mm, 60 μm and 30μm in thickness prepared at 130°C (red) and 100°C (black).

Figure 6-5 shows apparent modulus of dried monoliths and on substrates with DEME-TFSI against

the normal load. The large apparent modulus at small loads was due to small estimation of radius because interaction between the two surfaces was ignored. The modulus of monoliths with DEME-TFSI was larger than that of dried monoliths, indicating the fluid resistance in the pores was affected. The apparent elastic moduli of monoliths with 2 mm in thickness decreased gradually at the range of 1–30 N, indicating the less influence of the substrate, whereas in the case of thin monoliths, influence of the substrate was observed even at small load, indicating the load transfer to the substrate was effective because of rigid network of monoliths. From these results, small deformation less than 10 μm could be attained by the thin monolith on the rigid substrate, suggesting the potential for application of machine elements which was required precise and small clearance.

6-3-3. Frictional properties of monoliths

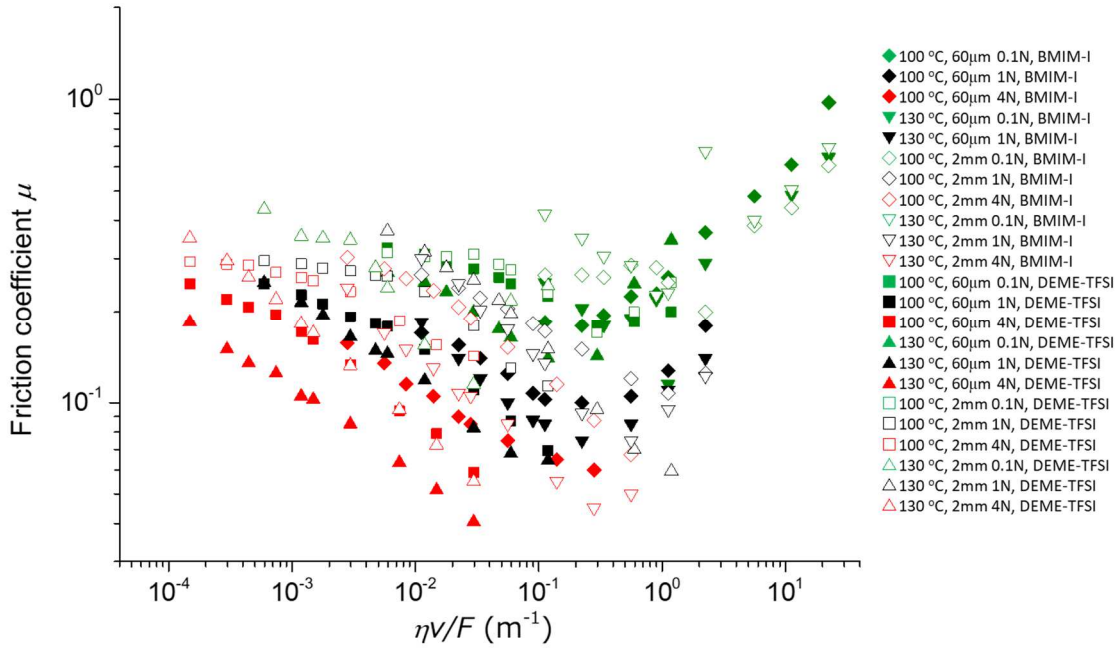

Figure 6-6. Plots of friction coefficient μ against characteristic parameter $\eta v/F$ for monoliths with a thickness of 2 mm (open symbols) and 60 μm (closed symbols) prepared at 130°C and 100°C. BMIM-I and DEME-TFSI were used as lubricants.

Figure 6-6 shows plots of μ against characteristic parameter $\eta v/F$, i.e. Stribeck curve for monoliths with a thickness of 2 mm and 60 μm. The parameters η, v, and F were viscosity of lubricants, sliding velocity and normal load, respectively. BMIM-I and DEME-TFSI were used as lubricants, which enabled wide range of measurement as the parameter $\eta v/F$ because of large difference of viscosity. In generally, Stribeck curve was divided three types of regimes; hydrodynamic lubrication, mixed lubrication and boundary lubrication regime. In the hydrodynamic lubrication regime, μ decreased with decreasing sliding speeds, considering the μ was determined by viscosity of the fluid film between two surfaces. In the mixed lubrication regime, μ was shifted increasing with decreasing sliding speeds, considering due to the increase of contact area with two surfaces. In the boundary lubrication regime, μ was shifted constant with decreasing sliding speeds, considered contact area with two surfaces was become constant. In Figure 6-6, mixed lubrication regime was appeared in wide range of parameter, in which the μ was affected all parameters of η, v, F, monolith thickness and pore size, i.e. i) the μ decreased with the increase of sliding velocity and normal load, ii) the μ in DEME-TFSI was lower than those in BMIM-I, iii) the μ prepared at 130°C was lower than that at 100°C and iv) the μ with a thickness of 60 μm was smaller than that with a thickness of 2 mm.

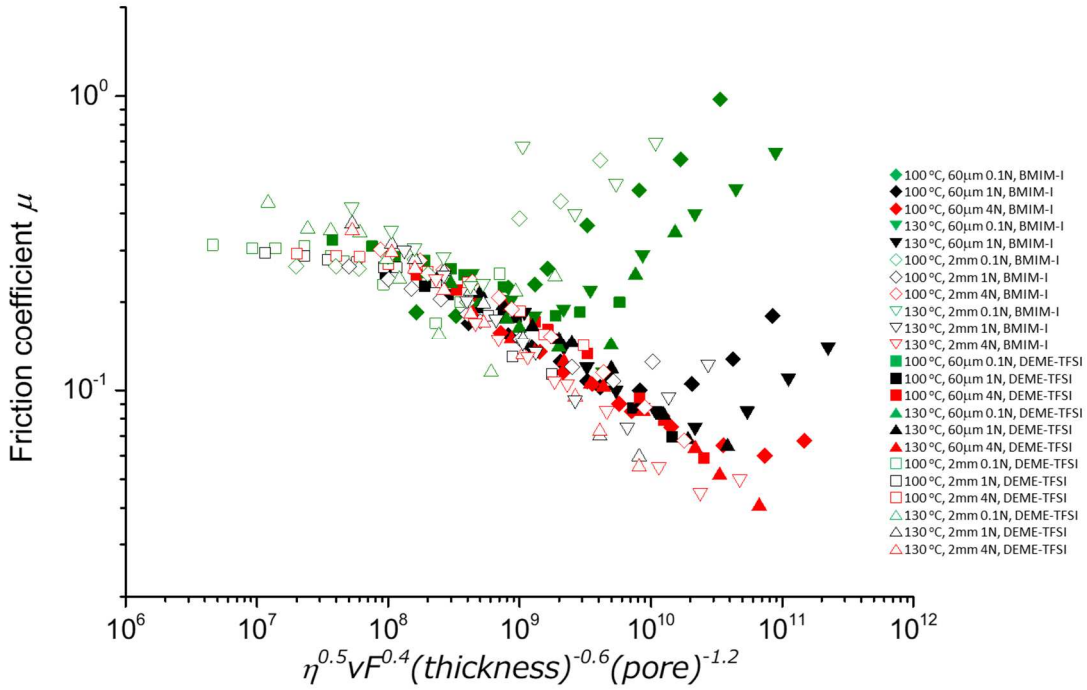

Figure 6-7. Plots of friction coefficient μ against parameter $\eta^{0.5} \upsilon F^{0.4}$ (thickness)$^{-0.6}$ (pore)$^{-1.2}$ for monoliths with a thickness of 2 mm (open symbols) and 60 μm (closed symbols) prepared at 130°C and 100°C.

Herein, dependence on parameters of η, υ, F, thickness and pore size of a monolith was discussed. Figure 6-7 shows plots of μ against a parameter $\eta^{0.5} \upsilon F^{0.4}$ (thickness)$^{-0.6}$ (pore size)$^{-1.2}$ for monoliths with a thickness of 2 mm and 60 μm. Pore size of thin monoliths was assumed same as that of thick monoliths. In the mixed lubrication, curves of plots were overlapped against this parameter. It should be noted that F was positive correlation, so that the μ decreased with the increase of F, indicating exuding of lubricants was suppressed the contact of sliding surfaces. In addition, thickness and pore size of a monolith were negative correlation, indicating ploughing force and flow behavior such as paths and resistance in the pores were affected frictional property. Furthermore, the μ was proportional to the 0.5 power of η, which was less than 1, indicating that lubricant was flowed into the pores, which cause the decrease of apparent viscosity.

6-4. Conclusion

We demonstrated the new approach for preparation of monolith film on flat and curved substrates uniformly by dip coating method. Wide range of film thickness was applied by controlling the viscosity of polymerization mixture during dip coating and heating. Thus obtained thin monolith with lubricants was apparently reinforced by a rigid substrate and resistance of liquid flow, resulting suppression of the deformation. Friction coefficient of monoliths was described as parameter $\eta^{0.5} v F^{0.4}$ (thickness)$^{-0.6}$ (pore size)$^{-1.2}$. The μ was decreased with the increase of normal loads and the decrease of thickness and pore sizes in the mixed lubrication, furthermore, the μ was proportional to 0.5 power of viscosity of lubricant, indicating mechanical properties and flow behavior including exuding, paths and resistance of flow in pores were affected frictional properties. Accordingly, we revealed the potential of epoxy-based thin monoliths on rigid substrates toward tribological soft materials with advantages of small deformation and fluid flow in pores.

6-5. References

1. Y, Fujii. *Tribol. Int.* **2008**, *41*, 17–23.

2. S. Bahadur. *Wear* **2000**, *245*, 92–99.

3. N. Marx, J. Guegan, H. A. Spikes. *Tribol. Int.* **2016**, *99*, 267–277.

4. P. Sadowski, S. Stupkiewicz. *Tribol. Int.* **2019**,*129*, 246–256.

5. E. Omrani, P. L. Menezes, P. K. Rohatgi. *Int. J. Eng. Sci. Technol.* **2016**, *19*, 717–736.

6. J. H. H. Bongaerts, K. Fourtouni, J. R. Stokes. *Tribol. Int.* **2007**, *40*, 1531–1542.

7. N. K. Myshkin, M. I. Petrokovets, A. V. Kovalev. *Tribol. Int.* **2005**, *38*, 910–921.

8. N. Maeda, N. Chen, M. Tirrell, J. N. Israelachvili. *Science* **2002**, *297*, 379–382.

9. B. J. Hamrock, S. R. Schmid, B. O. Jacobson. *Fundamentals of fluid film lubrication* **2004**.

10. K. Holmberg, A. Mathews. *Thin Solid Films* **1994**, *253*, 173–178.

11. K. Sakakibara, H. Kagata, N. Ishizuka, T. Sato, Y. Tsujii. *J. Mater. Chem. A* **2017**, *5*, 6866–6873.

12. K. Hosoya, H. Hira, K. Yamamoto, M. Nishimura, N. Tanaka. *Anal. Chem.* **2006**, *78*, 5729–5735.

13. N. P. Dinh, Q. M. Cam, A. M. Nguyen, A. Shchukarev, K. Irgum. *J. Sep. Sci.* **2009**, *32*, 2556–2264.

14. A. M. Nguyen, K. Irgum. *Chem. Mater.* **2006**, *18*, 6308–6315.

15. K. Sakakibara, K. Konishi, N. Ishizuka, A. Goto, Y. Tsujii. *Polym. Chem.* **2018**, *9*, 414-419.

16. M. T. Gokmen, F. E. Du Prez. *Prog. Polym. Sci*. **2012**, *37*, 365–405.

17. B. Wang, P. Prinsen, H. Wang, Z. Bai, H. Wang, R. Luque, J. Xuan. *Chem. Soc. Rev.* **2017**, *46*, 855–914.

Chapter 7

Understanding of Tribological Property of Epoxy Resin-based Monoliths by Simultaneous Measurement of Optical Interferometry

7-1. Introduction

Epoxy resin-based polymer monoliths, which were formed by polymerization induced phase separation including the reaction of epoxy and amine monomers in non-reactive porogen, was high strength derived from the epoxy resin frame itself and fine network, in addition, the monolith was expected some kinds of surface texturing effect in terms of surface structure and high liquid holding into the pores, therefore, it was focused on tribological applications.

Surface texturing such as a dimple and a groove pattern was widely utilized for tribological materials.[1] Advantages of surface texturing were expanding the range of mixed lubrication and elasto-hydrodynamic lubrication (EHL) by producing hydrodynamic pressure derived from reserving and controlling flow of lubricants on the sliding surface, therefore, a large amount of studies were reported experimentally and theoretically for rigid materials.[2-7] Recently, surface texturing of soft materials was also focused on because of advantages of wear resistance, mitigating impacts and exuding lubricants derived from large deformation.[8-11] Theoretically studies were also focused on cavitation and deformation phenomenon, which were one of the most important factors in the mixed lubrication and soft EHL.[12-14]

In previous chapter, we revealed superior frictional properties of epoxy-based thin monoliths from the viewpoint of mechanical properties, i.e. the increase of apparent modulus derived from rigid substrates and fluid flow in pores affected the frictional behavior. On the other hands, despite the monolith was also expected smooth transfer from boundary lubrication to hydrodynamic lubrication

in poor lubrication or starting up due to the exuding of fluid in pores, behavior of sliding surface including effect of surface roughness, fluid reservation, exuding and flow was not revealed.

In Chapter 7, we demonstrate understanding of tribological properties in the mixed lubrication and soft EHL from the viewpoint of the behavior of sliding surface by using simultaneous measurement of optical interferometry. This technique is generally used in order to obtain information such as sliding surface such as fluid flow, fluid film thickness and contact region.[15] However, there are two difficulty to apply this technique to the monolith; i) it is difficult to apply generally used ball-on disk type apparatus consisted of reflective ball and transparent disk because a monolith is not transparent due to the difference of reflective index between the monolith and lubricants and ii) surface roughness including pores of polymer monoliths was affected optical interferometry.[16] To overcome these problems, in the former, a semi-reflective plano-convex glass lens and a surface-reflective monolith on a substrate were used and sliding surface was observed from the flat surface of the lens. In the latter, poly(vinyl alcohol) (PVA)-laminate method was applied to prepare surface-smooth monolith with skinless, which has reported by Sakakibara at al.[17] Our goal was tribological properties in the mixed and soft-EHL of monoliths were revealed by the optical interferometry technique to provide guideline to improve them further, in specially, in poor lubrication of monoliths utilizing the advantage of exuding.

7-2. Experimental Section

7-2-1. Materials

1,3-Bis(*N,N'*-diglycidylaminoethyl)cyclohexane (TETRAD-C) (98%, Mitsubishi Gas Chemical Company, Inc., Japan), bis(4-aminocyclohexyl)methane (BACM) (mixture of isomers, 97%, Wako, Japan), Polyethylene glycol 200 (PEG200) (averaged molecular weight: 190–210, Kishida Chemical Co., Ltd., Japan), methanol (1st grade, Wako), poly-α-olefin (PAO) 10 (Durasyn 170) (110 cP at

25 °C, poly-*α*-olefin, INEOS Oligomers) and PAO100 (Durasyn 180I) (2410 cP at 25 °C, poly-*α*-olefin, INEOS Oligomers) were used as received. PVA-coated glasses were prepared as follows: a PVA solution in water (1.0 wt%) was spin-coated on a glass substrate (7.5 × 7.5 cm^2) at 2000 rpm for 20 s, and the substrate was dried at 105 °C for 1 h. A stainless steel (SUS) disk roughened by sand blast on one side (Diameter 30 mm, thickness 2 mm, R_a = 1.21 μm, Kumamoto Seiken Kogyo, Japan), a plano-convex glass lens (SLB-10-15P, BK-7, curvature radius 7.79 mm, Sigmakoki Co., Ltd., Japan) were washed with hexane, followed by acetone by sonication for 10 minutes.

7-2-2. Aluminum-coated monolith by PVA-laminate method

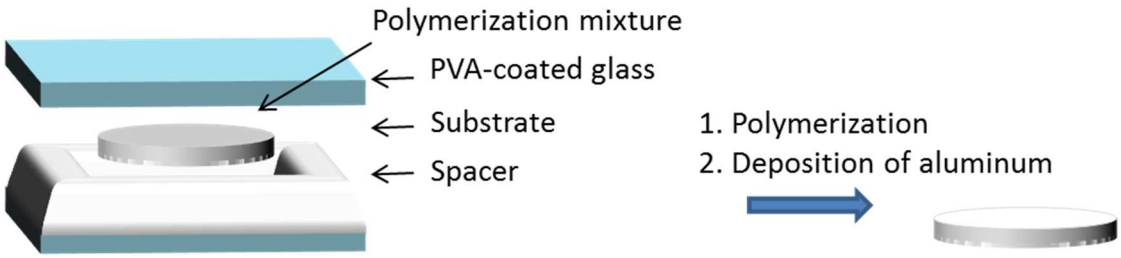

Figure 7-1. Preparation of aluminum-coated monolith by PVA-laminate method.

Figure 7-1 shows a schematic preparation of a monolith by PVA-laminate method. PVA-coated glass was placed on the top of polymerization mixture with spacers, followed by polymerization and peeling of the PVA film, yielding a monolith on a substrate. Thickness of the monolith was controlled by spacers. In details, BACM (0.5745 g) melted at 60 °C was dissolved in PEG200 (4.0 g), followed by addition of TETRAD-C (1.0 g). A monomer mixture was stirred using a mixer (Awatori-rentaro, THINKY Ltd., Japan). The mixture was placed on a SUS substrate with a spacer on a PVA-coated glass substrate, and another PVA-coated glass substrate was placed on top of the

spacer. The sample was clamped with double clips, then, heated at 130 °C for 1 h, followed at 180 °C for 30 minutes in an oven. The sample was immersed in methanol overnight to remove PEG200 and unreactive monomer, and dried under vacuum. Aluminum was deposited 15 nm in thickness on the monolith using vacuum deposition apparatus (V-KS200, Osaka Vacuum, Ltd., Japan), yielding an Al-coated monolith. The monolith was immersed in PAO10 or PAO100 under vacuum overnight.

7-2-3. Characterization

Field emission scanning electron microscopy (FE-SEM) observations were carried out on a JEOL JSM-6700F SEM operated at 3.0 kV. During the preparation of samples for cross-sectional observations, the samples were fractured in liquid nitrogen to obtain fresh cross sections. Prior to SEM observations, the samples were sputter-coated with a thin layer of platinum to enhance their conductivity (Hitachi ion sputter E-1010); sputter time: 20 s; coat thickness: ca. 5 nm.

7-2-4. Measurements

Frictional measurement and observation of sliding surface by optical interferometry technique

Figure 7-2 shows schematically illustrated set up for frictional measurement and observation of surface of a monolith. Cr film with 5 nm in thickness was coated on a plano-convex glass lens by a spatter, then, silica film with 480 nm in thickness was coated, yielding a Cr-SiO_2-coated glass lens. Aluminum with 15 nm of in thickness was deposited on a monolith.

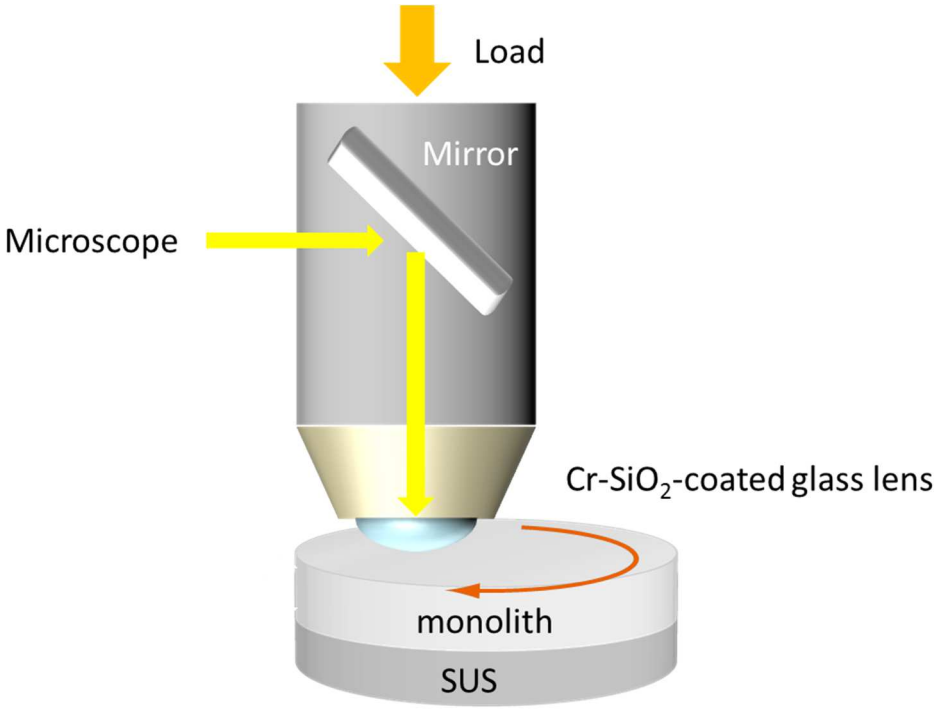

Figure 7-2. Schematic ball-on-disk method set up for frictional measurement and observation of surface of a monolith.

The friction force and friction coefficient were measured by ball on disc type of a rotatory tribometer (UMT, Bruker Co., United States) equipped with a 50N-load cell sensor (DFH-5, Bruker), a dumper and a rotary drive at 25 °C. A monolith was immersed in lubricants under vacuum overnight for intrusion in pores. The monolith was observed and recorded continuously by using a microscope equipped with a video camera (VH-Z50L, KEYENCE, Japan) from the back of the lens. A mirror was placed above the surface at an angle of 45°. A Cr-SiO_2-coated glass lens was set on the location with a distance of 5–10 mm from the center of a rotary disk. PAO10 and PAO100 were used as lubricants. The normal loads (F) were 1, 4 and 10 N and number of rotation was from 500 to 1 rpm in stepwise corresponding to 5.2×10^{-4}–0.52 m/s of sliding velocity, followed by switching rotary direction clockwise to counterclockwise. Friction force (F_s) was defined as average of detected absolute value in clockwise and counterclockwise rotation. Friction coefficient (μ) was

defined as F_s/F.

Poor lubrication measurement

Lubricants on the surface of a monolith were wiped using soft papers repeatedly, then, friction force and friction coefficient were measured by ball on disc type of the rotatory tribometer, as mentioned above.

Fluid Film thickness

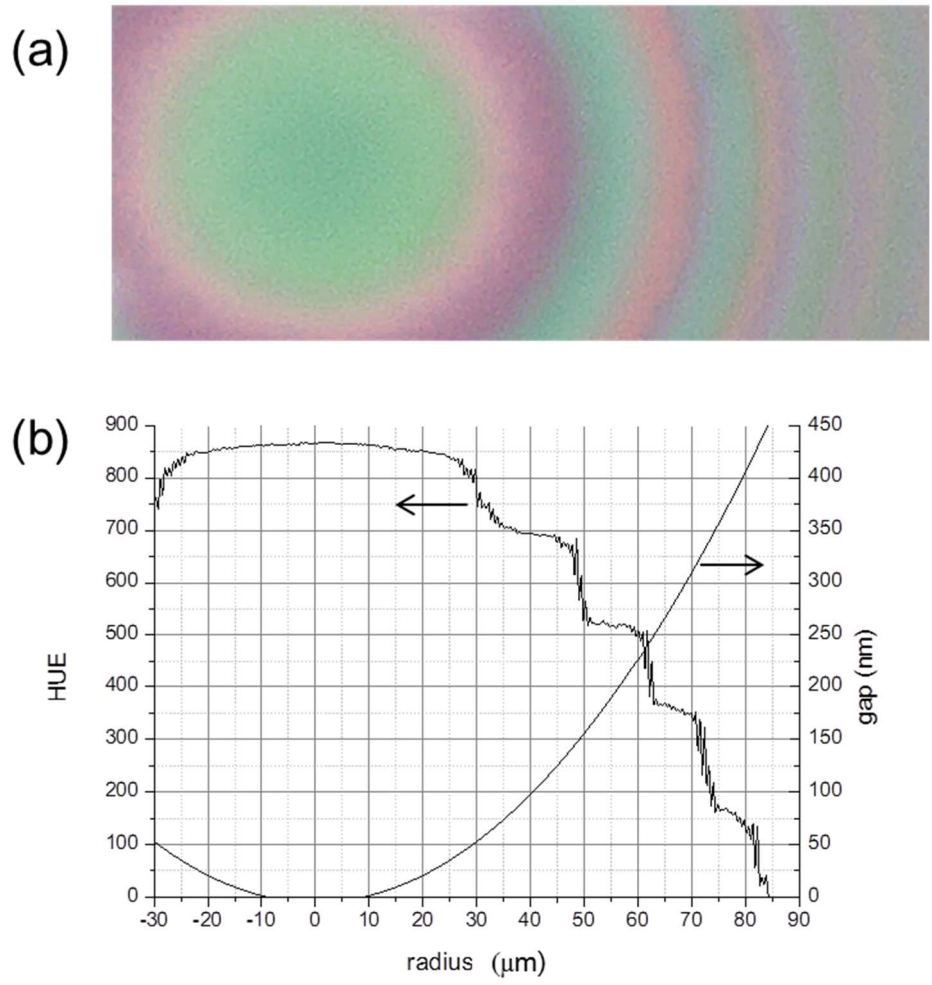

Figure 7-3. Calibration between hue value and gap distance. (a) Microscopic image of circular interferogram of Cr-SiO_2-coated lens on an Al-coated glass with PAO10 and (b) hue value and gap distance profiles against the radius of a lens.

Film thickness of lubricants was estimated by interferogram method. Figure 7-3(a) shows interferogram of a Cr-SiO_2-coated lens on an Al-coated slide glass in PAO10. RGB values were measured along equator, then, converted to corresponding hue values of 0 to 360.[18] Interference order and hue value order were estimated by comparing each sliding speed. Calibration between the hue value and gap distance was performed from relationship between radius of lens and gap in Figure 7-3(b).

Indentation

Indentation was performed using the tribometer described in figure 7-2. The surface of a monolith with PAO10 in pores was wiped by soft papers repeatedly. The monolith with PAO10 was pressed at a speed of 0.8 N/s by the Cr-SiO_2-coated lens.

7-3. Results and discussion

7-3-1. Preparation of Al-coated monolith on a substrate

In order to observe interference fringes on sliding surface, aluminum was deposited on the surface of a monolith. An Al-coated monolith prepared by using polishing skin layer was impossible to observe interference fringes probably due to large roughness of the surface, hence, a skinless monolith was prepared by PVA-laminate method including a sandwiching process (Figure 7-1). In order to suppress to form a skin layer on surface, PVA-coated glass substrate was contacted on surface of the polymerization mixture. Because PVA was hydrophilic and soluble in water, it was expected to suppress formation of a hydrophobic skin layer and easily peeling of the monolith from the glass substrate.

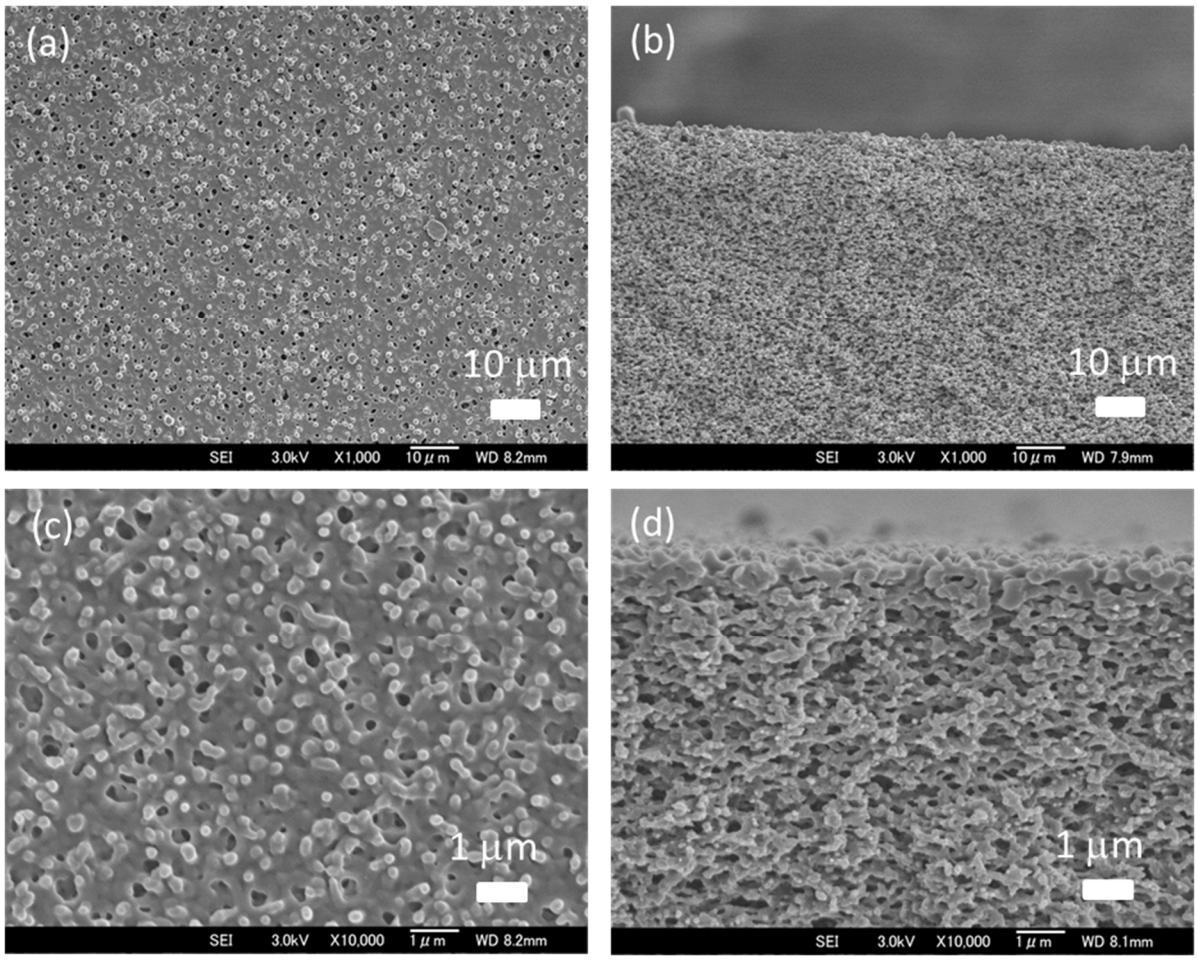

Figure 7-4. FE-SEM images of monoliths prepared by PVA-laminate method. Top-surface and cross-section of monoliths with a 170 μm in thickness (a),(b) at 100°C and (c),(d) at 130°C.

In the case using the spacer with 200 μm, a monolith with 170 μm in thickness was obtained, probably due to shrinking by annealing. Figure 7-4 shows top-surface and cross-sectional FE-SEM images of monoliths prepared by using PVA-laminate method with 170 μm in thickness at 100°C and 130°C. Pores were observed on the surface of the monolith with skinless. Pore sizes were controlled by polymerization temperature. In the case a Cr-coated glass lens was contacted on the surface of the Al-coated monolith prepared at 130°C, a circular optical interferogram was observed. On the other hands, in the case of the Al-coated monolith prepared at 100°C, a mottled-patterned interferogram was observed non-clearly, probably because aluminum was deposited inside pores,

which caused disturbance of interference. Therefore, the monolith prepared at 130°C was adapted.

7-3-2. Observation of sliding surface by an optical interferometry technique

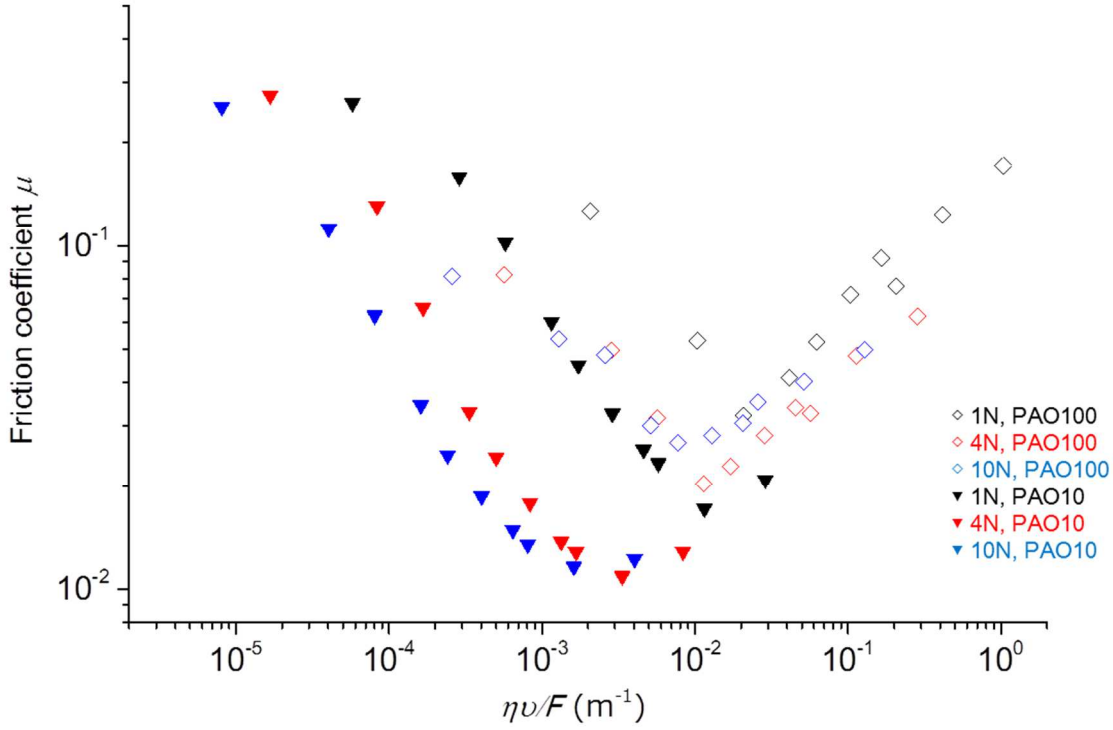

Figure 7-5. Plots of friction coefficient μ against characteristic parameter $\eta\upsilon/F$ for Al-coated monoliths prepared at 130 °C versus a Cr-SiO_2-coated lens with PAO10 (closed triangles) and PAO100 (open diamonds).

Subsequently, tribological measurement was performed by simultaneous measurement of optical interferometry. Figure 7-5 shows Stribeck plots of μ against characteristic parameter $\eta\upsilon/F$ for Al-coated monoliths with a thickness of 170 μm versus the Cr-SiO_2-coated lens. PAO 10 and PAO 100 were used as lubricants which were industrially used as base oils. The parameters η, υ, and F were viscosity, sliding velocity and normal load, respectively. In generally, Stribeck curve was divided three types of regimes; hydrodynamic lubrication, mixed lubrication and boundary

lubrication regime. In the hydrodynamic lubrication regime, μ decreased with decreasing sliding speeds, considering the μ was determined by viscosity of the fluid film between two surfaces. In the mixed lubrication regime, μ was shifted increasing with decreasing sliding speeds, considering due to the increase of contact area with two surfaces. In the boundary lubrication regime, μ was shifted constant with decreasing sliding speeds, considered contact area with two surfaces was become constant. In Figure 7-5, mixed and hydrodynamic lubrication regimes were appeared mainly. In the hydrodynamic lubrication regime, plots were roughly overlapped at any loads. In the mixed lubrication regime, μ decreased with the increase of normal load from 1 to 10 N, suggesting frictional behavior could not expressed by $\eta v/F$. In addition, μ lubricated with PAO 100 was much larger than that with PAO10 at similar $\eta v/F$, indicating apparent viscosity decreased.

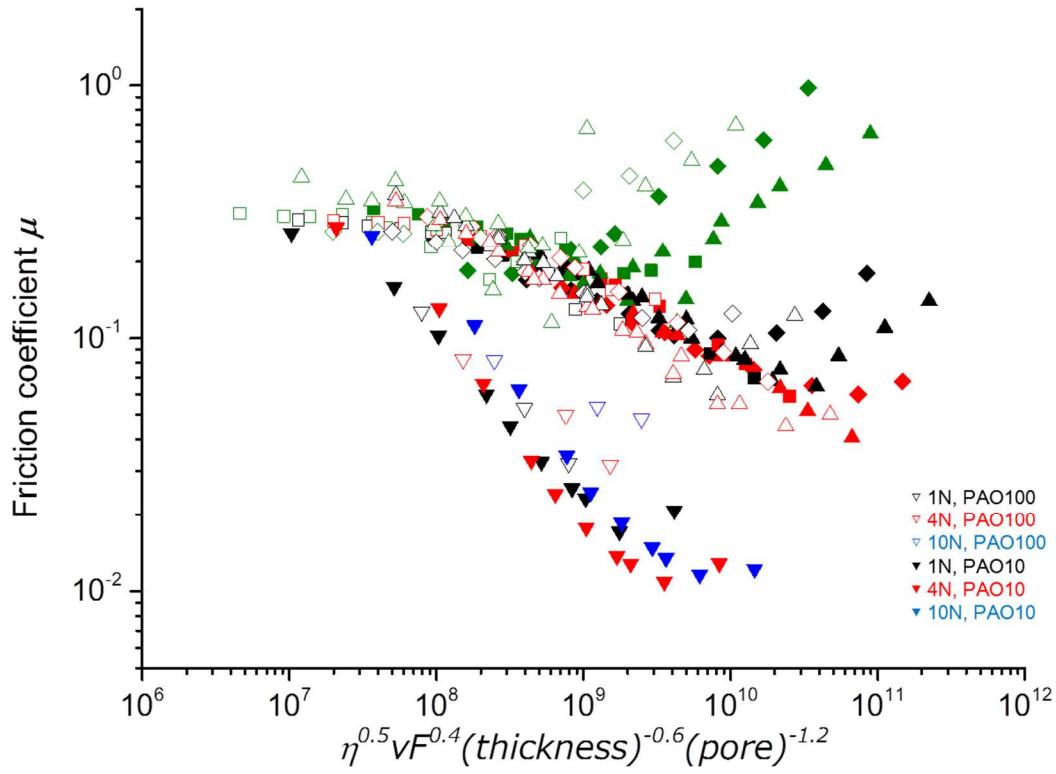

Figure 7-6. Plots of friction coefficient μ against parameter $\eta^{0.5} v F^{0.4}$ (thickness)$^{-0.6}$ (pore)$^{-1.2}$ for monoliths in Chapter 6 (Figure 6-7) and Al-coated monoliths with PAO10 and PAO100 in Figure 7-5 at 1 N (black), 4 N (red) and 10 N (blue).

Figure 7-6 shows plots of friction coefficient μ against parameter $\eta^{0.5} v F^{0.4}$ (thickness)$^{-0.6}$ (pore)$^{-1.2}$ for monoliths in Chapter 6 (Figure 6-7) and monoliths with PAO10 in Figure 7-5. In the mixed lubrication, plots for the Al-coated monolith at 1, 4, 10 N were overlapped against this parameter. On the other hand, the μ of the Al-coated monolith was extremely lower than that of non-coated monolith prepared in Chapter 6 in the mixed lubrication regime, indicating other parameter in regard to the interaction between surfaces were needed for description of a master curve since adhesion was suppressed probably because of the improvement of wettability for lubricants against the aluminum surface.[19]

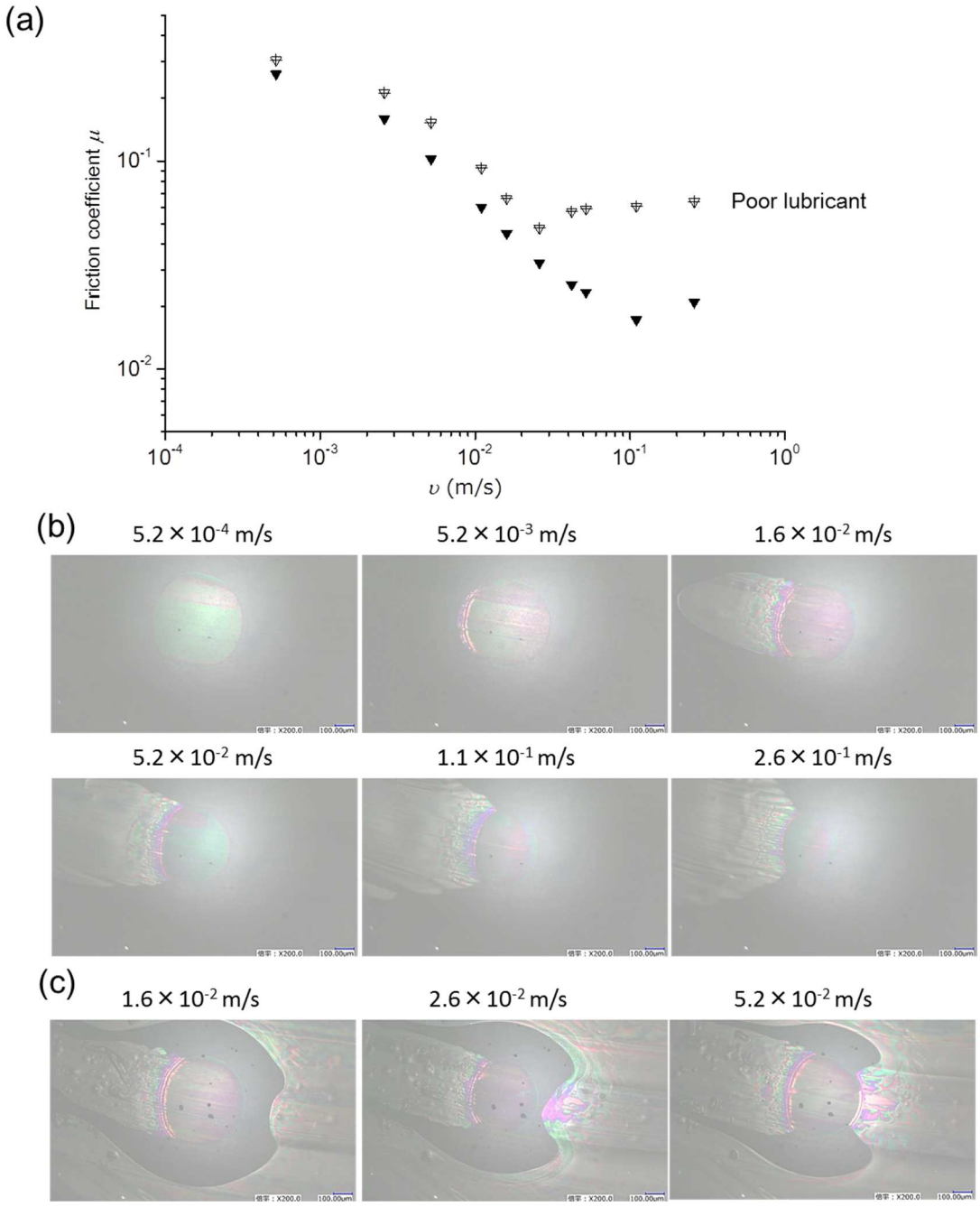

Figure 7-7. (a) Plots of friction coefficient μ against sliding velocity for Al-coated monoliths against the Cr-SiO_2-coated lens with PAO10 (open triangles) and poor lubricant (open triangles with cross) at 1 N, (b) microscopic images of sliding surface with PAO10 and (c) with poor lubricants.

Monoliths were expected forming of fluid film in poor lubrication by exuding lubricants.

Accordingly, the frictional properties with poor lubrication were performed. Figure 7-7(a) shows μ against sliding velocity for Al-coated monoliths versus a Cr-SiO_2-coated lens lubricated with PAO10 and poor lubricant at 1 N. In small sliding velocity, μ with poor lubrication was consistent with immersed lubrication, whereas, μ increased in the large sliding velocity. Figure 7-7(b) shows sliding surfaces of an Al-coated monolith with immersed PAO 10 at 1 N. Circular contact regions and colored interference patterns were observed. Contact areas decreased with the increase of sliding velocity. Central colors were changed from green to red and green again with the increase of sliding velocity, indicating film thickness increased. Cavitation phenomenon was also observed in the backside of the lens toward the sliding direction of the monolith, and larger with the increase of velocity. Figure 7-7(c) shows sliding surfaces with poor lubricant. Bright grey and colored regions were also observed, in which the lubricant was shortage. It should be notice that at lubricants were existed around contact region and frictional behavior was similar as immersed lubricant at small sliding velocity, indicating the lubricant was immersed. On the other hand, at large velocity, lubricant was shortage in front of the contact region, resulting to the increase of μ.

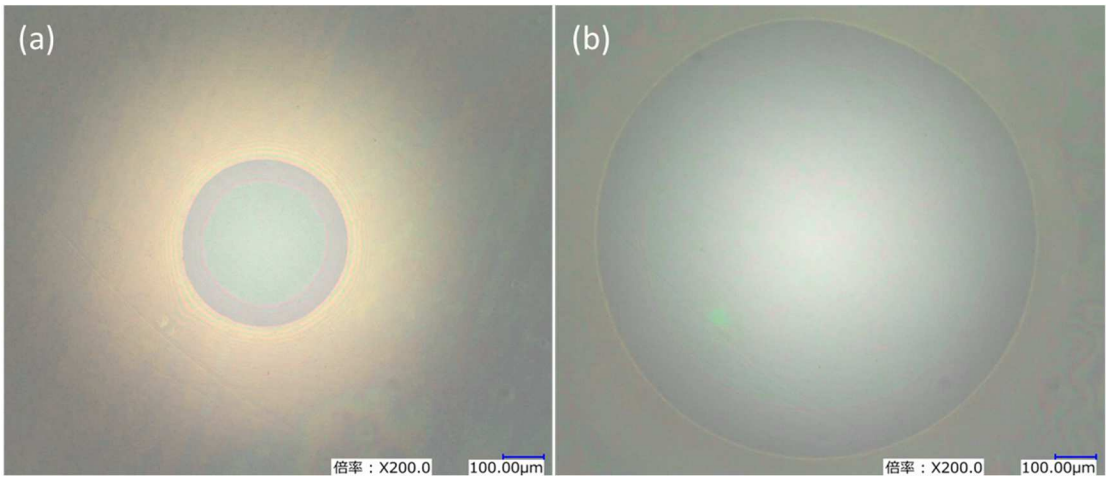

Figure 7-8. Microscopic images of indentation measurement of a monolith with PAO10 in thickness (a) at 0.1 N and (b) 4 N. PAO10 was filled in pores of the monolith.

Subsequently, in order to observe the exuding phenomenon from the pores, indentation test was performed. Figure 7-8 shows images of contact surface and fluids during a measurement of monolith with PAO10. Circular contact regions colored green and immersed regions colored dark were observed at both 0.1 N and 4 N. Furthermore, exuding behavior of lubricant was observed outside of dark regions. Volume of exuding lubricant estimated geometrically at 0.1 N and 4 N was 2.9×10^4 and 1.3×10^6 μm^3, respectively, which at 4 N was about 45 times larger. The ratio of lubricant volume to the deformation volume of monoliths at 0.1 N and 4 N was 80% and 61%, respectively, which were roughly consistent with the porosity of monoliths. From these results, lubricant was exuded by deformation of monoliths.

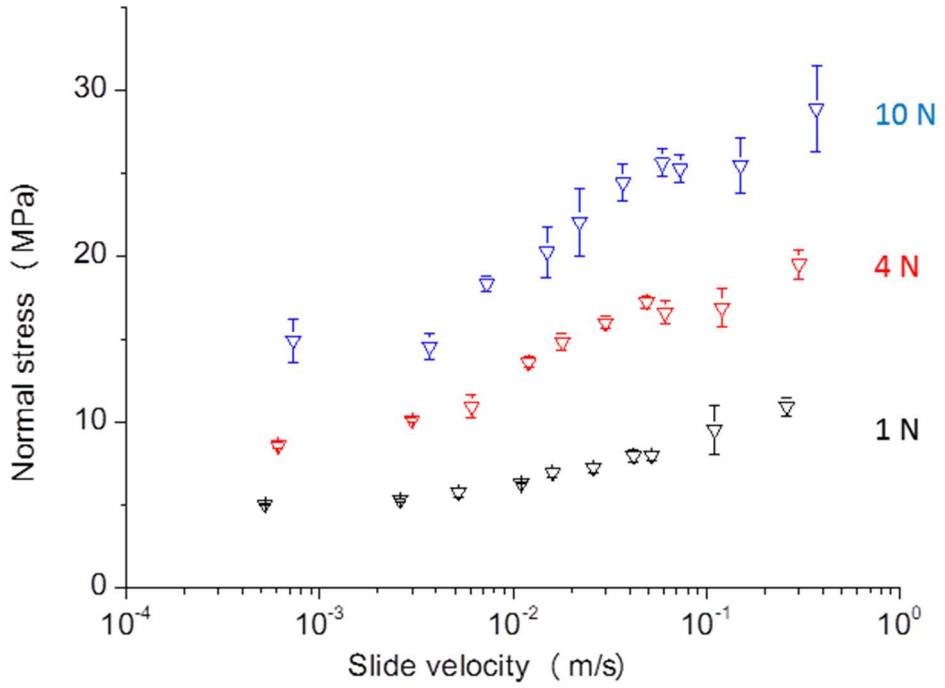

Figure 7-9. Normal stress against sliding velocity of a monolith with 170 μm in thickness prepared at 130°C with PAO10. Standard deviation was given by error bars.

Subsequently, averaged normal stress and film thickness were estimated. Figure 7-9 shows normal stress against sliding velocity of a monolith with 170 μm in thickness. Normal stress increased with the increase of sliding velocity due to the increase of hydrodynamic pressure. In addition, normal stress of the thin monolith drastically increased by loads than that of the thick monolith, indicating the load was supported by a substrate under the monolith.

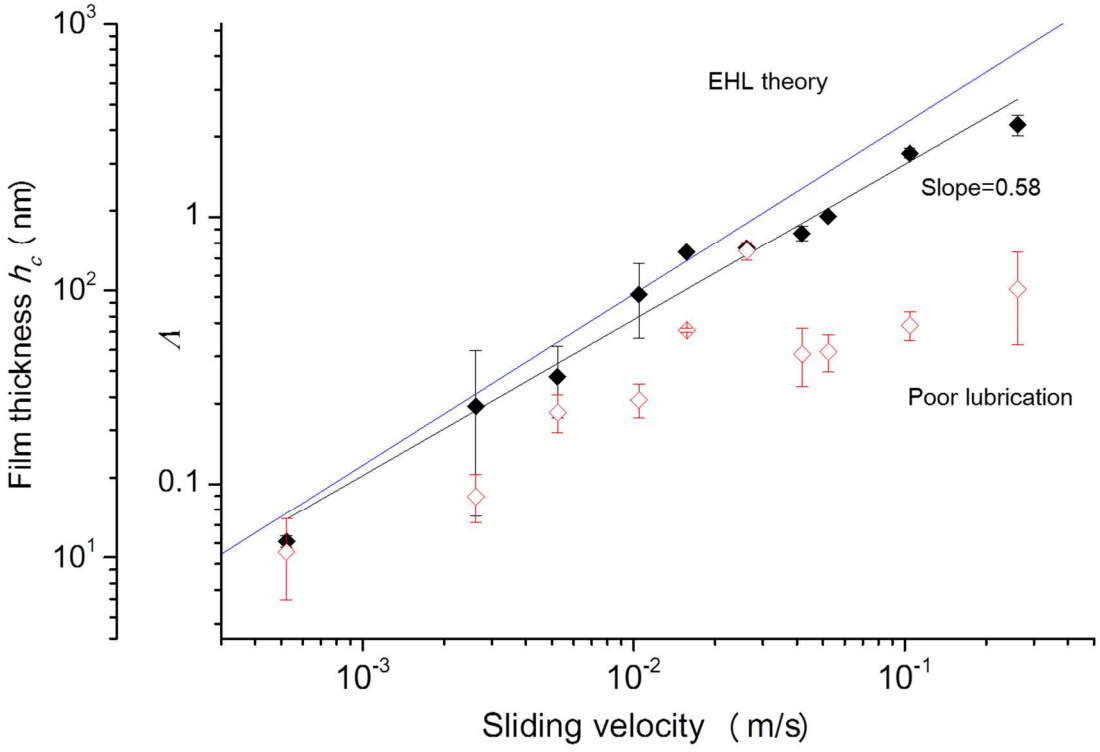

Figure 7-10. Double logarithmic plots of averaged central film thickness (h_c), film thickness parameter (Λ) and standard deviation (error bars) against sliding velocity with PAO10 (closed diamonds), fitting line (black line) and with poor lubrication (open diamonds) at 1 N. Blue line was prediction by EHL theory.

Figure 7-10 shows central film thickness (h_c) and film thickness parameter (Λ) against sliding velocity with PAO10 and poor lubricants, and EHL theory estimated from Hamrock and Dowson's isoviscous-elastic equation shown as below,[20]

$$h_c = 3.3R\overline{U}^{0.64}\overline{W}^{-0.22} \quad (7-1)$$

$$\overline{U} = \frac{\eta_0 v}{ER} \quad (7-2)$$

$$\overline{W} = \frac{F}{ER^2} \quad (7-3)$$

$$\frac{2}{E} = \frac{1-\nu_1^2}{E_1} + \frac{1-\nu_2^2}{E_2} \quad (7-4)$$

where, v was sliding velocity, F was normal load, E was equivalent elastic modulus shown as equation (7-4), R was equivalent radius and η_0 was viscosity of lubricant. E_1, E_2, ν_1 and ν_2 were elastic modulus and poisson's ratio of opposite materials, respectively. The modulus of a glass lens was assumed 80 GPa. Poisson's ratio of a glass lens and a monolith was assumed 0.23 and 0.3, respectively. Apparent elastic modulus of the monolith with PAO10 was estimated 0.42 GPa by contact radius at 1 N (250 μm) and Hertzian contact equation as shown below,

$$a^3 = \frac{3}{2}\frac{FR}{E} \quad (7-5)$$

where, a was static contact radius. h_c was estimated from the averaged hue value of central 75 × 75 pixels (114 × 114 μm) in microscopic images. In immersed lubrication, film thickness increased with the increase of velocity with 0.58 of a slope, which was almost consistent with the EHL theory.[21, 22]

Subsequently, with poor lubrication, film thickness drastically decreased when sliding speed was more than 3×10^{-2} m/s, which was consistent with the speed that surrounding contact region was shortage of fluid in Figure 7-7(c), indicating fluid film was destructed by shortage of lubricant.

Subsequently, film thickness parameter (Λ) was defined as below,

$$\Lambda = \frac{h_{min}}{\sqrt{R_{q1}^2 + R_{q2}^2}} \quad (7-6)$$

where, h_{min} was minimum film thickness, R_{q1}, R_{q2} were root-mean-square roughness of two surfaces. R_q of a monolith and Cr-SiO_2 coated lens was 180 nm and 9 nm, respectively. The h_{min} was approximated estimated h_c, which was rather larger than h_{min}. Film thickness parameter Λ at 1.1×10^{-1} m/s of sliding velocity in EHL transition regime was $\Lambda = 1.7$, which was much smaller than generally reported range of 3–10,[23] suggesting less influence of roughness derived from softness of the monolith.

7-4. Conclusion

We demonstrated observation of sliding surface of monoliths by optical interferometry technique for the first time in success. Film thickness was consistent with EHL theory. Film thickness parameter at EHL transition regime was much smaller than expected, suggesting less influence of roughness derived from softness of the monolith. In poor lubrication, shortage of lubricant on sliding region caused decrease of film thickness, resulting in the increase of friction coefficient. On the other hands, monoliths were suppressed shortage of lubricants by exuding, hence, monoliths had potential to maintain soft-EHL in spite of with poor lubrication by controlling exude and flowing of lubricant.

7-5. References

1. T. Ibatan, M. S. Uddin, M. A. K. Chowdhury. *Surf. Coat. Technol.* **2015**, *272*, 102–120.

2. L. Mourier, D. Mazuyer, A. A. Lubrecht, C. Donnet. *Tribol. Int.* **2006**, *39*, 1745–1756.

3. L. Křupka, R. Poliščuk, M. Hartl. *Tribol. Int.* **2009**, *42*, 535–541.

4. I. Křupka, M. Hartl. *Tribol. Int.* **2007**, *40*, 1100–1110.

5. X. Wang, W. Liu, F. Zhou, D. Zhu. *Tribol. Int.* **2009**, *42*, 1118–1123.

6. D. Gropper, L. Wang, T. J. Harvey. *Tribol. Int.* **2016**, *94*, 509–529.

7. I. Křupka, M. Vrbka, M. Hartl. *Tribol. Int.* **2008**, *41*, 1063–1073.

8. B. Su, L. Huang, W. Huang, X. Wang. *Tribol. Int.* **2018**, *119*, 521–530.

9. W. Huang, L. Jiang, C. Zhou, X. Wang. *Tribol. Int.* **2012**, *52*, 87–93.

10. Y. H. Liu, X. K. Wang, J. B. Luo, X. C. Lu. *Appl. Surf. Sci.* **2009**, *255*, 9430–9438.

11. W. Huang, L. Jiang, C. Zhou, X. Wang. *Tribol. Int.* **2012**, *52*, 87–93.

12. A. Shinkarenko, Y. Kligerman, I. Etsion. *Tribol. Lett.* **2009**, *36*, 95–103.

13. F. Shi, R. F. Salant. *J. Tribol*. **2000**, *122*, 308–316.

14. B. Su, L. Huang, W. Huang, X. Wang. *Tribol. Int.* **2017**, *109*, 86–96.

15. I. Křupka, M. Hartl. *Tribol. Int.* **2007**, *40*, 1553–1560.

16. R. Gohar, A. Cameron. *Nature* **1963**, *200*, 458.

17. K. Sakakibara, H. Kagata, N. Ishizuka, T. Sato, Y. Tsujii. *J. Mater. Chem. A* **2017**, *5*, 6866–6873.

18. M. Kobayashi, H. Tanaka, M. Minn, J. Sugimura, A. Takahara. *ACS Appl. Mater. Interfaces* **2014**, *6*, 20365–20371.

19. J. H. H. Bongaerts, K. Fourtouni, J. R. Stokes. *Tribol. Int.* **2007**, *40*, 1531–1542.

20. B. J. Hamrock, D. Dowson. *J. Lubr. Technol.* **1977**, *99*, 264–275.

21. J. De Vicente, J. R. Stokes, H. A. Spikes. *Tribol. Lett.* **2005**, *20*, 273–286.

22. N. Marx, J. Guegan, H. A. Spikes. *Tribol. Int.* **2016**, *99*, 267–277.

23. B. J. Hamrock, S. R. Schmid, B. O. Jacobson. *Fundamentals of fluid film lubrication. CRC press* **2004**.

Chapter 8

Understanding of Frictional Property and Wearing Control of Monolith-coated Sliding Bearings

8-1. Introduction

Sliding machine elements, which were exhibited basic tribological performance such as high strength, wear resistance and control of friction were widely used in various industrial machine systems, while they were required miniaturization and weight saving to achieve reduction of environmental load and energy saving. Accordingly improvement of tribological properties was required under sliding conditions such as use of low viscosity lubricants, loading large surface pressure, and small sliding velocity. However, thus severe sliding conditions caused seizure[1–3] i.e. critical damage of sliding materials derived from sudden increase of friction force, temperature and wear in the mixed and boundary lubrication. To overcome this problem, control of running-in process, which was the process that frictional behavior was stabilized by sliding surfaces, was proposed.[4-8]

Surface texturing such as micrometer-scale of dimples and groove patterns was one of the effective methods for control running-in process and expected suppression of boundary lubrication by reserving and flow control of lubricants on the sliding surface.[9–11]

Coating of soft materials such as aluminum alloy and polymer resin was also reported, which was expected the decrease of contact pressure.[12, 13] Among them, polymer resin was focused on as tribomaterials with an advantage of lightweight, formability and tribological properties such as resiliency and followability for various sliding conditions. In previous chapters, we revealed a monolith film on a substrate was exhibited superior friction properties derived from holding and

exuding of lubricant, soft-EHL effects, and suppression of ploughing.

In Chapter 8, a monolith film was applied toward sliding machine elements. First of all, a monolith-coated sliding bearing with a monolith film embedded in micrometer-scale-depth of aluminum alloy grooves was prepared. It should be noticed that grooves were utilized as embedding space of the monolith for the improvement of wear resistance but not as surface texturing because the monolith itself was some kind of surface texturing with the advantage of reserving and exuding of lubricants derived from soft materials with connected pores. In the second, tribological properties including running-in process and wear resistance was evaluated by using the apparatus which was closely correlated to actual use.

8-2. Experimental Section

8-2-1. Materials

1,3-Bis(*N,N'*-diglycidylaminoethyl)cyclohexane (TETRAD-C) (98%, Mitsubishi Gas Chemical Company, Inc., Japan), bis(4-aminocyclohexyl)methane (BACM) (mixture of isomers, 97%, Wako, Japan), Polyethylene glycol 200 (PEG200) (averaged molecular weight: 190–210, Kishida Chemical Co., Ltd., Japan), 3-aminopropyltriethoxysilane (98%, Nacalai Tesque Inc., Japan), ammonia solution (28%, Nacalai Tesque Inc., Japan), acetone (99.5%, Super Dehydrated, Wako, Japan), methanol (1st grade, Wako), ethanol (99.5%, Wako) and AEROSIL 130 (Hydrophilic fumed silica, Evonik Industries), actually used oil consisted of base oil and viscosity index improver (10.37 mm^2/s at 60 °C) and a ring specimens S55C (Vickers Hardness 222, R_a = 0.036 μm, diameter D=44 mm, width 15.2 mm) were used as received. A grooved bearing specimen (pitch of groove 300 μm, depth of groove 12 μm, inside diameter D=44 mm, back metal width 13.4 mm, thickness 1.497 mm, TAIHO KOGYO CO.,LTD.) (Figure 8-1) were washed with hexane, followed by acetone by sonication for 10 minutes.

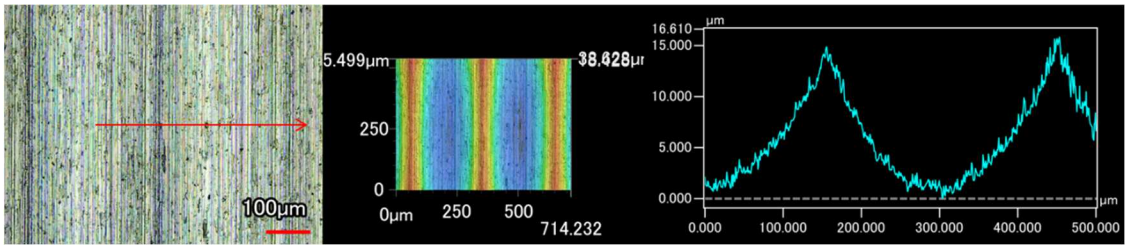

Figure 8-1. Laser microscopic image and surface roughness profiles of a grooved bearing specimen.

8-2-2. Preparation of a monolith-coated bearing

Monolith-coated bearing specimen

A grooved bearing specimen was immersed in an ethanol solution of 3-aminopropyltriethoxysilane (1 wt%) and 28% aqueous NH_3 (10 wt%) for 15 h at room temperature, then, washed with ethanol. The monomer mixture of AEROSIL 130 (1.394 g, 2.5 wt%), PEG200 (40 g), BACM (5.75 g, 1 eq.) and TETRAD-C (10 g, 1 eq.) was coated on a grooved bearing specimen. The bearing with the mixture was heated at 110 °C for 1 h in an oven, heated at 180 °C for 30 minutes, immersed in methanol overnight and dried under vacuum, yielding a monolith with a thickness of around 250 μm. The surface monolith was polished to the top of grooves with an abrasive paper #2000 in water, yielding a monolith-coated bearing specimen. The monolith-coated bearing specimen was immersed in the lubricant under vacuum overnight for tribological measurements.

8-2-3. Characterization

Field emission scanning electron microscopy (FE-SEM) observations were carried out on a JEOL JSM-6700F SEM operated at 1.5 kV. During the preparation of samples for cross-sectional observations, the samples were fractured in liquid nitrogen to obtain fresh cross sections. Prior to SEM observations, the samples were sputter-coated with a thin layer of platinum to enhance their conductivity (Hitachi ion sputter E-1010); sputter time: 20 s; coat thickness: ca. 5 nm.

8-2-4. Measurements

Test apparatus for tribological measurements

Tribological properties of sliding bearings were evaluated by using a test apparatus shown in Figure 8-2, which was prepared by Honda et al. at university of Fukui for the purpose of understanding tribological and seizure mechanism under actual conditions of industrial automobile systems.

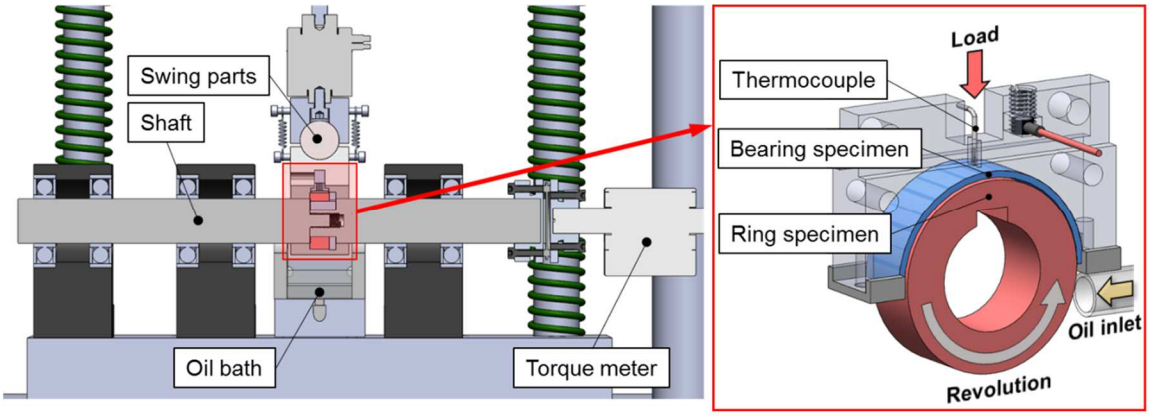

Figure 8-2. Schematic illustration of a test apparatus for tribological measurements of a bearing specimen.

Load (F) was applied by using a hydraulic pump from top of a bearing mount equipped with a swing part. Friction torque (T_q) and temperature at center backside of a bearing specimen were measured during rotation of a ring. Oil was continued pouring to a ring specimen from an oil inlet which was connected to an oil tank maintained at 60 °C. Oil was circulated through a magnetic filter to remove wear particles. Friction coefficient (μ) was defined as $2T_q/DF$. The F was averaged in the regime of final 100 m of sliding distance at each step.

Tribological measurement by decreasing sliding velocity in a stepwise

A ring specimen was rotated 2000 m of sliding distance at 6 m/s of sliding velocity (v) at 100 N of load, followed by rotating 500 m each at 6.0-0.5 m/s in a stepwise at 500 N.

Tribological measurement by increasing loading in a stepwise

The ring specimen was rotated 2000 m of sliding distance at 2 m/s of v at 100 N, followed by rotating 500 m each at 500, 1000, 1500 and 2000 N in stepwise, finally rotating additional 1000 m after stopped pouring the oil.

8-3. Results and discussion

8-3-1. Preparation of a monolith-coated bearing

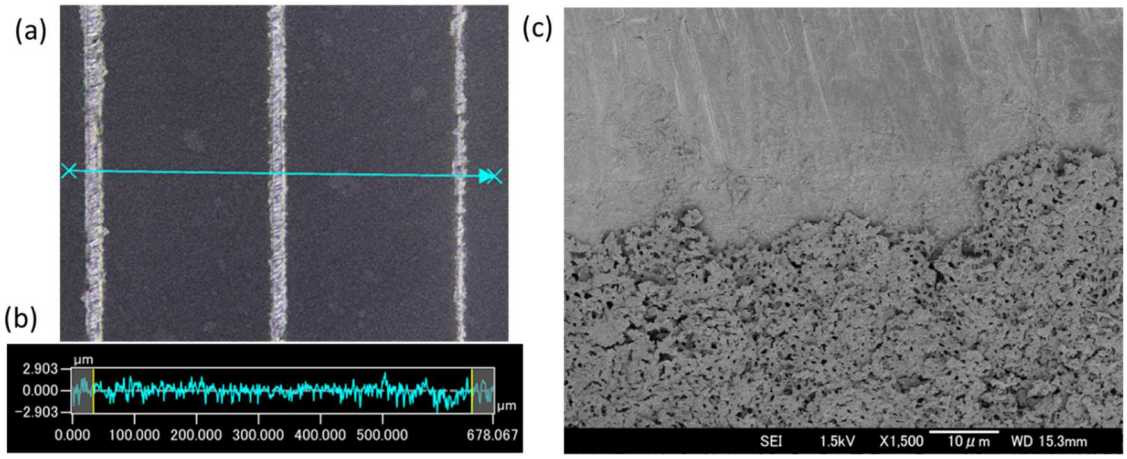

Figure 8-3. (a) Laser microscopic image, (b) roughness profile and (c) FE-SEM image of a surface of monolith-coated bearing. R_a = 0.58 μm.

A monolith-coated sliding bearing with a monolith film embedded in 12 μm depth of aluminum alloy grooves was prepared. Figure 8-3 shows laser microscopic image, roughness profile and FE-SEM image of a surface of monolith-coated bearing. Monoliths were embedded in grooves and top-surface of the monolith-coated bearing was flat without steps between the monolith and top of

the groove (Figure 8-3(a) and (b)). Pores and monolith network were observed with skinless (Figure 8-3(c)). In conclusion, a monolith-coated bearing specimen was prepared in success.

8-3-2. Tribological properties of a monolith-coated bearing

Figure 8-4 shows friction coefficient μ and back steel temperature for a grooved bearing and a monolith-coated bearing measured by increasing load in a stepwise at 2 m/s of v. In the range of 0–2000 m of sliding distance at 100 N, the back steel temperature of both bearings was converged to 60 °C which was oil temperature, indicating the friction heat was less generated. The μ of the monolith-coated bearing decreased with sliding distance, indicating running-in process was smoothly. In the range of 2000–4000 m of sliding distance at 500–2000 N, back metal temperature of the monolith-coated bearing was gradually increased with loading and the peak value was smaller than that of the grooved bearing at the moment of additional loading. While the μ of both bearing decreased with loading, peak value of μ was also small in the case of the monolith-coated bearing at the moment of additional loading. In the range from 4000 m in which supplying of oil was stopped, the μ was maintained still lower without seizure.

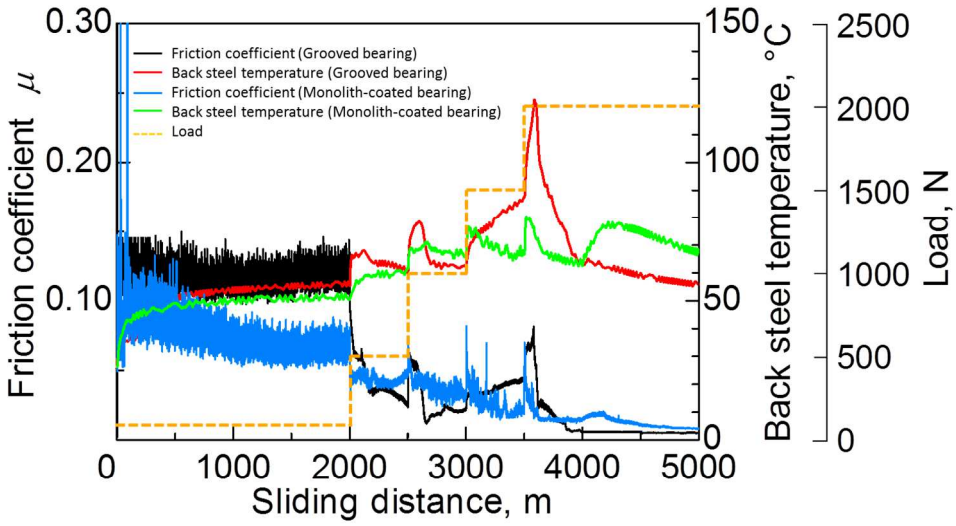

Figure 8-4. Friction coefficient μ and back steel temperature for a grooved bearing and a monolith-coated bearing measured by increasing load in a stepwise at 2 m/s of *v*.

Subsequently, Figure 8-5 shows μ and back steel temperature for a grooved bearing and a monolith-coated bearing measured by decreasing *v* in a stepwise at 100 N and 500 N. In the case of a monolith-coated bearing, the μ decreased gradually in the range of 0–2000 m of sliding distance at 100 N, indicating the running-in process of wearing was occurred smoothly. In the range of 2000–7000 m at 500 N, the μ and back steel temperature decreased with the decrease of sliding velocity, followed by increased in 7000–8000 m.

In the case of a grooved bearing, the μ was smaller than that of the monolith-coated bearing at first 2000 m at 100 N. At 2000, 5500, 7000, and 7500 m, the μ and temperature rapidly increased by decreasing sliding velocity, indicating sudden contact and wear of materials were occurred.

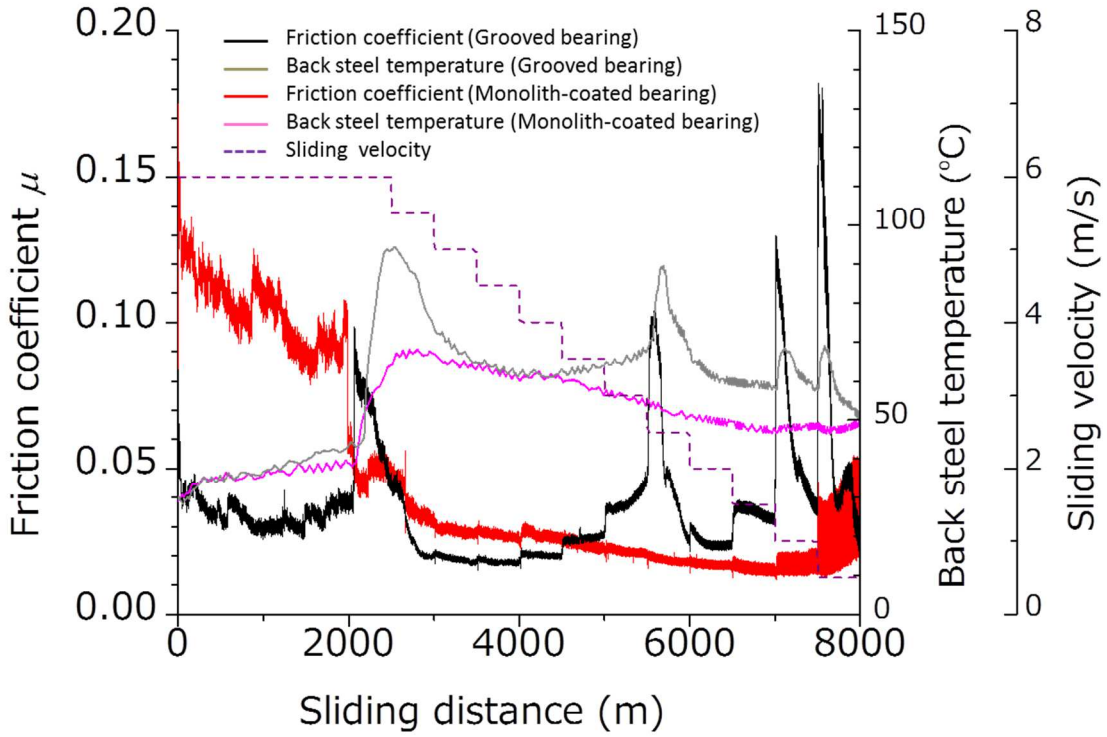

Figure 8-5. Friction coefficient μ and back steel temperature for a grooved bearing and a monolith-coated bearing measured by decreasing sliding velocity v 6–0.5 m/s in a stepwise at 100 N and 500 N.

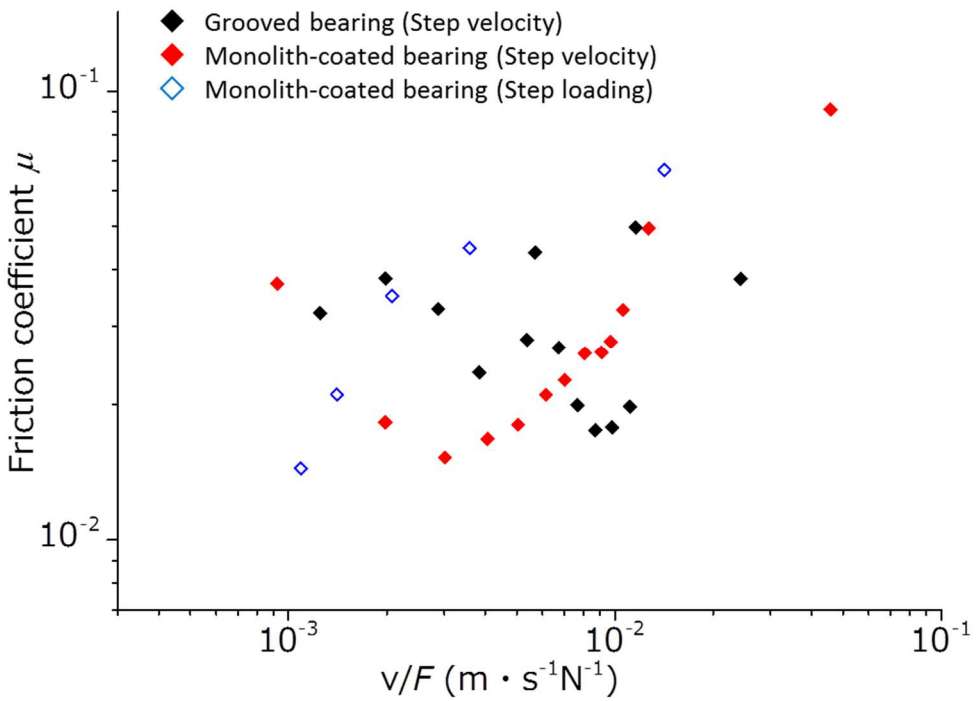

Figure 8-6. Plots of friction coefficient μ against parameter of *v/F* for a grooved bearing and monolith-coated bearings.

Figure 8-6 shows plots of μ against parameter of *v/F* for a grooved bearing and monolith-coated bearings. The μ of the grooved bearing was exhibited unstable behavior because the sliding surface was worn severely and irregularly due to the sudden contact at some steps. Subsequently, the monolith-coated bearings were described smooth Stribeck curve in the hydrodynamic and mixed lubrication regime because wear of the sliding surface was gradually and smoothly during the measurements. In addition, low μ was attained in the regime of mixed lubrication without seizure. On the other hand, curves in the hydrodynamic lubrication regime was shifted left with the increase of loading probably because sliding surfaces were contacted and actual normal stress was become smaller than that of the grooved bearing by the support of the monolith. Similarly, curves with step velocity and step loading measurement were not overlapped probably because of the difference of loading condition and running-in process.

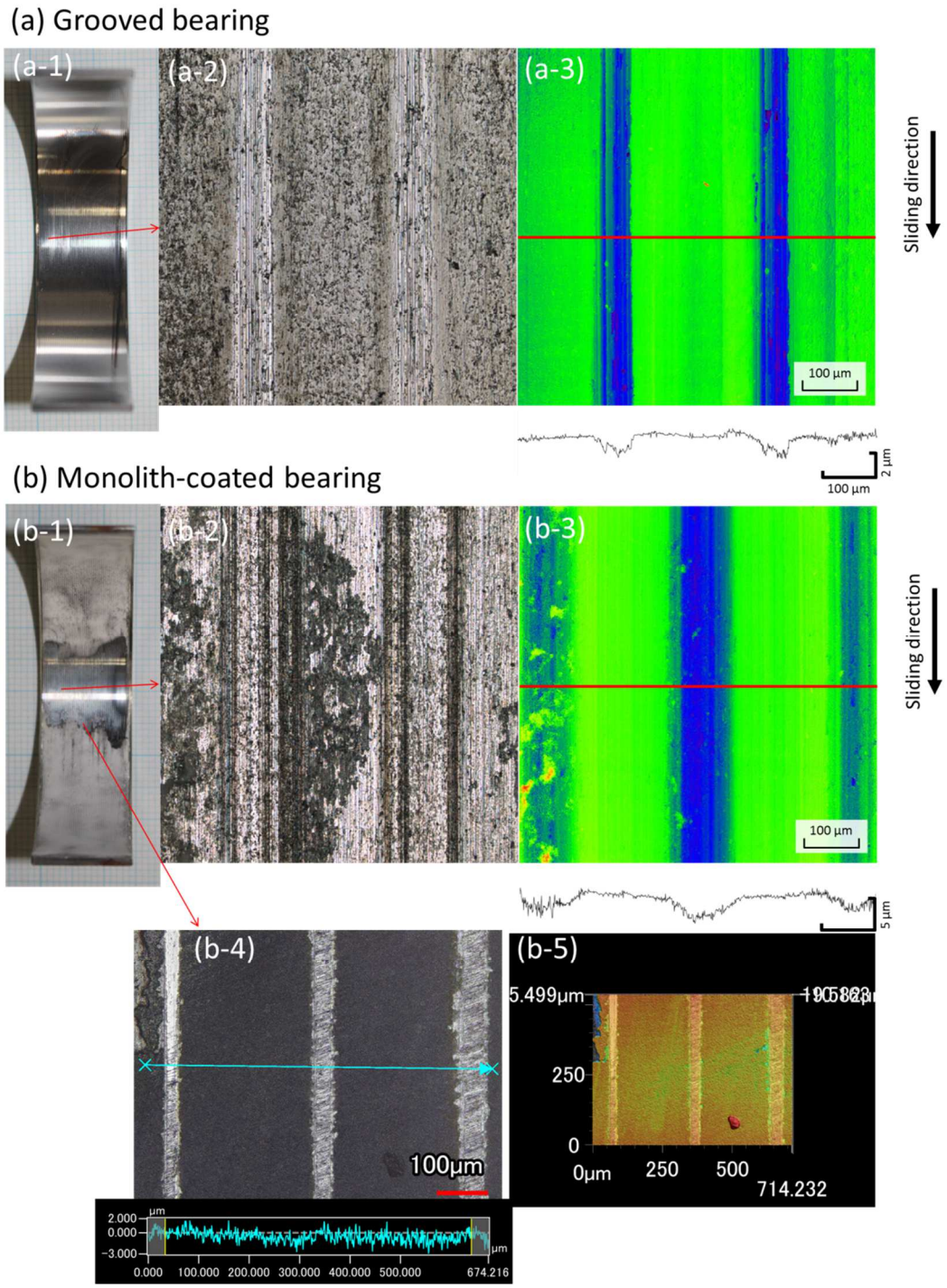

Figure 8-7. Appearance, laser microscopic images and surface roughness profiles of (a) a grooved bearing and (b) a monolith-coated bearing washed with hexane after tribological measurement by increasing loading in a stepwise. Arrows show the regime of observation.

Figure 8-7 shows appearance, laser microscopic images of a grooved bearing and a monolith-coated bearing washed with hexane after tribological measurement by increasing loading in a stepwise. Top of groove was worn out with small roughness, indicating running-in process was proceeded in both bearings. The monolith was destructed by cohesive and interfacial failure in the load center regime of bearing, whereas abrasion failure in the far from the load center, indicating the monolith was gradually destructed critically with the loading, nevertheless residual was effective for the tribological properties.

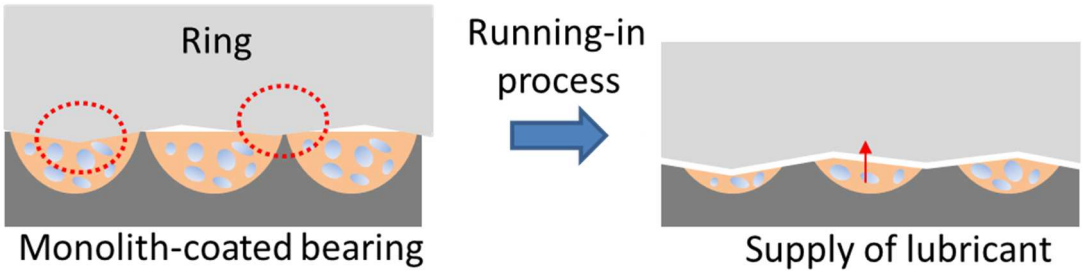

Figure 8-8. Schematic illustration of the proposed running-in process and suppression of seizure mechanism of the monolith-coated bearing.

Figure 8-8 shows schematic illustration of the proposed effective running-in process and suppression of seizure mechanism of the monolith-coated bearing. At start-up of sliding, tops of grooves were contacted derived from small roughness of two faces, and at the same time, a monolith embedded in the grooves was also supported the load and lubricant was supplied to the sliding surface, resulting to the decrease of surface pressure of contact. Furthermore, severe wear by sudden contact and the increase of frictional force was suppressed by the supply of lubricant to the sliding surface derived from the deformation of the monolith. In conclusion, effective running-in process

and suppression of seizure was revealed by applying a monolith-coated sliding bearing.

8-4. Conclusion

A monolith-coated sliding bearing with a monolith embedded in micrometer-scale-depth of grooves, was exhibited excellent tribological properties including smooth and effective transfer to running-in process and impact mitigation derived from suppression of unexpected increase of frictional force, temperature, and wear. In conclusion, we revealed the monolith films combined surface grooving of substrates had the potential for practical realization of sliding machine elements.

8-5. References

1. E. Rabinowicz. *Wear* **1973**, *25*, 357–363.
2. Q. Wang. *Wear* **1997**, *210*, 8–16.
3. U. Pettersson, S. Jacobson. *Tribol. Int*. **2003**, *36*, 857–864.
4. A. Hase, H. Mishina, M. Wada. *Wear* **2016**, *346*, 132–139.
5. W. Wang, P. L. Wong, Z. Zhang. *Wear* **2000**, *244*, 140–146.
6. W. Wang, P. L. Wong, F. Guo. *Wear* **2004**, *257*, 823–832.
7. S. Akbarzadeh, M. M. Khonsari. *J. Tribol.* **2010**, *132*, 032102.
8. D. E. Sander, H. Allmaier, H. H. Priebsch, M. Witt, A. Skiadas. *Tribol. Int.* **2016**, *96*, 173–183.
9. X. Wang, K. Adachi, K. Otsuka, K. Kato. *Appl. Surf. Sci.* **2006**, *253*, 1282–1286.
10. W. Koszela, P. Pawlus, L. Galda. *Wear* **2007**, *263*, 1585–1592.
11. W. Tang, Y. Zhou, H. Zhu, H. Yang, H. *Appl. Surf. Sci.* **2013**, *273*, 199–204.
12. A. Takami, T. Honda, E. Yasuda. *Trans. Soc. Automot. Eng. Jpn.* **2018**, *49*, 926–931.
13. M. Repka, N. Dörr, J. Brenner, C. Gabler, C. McAleese, O. Ishigo, M. Koshima. *Tribol. Int.* **2017**, *109*, 519–528.

Summary

In Chapter 1, the background, purpose, and outline of this thesis were described.

This thesis is divided into two parts. In Part 1 (Chapters 2, 3, 4, and 5), a BC gel was utilized as a well-defined fine network. In Part 2 (Chapters 6, 7, and 8), an epoxy resin-based monolith was utilized as a well-defined fine network.

In Chapter 2, resin composites with a well-defined BC nanofiber network were prepared by *in situ* solvent exchange and polymerization. In this method, the water in BC hydrogels was exchanged to MMA via THF, following which free radical polymerization of the MMA was performed using an initiator. The CLSM images of the BC gels and BC/PMMA composites indicated that the networks in the latter maintained a homogenous distribution. Nano-indentation experiments revealed high mechanical properties, which were predicted theoretically from the elastic modulus of BC. The BC nanofiber network exhibited stretch-dominated deformation and effective load transfer. These were derived from the reinforcement of the fine BC network as well as the lateral reinforcement of the matrix, despite the weak interfacial interaction between BC and PMMA due to low affinity.

In Chapter 3, BC-reinforced elastomers with a well-defined nanofiber network were prepared by *in situ* solvent exchange and polymerization. The obtained elastomeric composite showed good mechanical properties even with a small volume fraction of BC. It was characterized by an exceptionally high fracture strain, good stretchability, and effective strain hardening with necking during the tensile test. CLSM observations confirmed that a well-defined nanofiber network of the original BC was successfully embedded in the PEA matrix and that the BC nanofibers were uniformly oriented in the stretched sample. These remarkable mechanical and structural features could be ascribed to the rigidity and flexibility of the BC nanofibers, which led to the formation of a percolated structure of fully aligned nanofibers by elongation. This process can be applied to various

materials, demonstrating the reinforcement capability for composites with a BC nanofiber network.

In Chapter 4, we demonstrated the preparation of hybrid gels with concentrated polymer brush-grafted BC and bottle-brush networks by the surface-initiated ATRP of PEGMA. The hybrid gel was remarkably reinforced by the BC nanofiber network depending on the BC content. The friction coefficient for the thus-obtained gels was of the order of 10^{-4} in magnitude, suggesting that the adhesion force was effectively suppressed by the bottle-brush network and immobilized lubrication film derived from the CPB. In addition, the hybrid gels exhibited superior wear resiliency against the thin CPB on a rigid substrate, demonstrating their potential as a tribomaterial. Rheometer measurements suggested that the friction force at the shoulder region in the Stribeck curve was derived from the adhesion force and elastic modulus of the gel. From these results, we developed a general approach for tribomaterials by classifying the networks as a mechanically reinforced network and low frictional network with small adhesion force.

In Chapter 5, we revealed the systematic relationship between the deformation behavior of the BC nanofiber network in matrices and the mechanical properties of the composites. The composites were reinforced by suppressing the deformation of the BC nanofiber network, depending on the elasticity of the surrounding elastic matrices. This systematic understanding will aid in the design of functionalized composites embedded with a network structure.

In Chapter 6, we demonstrated a new approach to prepare monolith films uniformly on flat and curved substrates by dip coating. Films of various thicknesses were obtained by controlling the viscosity of the polymerization mixture during dip coating and heating. The monolith film with lubricants was apparently reinforced by a rigid substrate and resistance of liquid flow, resulting in the suppression of deformation. The friction coefficient of the monoliths was described as $\eta^{0.5} v F^{0.4}$ (thickness)$^{-0.6}$ (pore size)$^{-1.2}$. μ decreased with increasing normal loads and decreasing thickness and pore sizes. It was also proportional to the 0.5^{th} power of the viscosity of the lubricant, indicating that

the mechanical properties of the monolith, including the influence of a rigid substrate and flow behaviors such as exuding, paths, and resistance to flow in pores, were affected by the frictional properties.

In Chapter 7, we analyzed the sliding surface of monoliths by optical interferometry. The thickness of the lubricant film was consistent with the EHL theory. The film thickness at the EHL transition regime was much smaller than expected, suggesting a lesser influence of the roughness, due to the softness of the monolith. Under poor lubrication, a shortage of lubricant on the sliding region caused a decrease in the film thickness, thereby increasing the friction coefficient. On the other hand, the monoliths suppressed the shortage of lubricants by exuding; hence, they can be used to maintain a soft EHL despite poor lubrication by controlling the exuding and flowing of the lubricant.

In Chapter 8, the monolith film was applied toward sliding machine elements. A monolith-coated sliding bearing, of which a monolith was embedded in micrometer-scale-depth of grooves, was exhibited excellent tribological properties including smooth and effective transfer of running-in process and impact mitigation derived from suppression of unexpected increase of frictional force, temperature, and wear. In conclusion, we revealed the monolith films combined surface grooving of substrates had the potential for practical realization of sliding machine elements.

List of Publications

Chapter 2.

(1) Effective reinforcement with well-defined bacterial cellulose nanofiber network for poly(methyl methacrylate) composites

Y. Shimizu, K. Sakakibara, S. Akimoto, Y. Tsujii. *Biomacromolecules.* submitted.

Chapter 3.

(2) Strain hardening of highly stretchable elastomeric composites reinforced with well-defined nanofiber network of bacterial cellulose

Y. Shimizu, K. Sakakibara, Y. Tsujii. *J. Fiber Sci. Technol.* **2018**, *74*, 17–23.

Chapter 4.

(3) Excellent lubrication and resiliency of bottle-brush typed hybrid gel reinforced with well-defined nanofiber network of bacterial cellulose

Y. Shimizu, K. Sakakibara, Y. Tsujii. to be submitted.

Chapter 5.

(4) Understanding of mechanical functionality of well-defined bacterial cellulose nanofiber network embedded in matrices

Y. Shimizu, K. Sakakibara, Y. Tsujii. to be submitted.

Chapter 6.

(5) Preparation, structure and tribological property of epoxy resin-based monolith films

Y. Shimizu, K. Sakakibara, S. Yasuda, Y. Tsujii. *Soft matter.* submitted.

Chapter 7.

(6) Effective lubrication of epoxy resin-based monoliths by simultaneous measurement of optical interferometry

Y. Shimizu, K. Sakakibara, Y. Tsujii. to be submitted.

Chapter 8.

(7) Understanding of frictional property and wearing control of monolith-coated sliding bearings

Y. Shimizu, M. Tsubota, K. Sakakibara, T. Honda, Y. Tsujii. to be submitted.

Other Publications

(8) Photoinduced Group Transfer Radical Addition of Carbamotelluroates to Acetylenes.

S. Fujiwara, Y. Shimizu, T. Shin-ike, N. Kambe. *Org. Lett.* **2001**, *3*, 2085–2088.

(9) N-carbonylation of lithium azaenolates of amides, formamides, ureas, and carbamates with carbon monoxide mediated by selenium.

S. Fujiwara, K. Okada, Y. Shikano, Y. Shimizu, T. Shin-ike, J. Terao, N. Kambe, N. Sonoda. *J. Org. Chem.* **2007**, *72*, 273–276.

(10) A new entry to α-alkylidene-β-lactams by 4-exo-dig cyclization of carbamoyl radicals.

S. Fujiwara, Y. Shimizu, Y. Imahori, M. Toyofuku, T. Shin-ike, N. Kambe. *Tetrahedron Lett.* **2009**, *50*, 3628–3630.

(11) Fabrication of Well-Dispersed Cellulose Nanofiber / Polymer Nanocomposite Materials.

K. Sakakibara, Y. Shimizu, Y Tsujii. *Cellulose Commun.* **2017**, *24*, 8–12.

Acknowledgements

The present investigations were carried out under the direction of Prof. Yoshinobu Tsujii at the Institute for Chemical Research (ICR), Kyoto University in the period from April 2015 to March 2019 as a student for doctoral course.

I would like to express my sincerest gratitude to Prof. Yoshinobu Tsujii for his kind guidance, valuable suggestions and warm encouragement throughout this work. I would like to thank Assist. Prof. Keita Sakakibara for his constructive guidance, valuable suggestions and discussions. I wish to express my appreciation to Prof. Hiroshi Watanabe and Prof. Shigeru Yamago for their helpful advices on this thesis. I wish to acknowledge Prof. Ryuta Kasada at Institute for Materials Research, Tohoku University, Assoc. Prof. Yumi Matsumiya at ICR, Kyoto University, Assoc. Prof. Tomomi Honda and Mr. Masahiro Tsubota at Department of Mechanical Engineering, Graduate School of Engineering, University of Fukui, and Dr. Norio Ishizuka at Emaus Kyoto Inc. for their remarkable suggestions and support in part of the thesis.

I am also thankful to all the members of Prof. Tsujii's Laboratory for their kind helps, particularly, to Dr. Horoshi Eguchi, Mr. Shuhei Akimoto, Mr. Shuma Yasuda, Ms. Kimiyo Nakamichi, and Mr. Yoshihito Moriki for their support in experiments.

Furthermore, I would like to express my special thanks to Matsumoto Yushi-Seiyaku Co., LTD., especially President Naoki Kimura, Senior Managing Director Singo Yano, Auditor Sei-ichi Nishimoto, Auditor Shin-ichiro Yamane, Director Michihiro Shibano, Department Manager Yoshihiro Kando, and all the members of R&D department for their supports during this work.

Finally, I wish to express my heartfelt thanks to my wife Hiromi Shimizu, my elder daughter Hatsune Shimizu, and my second daughter Kotone Shimizu for their continuous support, encouragement, and smiles.

February, 2019

Yoshihiko Shimizu